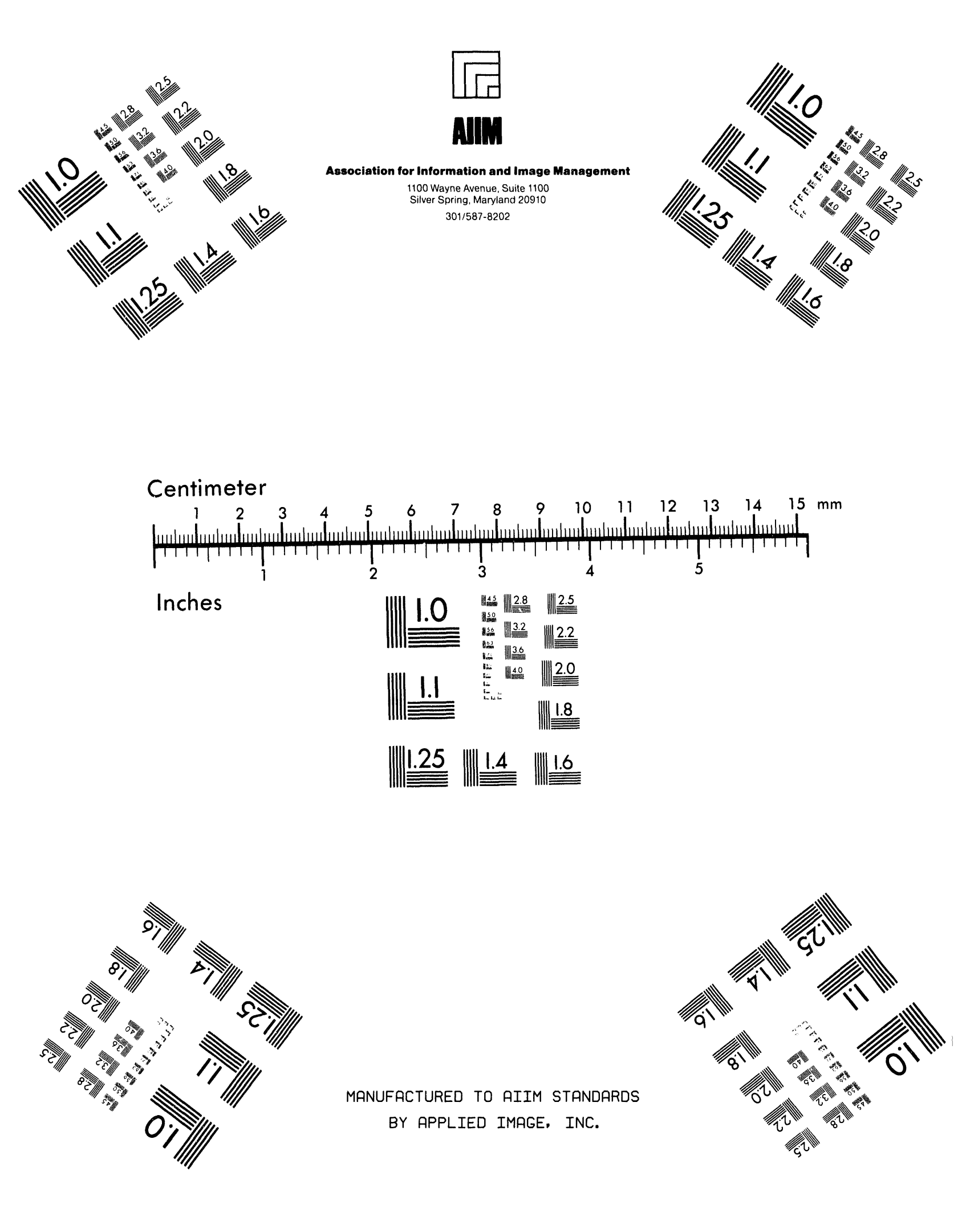
AIIM
Association for Information and Image Management
1100 Wayne Avenue, Suite 1100
Silver Spring, Maryland 20910
301/587-8202
Centimeter
Inches
MANUFACTURED TO AIIM STANDARDS
BY APPLIED IMAGE, INC.

1 of 2

DOE/BC/14852--4

RECEIVED
USDOE/PETC
93 APR 26 AM 10:38

SCALE-UP OF MISCIBLE FLOOD PROCESSES

QUARTERLY REPORT

Franklin M. Orr, Jr.
Principal Investigator

Department of Petroleum Engineering
Stanford University
Stanford, California 94305-2220

July 1, 1993- September 30, 1993

"US/DOE Patent Clearance is not required prior to the publication of this document."

DISCLAIMER

This report was prepared as an account of work sponsored by an agency of the United States Government. Neither the United States Government nor any agency thereof, nor any of their employees, makes any warranty, express or implied, or assumes any legal liability or responsibility for the accuracy, completeness, or usefulness of any information, apparatus, product, or process disclosed, or represents that its use would not infringe privately owned rights. Reference herein to any specific commercial product, process, or service by trade name, trademark, manufacturer, or otherwise does not necessarily constitute or imply its endorsement, recommendation, or favoring by the United States Government or any agency thereof. The views and opinions of authors expressed herein do not necessarily state or reflect those of the United States Government or any agency thereof.

MASTER

DISTRIBUTION OF THIS DOCUMENT IS UNLIMITED

Abstract

Progress is reported for a comprehensive investigation of the scaling behavior of gas injection processes in heterogeneous reservoirs. The interplay of phase behavior, viscous fingering, gravity segregation, capillary imbibition and drainage, and reservoir heterogeneity is examined in a series of simulations and experiments.

Compositional and first-contact miscible simulations of viscous fingering and gravity segregation are compared to show that the two techniques can give very different results. Also, analyzed are two-dimensional and three-dimensional flows in which gravity segregation and viscous fingering interact. The simulations show that 2D and 3D flows can differ significantly.

A comparison of analytical solutions for three-component two-phase flow with experimental results for oil/water/alcohol systems is reported. While the experiments and theory show reasonable agreement, some differences remain to be explained.

The scaling behavior of the interaction of gravity segregation and capillary forces is investigated through simulations and through scaling arguments based on analysis of the differential equations. The simulations show that standard approaches do not agree well with results of low IFT displacements. The scaling analyses, however, reveal flow regimes where capillary, gravity, or viscous forces dominate the flow.

Acknowledgements

This report summarizes work by an extended group of Stanford students, faculty, and research staff. The range of physical mechanisms considered testifies to their versatility: experiments, simulations, and analytical theory for flow of complex mixtures and phases, instabilities, heterogeneities, gravity and capillary forces. The richness of the physical interactions we study is an indication of the range of intellectual interaction we are fortunate to share.

Special credit for this report goes to Dengen Zhou, who took responsibility for assembling the completed package from a large set of computer files, cryptic editorial remarks, and annotated text fragments. He also contributed substantially to much of the work reported, especially the analysis of scaling in Chapter 5. MS student Rod Batycky contributed a significant section on his experimental work to verify the mathematical theory of multicomponent, multiphase flow developed previously in our group. Ph.D. student Marco Thiele and Prof. Martin Blunt report on their new and very efficient technique for simulations for heterogeneous reservoirs. Prof. John Fayers and visiting scholars Bruno Aleonard and Francois Jouaux describe their work to evaluate numerical approximations of compositional displacement process in heterogeneous reservoirs. MS student Darryl Fenwick reports on simulations that illuminate our capillary and gravity crossflow experiments. Ph.D. student Hamdi Tchelepi describes results of a large simulation study of two- and three-dimensional viscous fingering. That talented group is responsible for the work reported here.

All of us also thank Yolanda Williams, Pat Ota, and Jeanne Mankinen for their significant support of our work. Their careful attention to the financial, purchasing, and communications aspects of our project gives the researchers the time needed for research.

The work reported here was much influenced by many conversations and much assistance from our colleagues in Petroleum Engineering at Stanford. In particular, we are indebted to Khalid Aziz, Bill Brigham, Tom Hewett, Roland Horne, André Journel, and, of course, their students, for creating an unsurpassed environment for research.

The research described here was supported by the U.S. Department of Energy under Grant No. DE-FC22-92BC14852. We thank Tom Wesson, Jerry Casteel and their colleagues at the Bartlesville Project Office for their continued interest and support. In addition, thirteen companies provided support through the Stanford Gas Injection Affiliates Program: AGIP/RIGR, Arco Oil and Gas Co., BP Exploration Co. Ltd., Chevron Oil Field Research Co., Conoco Inc., Exxon Production Research Co., Japan National Oil Corporation, Marathon Oil Co., Mobil Oil Corporation, Norsk Hydro, Petronas, Texaco Inc., and UNOCAL. They have our heartfelt thanks, as well.

Lynn Orr
Stanford
October 1993

Contents

List of Tables

List of Figures

1. Introduction

When gas injected into an oil reservoir at high pressure, a richly complex set of physical mechanisms comes into play. Components transfer between oil and gas phases, viscous fingers form, geological heterogeneities move fluids in wonderfully complicated ways, and capillary and gravity forces drive flows. In this report, we examine the scaling of the interactions of those mechanisms. The goal of the work is to provide a base of physical understanding upon which can be built the design of gas injection processes for heterogeneous reservoirs.

In Chapter 2 we consider several aspects of the hydrodynamic instability that arises when low viscosity gas displaces more viscous oil. Interactions of phase behavior, heterogeneity, gravity segregation and viscous fingering are considered in Section 2.1, where simulations that include a representation of phase behavior are compared to others that treat the fluids as miscible. The simulations show that first-contact miscible calculations give quite different results from those in which effects of phase equilibrium are included. Section 2.2 offers a comparison of unstable single-phase flows in two- and three-dimensional (2D and 3D) porous media. Those computational results from the Stanford particle-tracking model show that effects of viscous fingering in 2D and 3D flow are similar only if gravity segregation is not important. When gravity segregation and viscous instability are both important, 2D flow can differ substantially from 3D flow. The calculations reported are the first detailed investigation of the transition from gravity-dominated to fingering-dominated flow for 3D porous media.

Chapter 3 describes a new technique for simulation of flow in heterogeneous reservoirs. The new method is a combination of streamtube calculations, which have long been used for single-phase flow, with one-dimensional analytical solutions for multiphase flow. The new approximation is much more efficient than standard reservoir simulation.

Chapter 4 describes an experimental test of the analytical theory, developed at Stanford, for one-dimensional multicomponent, two-phase flow. The experimental results are in reasonable, though not perfect agreement with the theory for three-component displacements.

Chapter 5 examines the interactions of capillary, gravity and viscous forces. Section 5.1 reports results of simulations of imbibition experiments performed with fluid phases that exhibit low interfacial tensions. The simulations demonstrate that much remains to be learned about how to model low IFT displacement processes. Section 5.2 reports an analysis of scaling behavior for gravity, capillary and viscous forces. Also reported is an attempt to delineate flow regimes for flow processes that include gravity, viscous and capillary forces.

The combination of experimental and theoretical results presented here is part of a comprehensive investigation of scaling of gas injection processes for heterogeneous reservoirs. This report covers work that is thoroughly "in progress." Thus, the results reported represent a step toward the goal of improved design capability based on clear understanding of the scaling underlying physical mechanisms of flow.

2. Modeling of Viscous Fingering in Heterogeneous Media

In most gas displacement processes, the mobility of gas is much larger than that of oil. This unfavorable mobility contrast induces viscous fingering, which results in low breakthrough recovery. Understanding the factors influencing the development of viscous fingering is of great importance in optimizing a gas injection process. Recent studies have indicated that multicontact processes do not generally reach miscibility, due to dispersion [68, 36] and due to crossflow between zones with different permeability [49, 50, 51, 52]. Therefore, phase behavior could have a significant impact on the development of viscous fingering. For example, because the displacement is not quite miscible, the presence of some liquid oil phase reduces gas relative permeability which also reduces the gas mobility. As a result, the mobility contrast is less unfavorable than that of completely miscible displacements. Consequently, viscous fingering would develop differently. Gravity segregation tends to push gas into the top part of the reservoir and reduces the vertically sweep efficiency. The impact of reservoir heterogeneity on viscous fingering and gravity segregation is another important aspect in description of gas displacement performance. In this chapter we examine the interplay of those mechanisms.

In Section 2.1, the effects of phase behavior on gas displacement are examined based on compositional simulations for a stochastically generated 2D heterogeneous media. We also compare the results of fully compositional simulations and simpler first contact miscible simulations, which are often used in study of two-component high resolution viscous fingering. We find that we can reproduce a compositional solution by miscible simulations at a reduced mobility ratio. In Section 2.2, simulations of viscous fingering performed with a particle-tracking simulator have been extended to 3D porous media. Comparison of simulations of viscous fingering in 2D and 3D models were conducted for cases with and without gravity effects, and for homogeneous and heterogeneous media. We find that 2D simulations represent flow features as well as 3D simulations do only where gravity effects are not included. However, for cases with consideration of gravity effects, 3D simulations give very different flow pictures from 2D simulations.

2.1 Progress With Compositional Studies in Heterogeneous Systems

F. J. Fayers, B. Aleonard, F. Jouaux

2.1.1 Introduction

The intention of this work is to obtain a better understanding of how phase behavior, adverse viscosity ratio, viscous fingering, heterogeneity and gravity interact in compositional modeling of gas displacement processes. One of the difficulties in understanding such problems arises from the fact that in a multicontact process leading to miscibility, the two phases move quickly towards equality in composition, so that density and viscosity contrasts are substantially reduced. However, at positions away from the mixing zone, the injected and *in situ* phases retain their original contrasts in properties. This led to the Todd and Longstaff method [67] for modeling viscous fingering in such systems, where the problem is represented in terms of a mixing rule with effective properties for the phases. This formulation neglects phase behavior and is based on the hypothesis that the system behaves very similarly to a first-contact miscible process. More recent studies have

indicated that multicontact processes do not generally attain miscibility (see for example [36]), and that dispersion effects can lead to submiscible behavior with some detrimental effects on oil displacement. Another factor relates to heterogeneity, where it is becoming increasingly evident [2] that reservoir heterogeneity has a strong effect on fingering patterns, although the magnitude of the adverse viscosity ratio also strongly influences the behavior. The correct way to adjust the Todd and Longstaff mixing parameter for heterogeneity is poorly understood. Because heterogeneity forces the displacing fluid to take preferred paths, the sweep characteristics are very different from the homogeneous case, and the assumptions of uniform mixing within large grid blocks are highly erroneous. For these reasons, the alpha-correction procedures were introduced by Barker and Fayers [5] into compositional modeling to compensate for the nonuniformities in phase behavior and component transport associated with the use of large grid blocks.

In the present studies, we will set up a "mildly" heterogeneous problem and study the attributes of various ways of representing its behavior under nearly miscible displacement. Understanding how to use compositional models to predict gas displacement more reliably in heterogeneous applications has become an important question. We will assume that the scale size involved is sufficiently large that capillary forces and diffusion processes are negligible. At the laboratory and somewhat larger scales, these effects cannot be neglected in nearly miscible processes [23] but their omission may be appropriate at the reservoir scale.

Two major simulators have been used in this work. The first code, MISTRESS, is a fast high resolution simulator developed by Christie *et al.* [14] at BP Research, which models a two-component first-contact miscible process. Its high resolution is achieved through fine gridding and use of an FCT-algorithm [13] for controlling numerical dispersion. It has been used to understand the physics of viscous fingering in homogeneous systems [24], and also some work has been done in heterogeneous systems [26]. The second code MORE, is a commercial compositional simulator developed by Young [73] at Reservoir Simulation Research Inc. It has high speed efficiency for finely gridded problems, and is very fast on the Cray YMP computer used in this work. It does not have special features for controlling numerical dispersion, and the unquantified influence of this in compositional problems will be partially examined in these studies. We will also be looking at some special features associated with variable interfacial tensions, which have been programmed into MORE through the Elf Geosciences Center.

2.1.2 The Permeability Field

Permeability distributions have been generated using the moving average technique in 2D, based on averages within an ellipse (major and minor axes give the anisotropic correlation lengths α_l and α_t). Random permeabilities are first normally generated using a random number generator on a fine (128 $\times$ 64) grid, with further points generated for averaging outside the rectangle of interest. The moving averages are taken on the fine grid, and thence a log transformation is used to give a log normal distribution. The distribution shown in Fig. 2.1 was the principal realization studied, which was generated using the parameters: L/W = 3.0, α_l/L = 0.2, α_t/W = 0.06 and σ_{lnk} = 0.69. The distribution was intentionally chosen to give rather long and thin permeability zones, thought to be more appropriate to real geology. We also wished to create a distribution which was reasonably statistically homogeneous as a function of x (clearly not so) and to be not too heterogeneous (the Dykstra-Parsons index for this problem is V_{DP} = 0.50). A reduced grid of permeability values (64 $\times$ 32) was also formed by performing a simple renormalization based on a 2 $\times$ 2 column and row averaging procedure (see Fig. 2.1b).

2.1.3 Phase Behavior

Three types of phase behavior have been studied as follows :

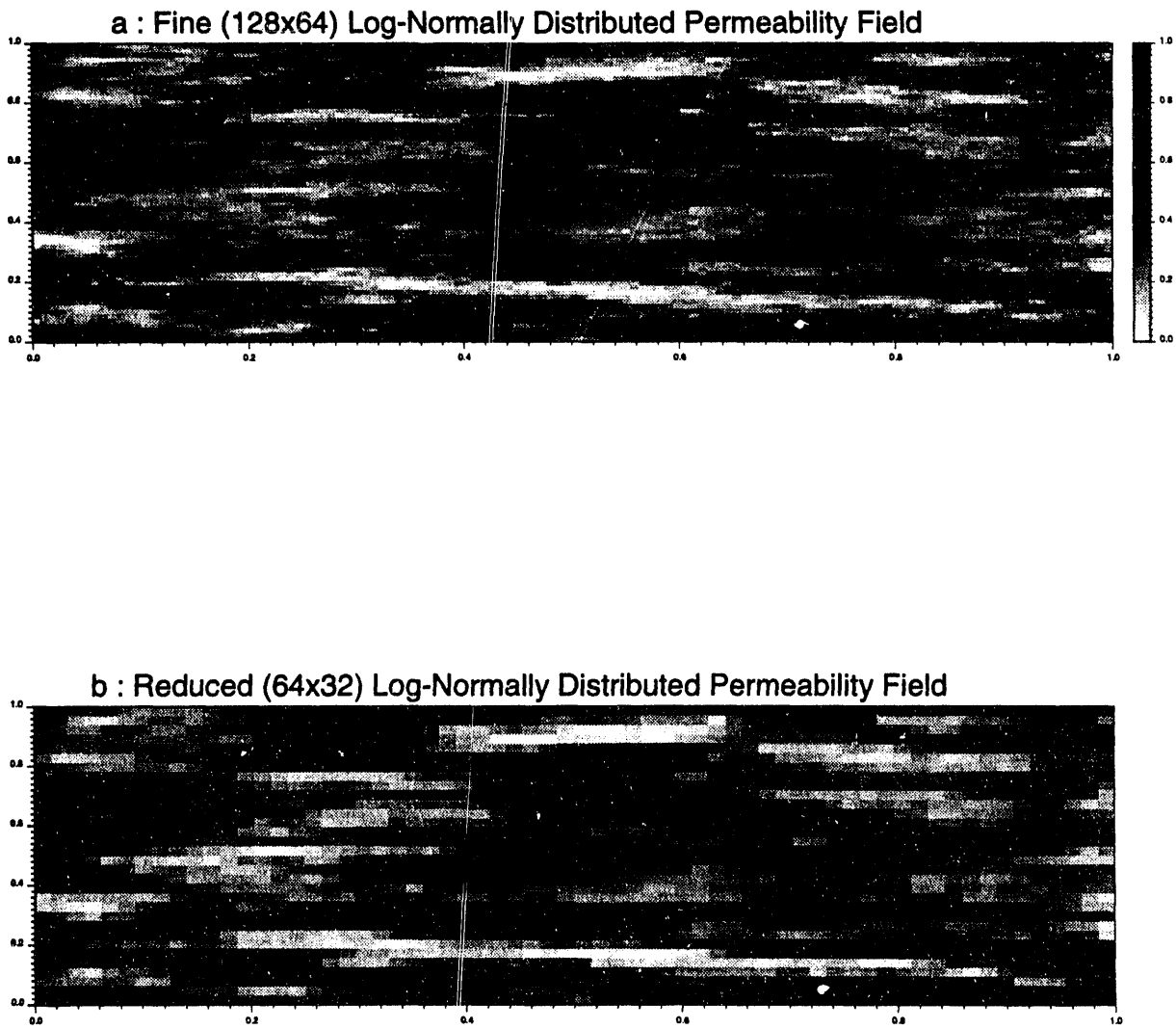

Figure 2.1: The permeability distribution used in this work.

Table 2.1: The parameters for the PR equation

Component	M_w (g/mol)	P_c (Psi)	T_c (F)	Ω —	Parachors —	%Mole Oil/Mis. Gas
C_1	16	671.17	117.07	0.1592	77.1	36.92/32.77
C_2+	41	769.81	142.79	0.013	141	11.55/67.23
C_5+	189	322.89	775	0.6736	588	42.81/0
$C_{30}+$	451	171.07	1136.59	1.0259	1453	8.71/0

Table 2.2: The PR-parameters used in this work

Component	M_w (g/mol)	P_c (Psi)	T_c (F)	Ω —	% Mole Oil /Mis. Gas
CO_2	44	1071.34	87.56	0.225	4.48/20.81
CH_4N_2	16	671.17	117.07	0.013	36.92/32.77
C_2	30	708.35	89.72	0.0986	3.21/20.08
C_3	44	617.38	205.82	0.1524	2.33/22.23
C_4	58	543.31	294.58	0.187	1.53/ 4.11
C_5	72	475.28	366.46	0.2523	0.88/0
C_6	86	419.54	439.41	0.3138	1.27/0
C_7+	108	417.69	584.35	0.3739	9.17/0
$C_{10}+$	152	407.14	670.78	0.5489	11.19/0
$C_{14}+$	213	314.34	808.24	0.755	11.22/0
$C_{20}+$	312	205.28	954.6	0.875	9.09/0
$C_{30}+$	451	171.07	1136.59	1.0259	8.72/0

1. First contact miscible displacements with $\mu_o/\mu_g = 20$ and $\rho_o = 49.2$ lb/ft^3, $\rho_g = 24.5$ lb/ft^3.

2. A four-component model of slightly submiscible displacement, using the data of [36] with a C_2+ enrichment of 67.23 mol% for the injected gas. The parameters for the Peng Robinson equation are listed in Table 2.1. These properties give viscosities and densities close to those in (1) for the initial fluids.

3. A twelve-component model from which the values in the four-component model were consistently derived [36]. The PR-parameters are given in Table 2.2 in this paper.

The parameters in (2) and (3) are associated with slightly submiscible displacement [36] but nevertheless the phase behavior ensures a reasonably efficient oil displacement, of the type which probably occurs in many "miscible" condensing/vaporizing displacements.

2.1.4 Results Without Gravity

Base Case MORE Calculations

A base case was run with the MORE four-component model on the fine grid. The gas saturation distribution is shown in Fig. 2.2, there is no evidence of injected gas components moving ahead of the S_g-values, since C_1 remains fixed at the *in-situ* value ahead of the gas front. The gas phase distribution is strongly controlled by the heterogeneities. Use of the reduced grid was expected

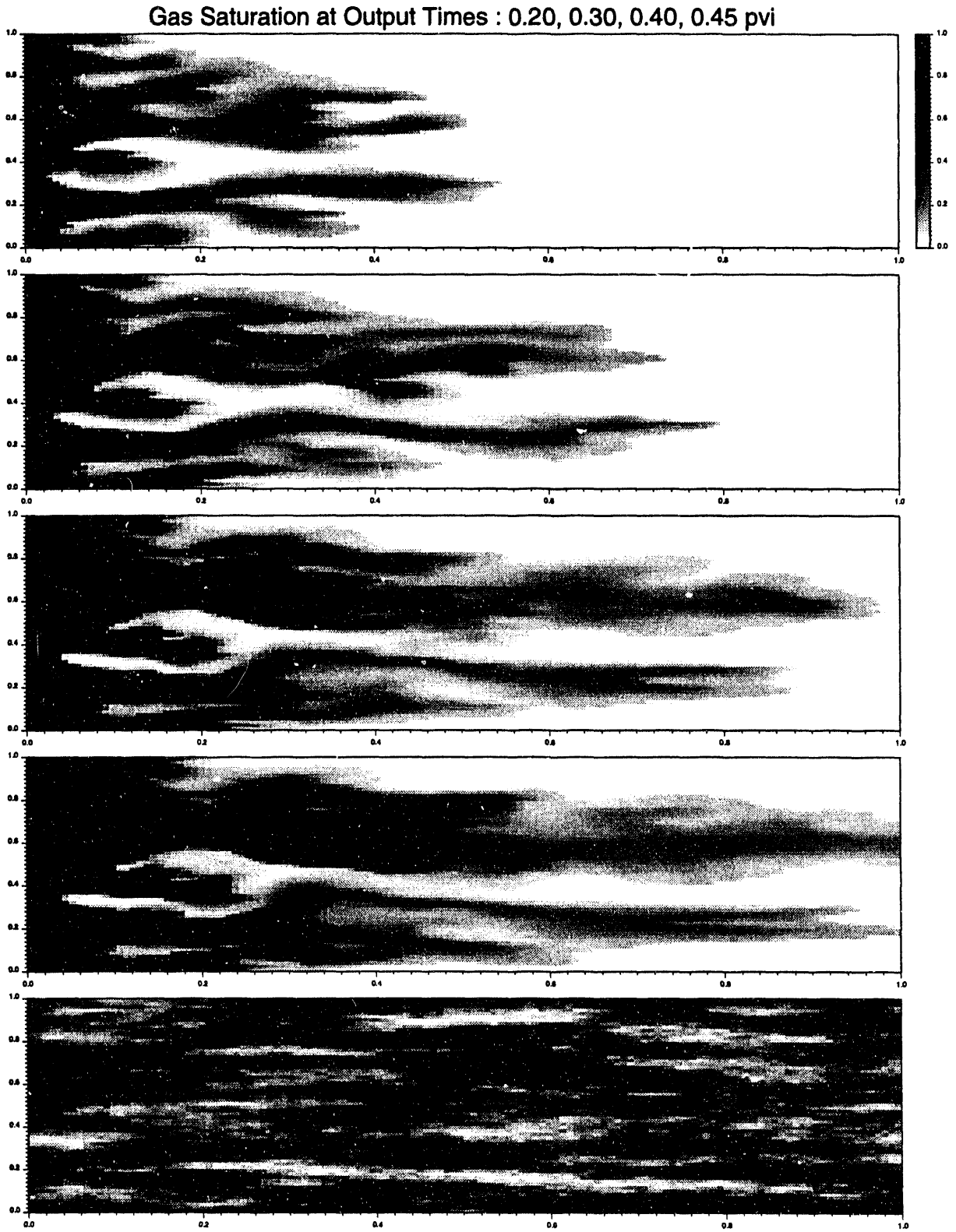

Figure 2.2: MORE four-component run on the fine grid (no gravity).

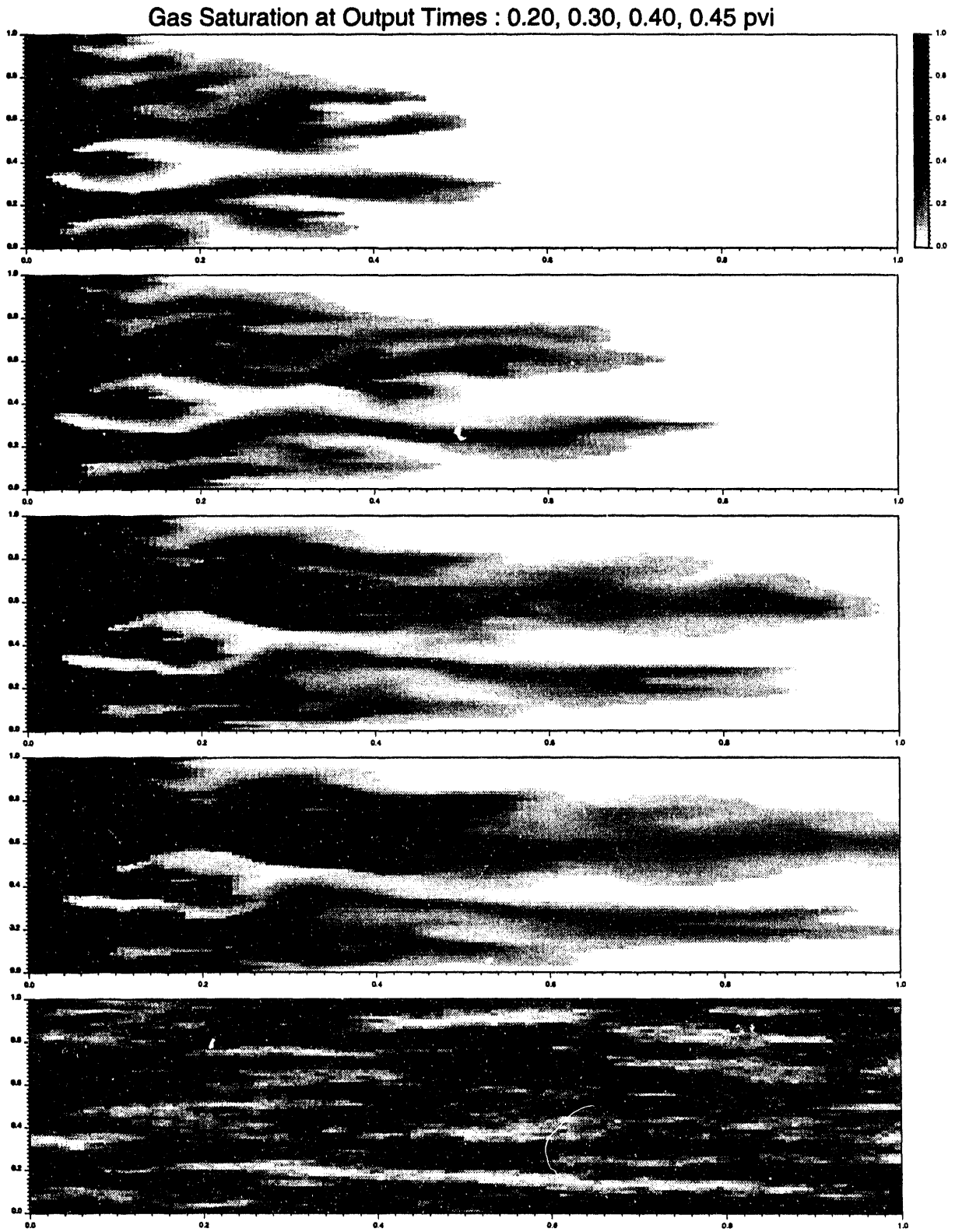

Figure 2.3: MORE four-component run on the reduced grid (no gravity).

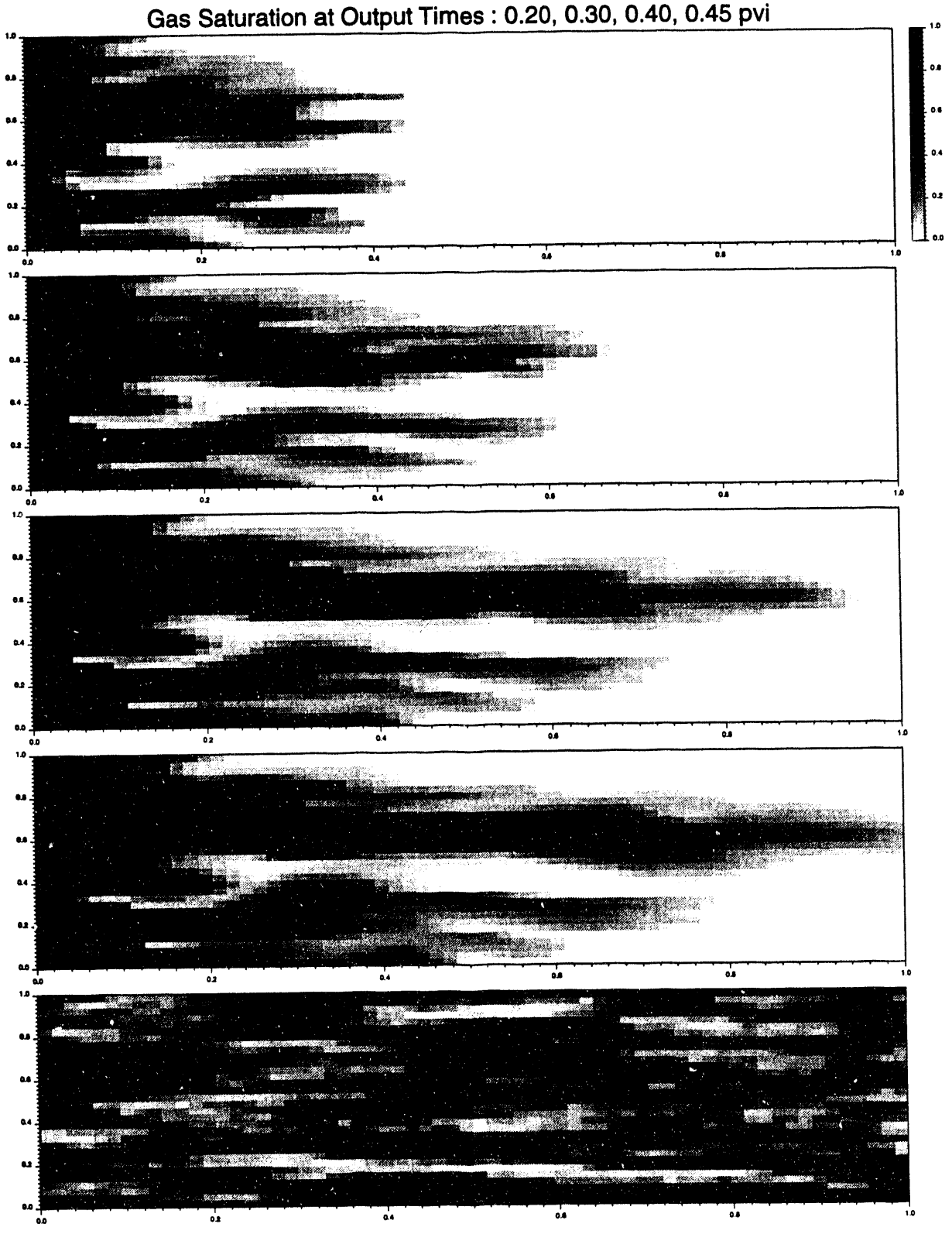

Figure 2.4: MORE twelve-component run on the reduced grid (no gravity).

to cause two sources of smoothing error, namely reduced permeability spread due to averaging and increased truncation errors in the finite difference method. Fig. 2.3 indicates that the consequent errors are tolerable, with the reduced grid still giving a fair reproduction of the main characteristics from the fine grid, including only a small error in breakthrough time. The effects of a more accurate representation of phase behavior were tested using the twelve-component model where comparison of Figs. 2.3 and 2.4 indicates almost no changes, i.e. the four-component approximation is more than adequate. In view of this, no further cases were run with twelve components. These results confirm the view that satisfactory compositional simulation in reservoir applications can often be performed with relatively few components (e.g. four to six). The relative permeabilities used in MORE have been based on $k_{ro} = S_o^{*2}$, $k_{rg} = S_g^{*2}$ with $S_{org} = 0.15$ and $S_{gc} = 0.05$. Thus high oil recovery is primarily driven by phase behavior. We also examined $k_{ro} = S_o^*$, $k_{rg} = S_g^*$ with $S_{org} = 0$ and $S_{gc} = 0$, i.e. straight lines assuming almost miscible behavior. The results shown in Fig. 2.5 indicate a very high degree of dispersion at low gas saturations. This must be partly physically driven by the much larger gas mobility at low saturation, but there may be exaggerated numerical dispersion errors due to the absence of any self-sharpening character in the fractional flow. It is interesting that the method of characteristics solutions for 1D flows suggest that there is only a weak dependency on fractional flow when the system is close to miscibility. Instead of solving by the method of characteristics, accurate 1D MORE solutions for gas saturations were obtained using 500 gridblocks for the two forms of relative permeabilities. These are compared in Fig. 2.6, which demonstrates that the straight line form will be more dispersed, although the numerical dispersion errors are now much reduced. There is also a light component front now moving ahead of the gas front. Recently completed Elf modifications to MORE which allow relative permeability adjustment with interfacial tension have also been examined. The interfacial tension is calculated by the Mcleod-Sugden correlation

$$\sigma^{1/4} = \sum_i^{N_c} P_{ic} \left(\frac{\rho_o x_i}{M_o} - \frac{\rho_g y_i}{M_g} \right) \tag{2.1}$$

where ρ_o and ρ_g are oil and gas phase densities and M_o, M_g the corresponding molecular weights. P_{ic} is the Parachor for component i. The parachor values used in this study are listed in Table 2.1. The default option in the Elf extension to MORE satisfies the following rules: For phase j

$$k_{rj} = [1 - f(r)]\, k_{rj}^{im} + f(r) k_{rj}^{m} \tag{2.2}$$

where im and m imply the limiting immiscible and miscible relative permeabilities, and the weighting function $f(r)$ is defined by

$$f(r) = (1 - r) exp(-r) \tag{2.3}$$

where $r = min\left(\frac{\sigma}{\sigma_o}\right)$. The magnitude of the switching parameter σ_o, determines the interfacial tension at which the weighting towards straight-line relative permeabilities will commence. With σ_o set to a threshold of 0.01 dyne/cm, and then to 0.1 dyne/cm, the results were almost identical to those from immiscible relative permeabilities in Fig. 2.3. The trend towards straight lines starts to occur using $\sigma_o = 1.0$ dyne/cm. The results shown in Fig. 2.7 are now somewhat closer to Fig. 2.5, but still similar to Fig. 2.3. This value for σ_o is probably too high in terms of expectation of a real change to immiscible relative permeabilities. Thus for nearly miscible processes in heterogeneous systems, the use of the unmodified immiscible relative permeabilities appears to be justified.

Equivalencing First-Contact Miscible Calculations to Compositional Results

It would be very convenient if compositional calculations could be replaced by appropriate first-contact miscible calculations in the consistent heterogeneous geometry. The MISTRESS code

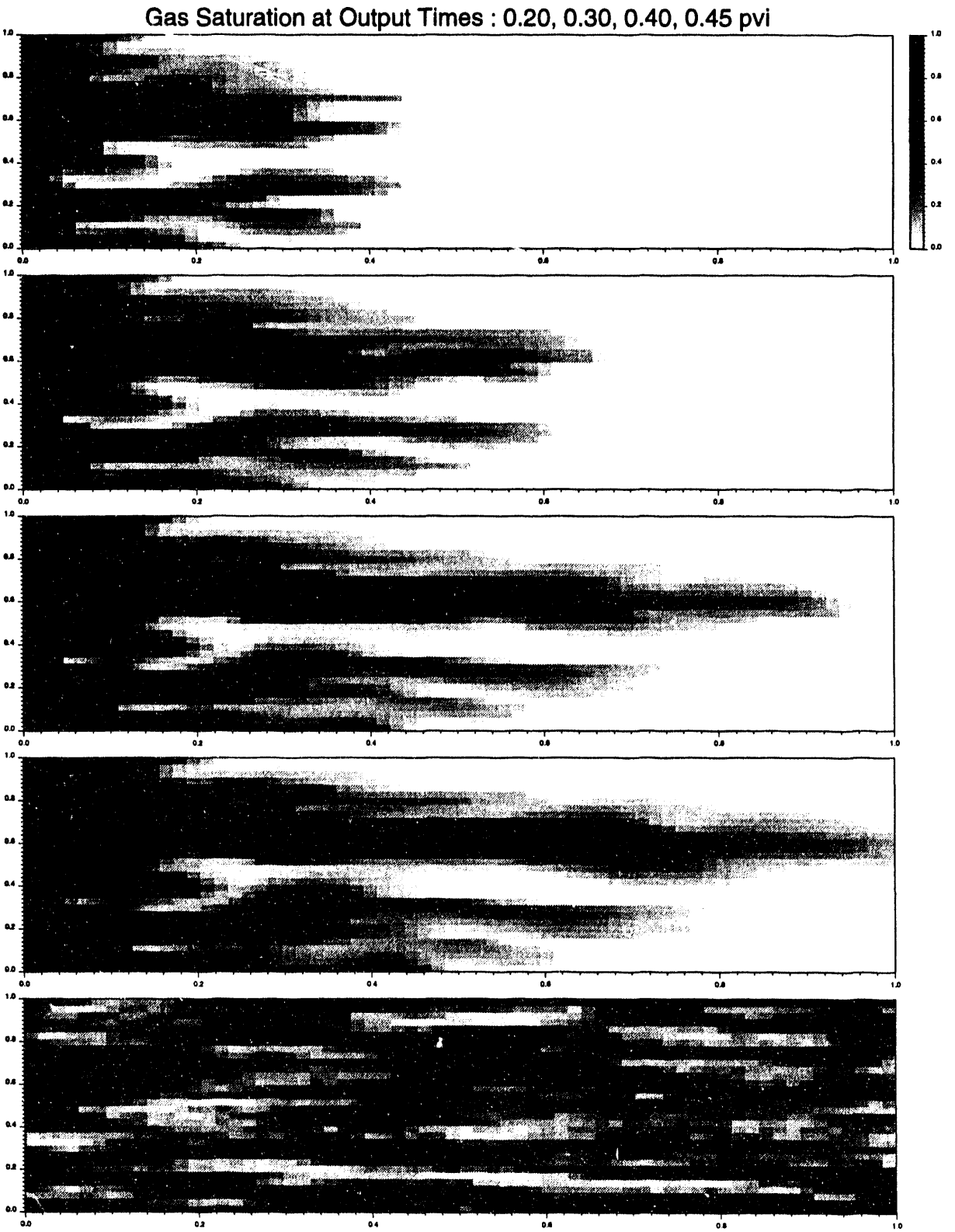

Figure 2.5: MORE four-component run on the reduced grid (no gravity) with straight line relative permeabilities.

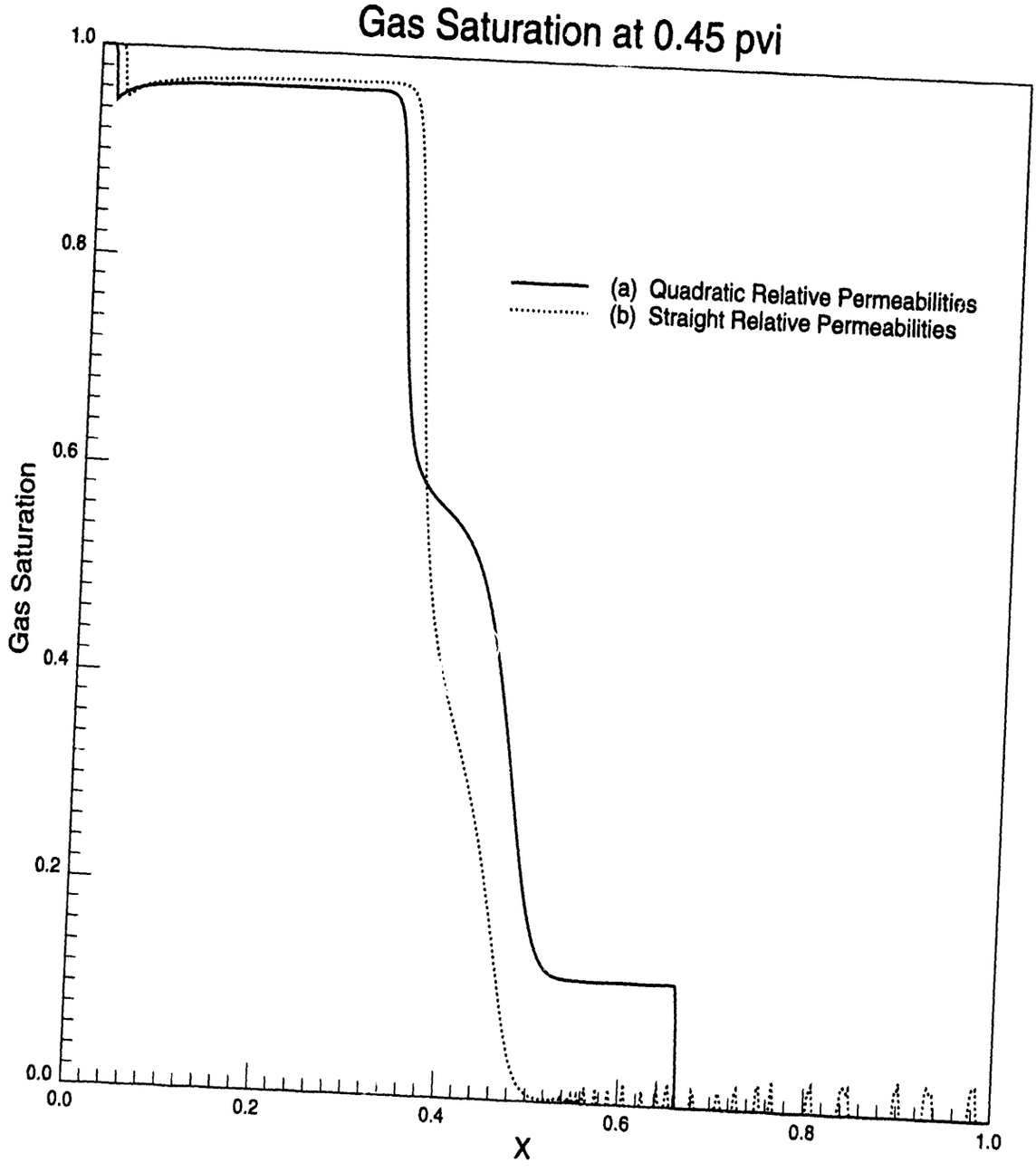

Figure 2.6: MORE four-component run on a homogeneous 1D grid (500 grid blocks).

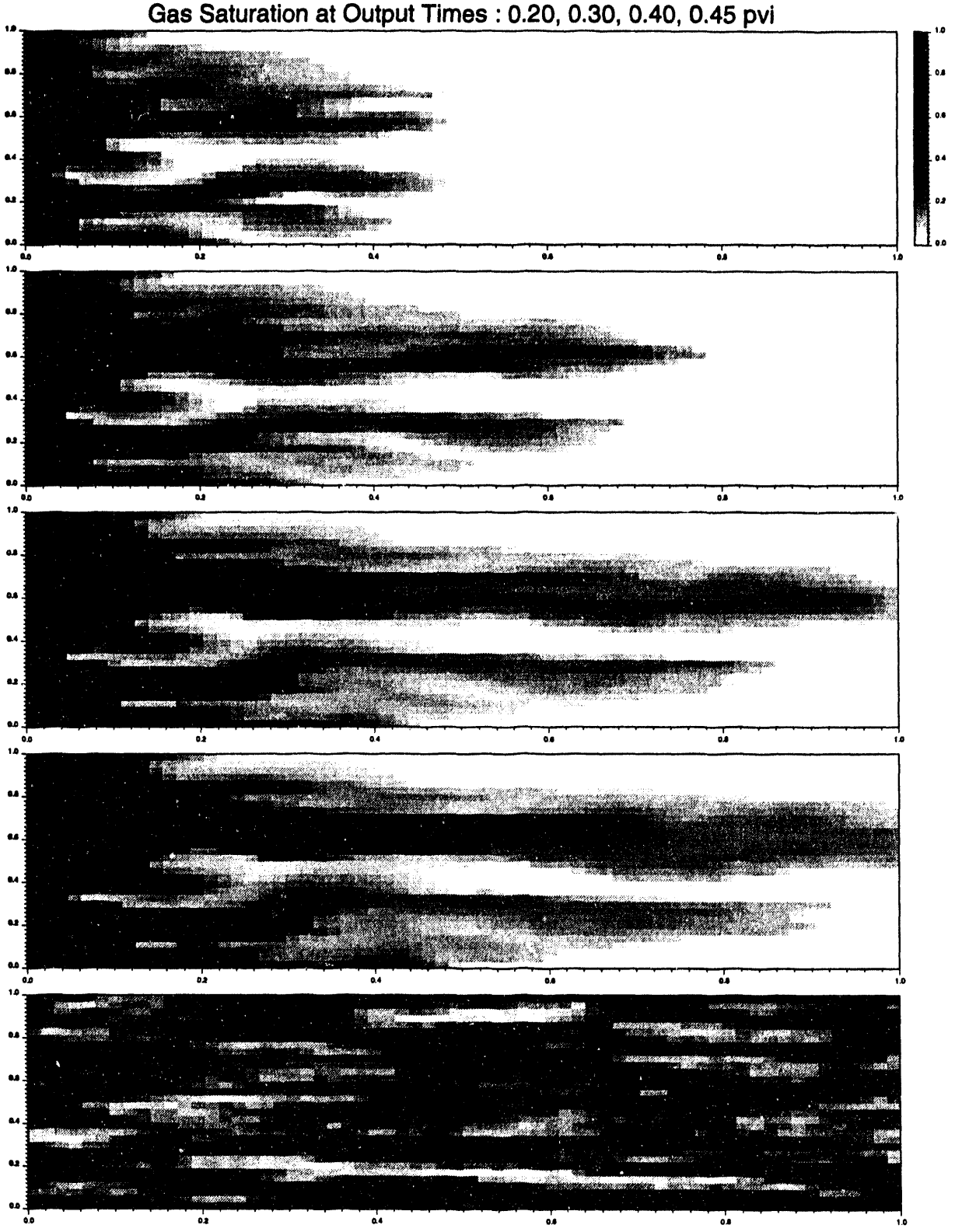

Figure 2.7: MORE four-component run on the reduced grid with IFT-adjusted relative permeabilities (S_o = 1.0 dyne/cm).

has been run for the fine and reduced permeability models to test this possibility. The fine grid results for $\mu_o/\mu_g = 20$ are shown in Fig. 2.8 which should be compared with Fig. 2.2 for the equivalent four-component MORE calculation. This shows finer fingers with MISTRESS and an earlier breakthrough. Thus the first-contact process in a heterogeneous system is more unstable than its submiscible compositional counterpart. The last calculation was replaced with the reduced grid, as shown in Fig. 2.9. This indicates a solution with a similar character, but now the breakthrough time is surprisingly, slightly more advanced. To test the effects of numerical dispersion in the MORE code, a method was found to allow this code to simulate a first-contact MISTRESS calculation. This entailed choosing the same properties for each component in a two-component model in the input data to MORE, and then adjusting the z_c-critical factors to cause the correct viscosity ratio in the Lohrenz-Bray-Clark correlation, i.e. 20:1. This gives a flatter mixing behavior than the 1/4-power mixing law. The MORE calculation is shown in Fig. 2.10 for the reduced grid, which shows some exaggerated numerical dispersion, but less dispersive than Fig. 2.5. However, the general character is similar to MISTRESS and the breakthrough time is only delayed slightly. Although the effects of numerical dispersion in two-component miscible models are different from multicomponent models with phase behavior, the above MORE results give encouragement about the nondominance of dispersion errors in MORE. It therefore seems unlikely that the numerical dispersion is a significant feature in reducing the instability of the compositional displacement. All of the first-contact miscible solutions are consistent with an effective mobility ratio which is too high. One method for fixing up the effective mobility ratio is to choose M_e consistent with the Koval value, arguing that viscosity mixing dominates in the channels of the heterogeneity. This approach is sometimes used in streamtube models. The Koval effective ratio is $M_e = 2.3$. The MISTRESS calculation run with this ratio is shown in Fig. 2.11. The delay in breakthrough is now too much and this result is not a satisfactory compromise. A second method for choosing the appropriate mobility ratio is based on the results of Rubin *et al.* [58] for viscous fingering in compositional problems in homogeneous media. They suggest that the fingering is primarily controlled by the mobility ratio across the principal shock of the analytic 1D solution. The saturations and compositions for curve (a) of Fig. 2.6 in the 500 point 1D calculation were used to estimate the variations in λ_t, the total mobility, as indicated in Fig. 2.12. It is seen that the primary variation occurs between $\lambda_t = 0.44$ and $\lambda_t = 2.20$ giving $M_e \sim 5.0$. A MISTRESS calculation run with this ratio, illustrated in Fig. refffig 13, now gives reasonably close agreement with the MORE four-component result in Fig. 2.2. Further examples are needed to test the generality of this equivalencing in heterogeneous problems.

2.1.5 Results with Gravity

Calculations with gravity are known to be sensitive to the effects of heterogeneity, because of the competition between mixing processes. Mixing governs $\Delta\rho$ and therefore controls gravity override, but mixing also controls the viscous drive through high permeability channels, which prevents large scale mixing and therefore modifies phase behavior. In general, we do not expect compositional and first-contact miscible models to be compatible when gravity is important. Cases for the same permeability models have been run for a vertical cross section, again with L/W = 3.0. We use the definition of gravity number given by:

$$N_g = \frac{q(M-1)W}{\Delta\rho g L\sqrt{k/\mu_g}} \tag{2.4}$$

where $\Delta\rho$ is the density difference between injected and *in-situ* phases, μ_g is the injected gas phase viscosity and q is the injection rate per unit area at the left boundary. We have used the arithmetic average permeability for our heterogeneous problem. The MORE calculation with $N_g = 2.0$ did not show much gravity effect (contrary to what would be expected for a homogeneous problem

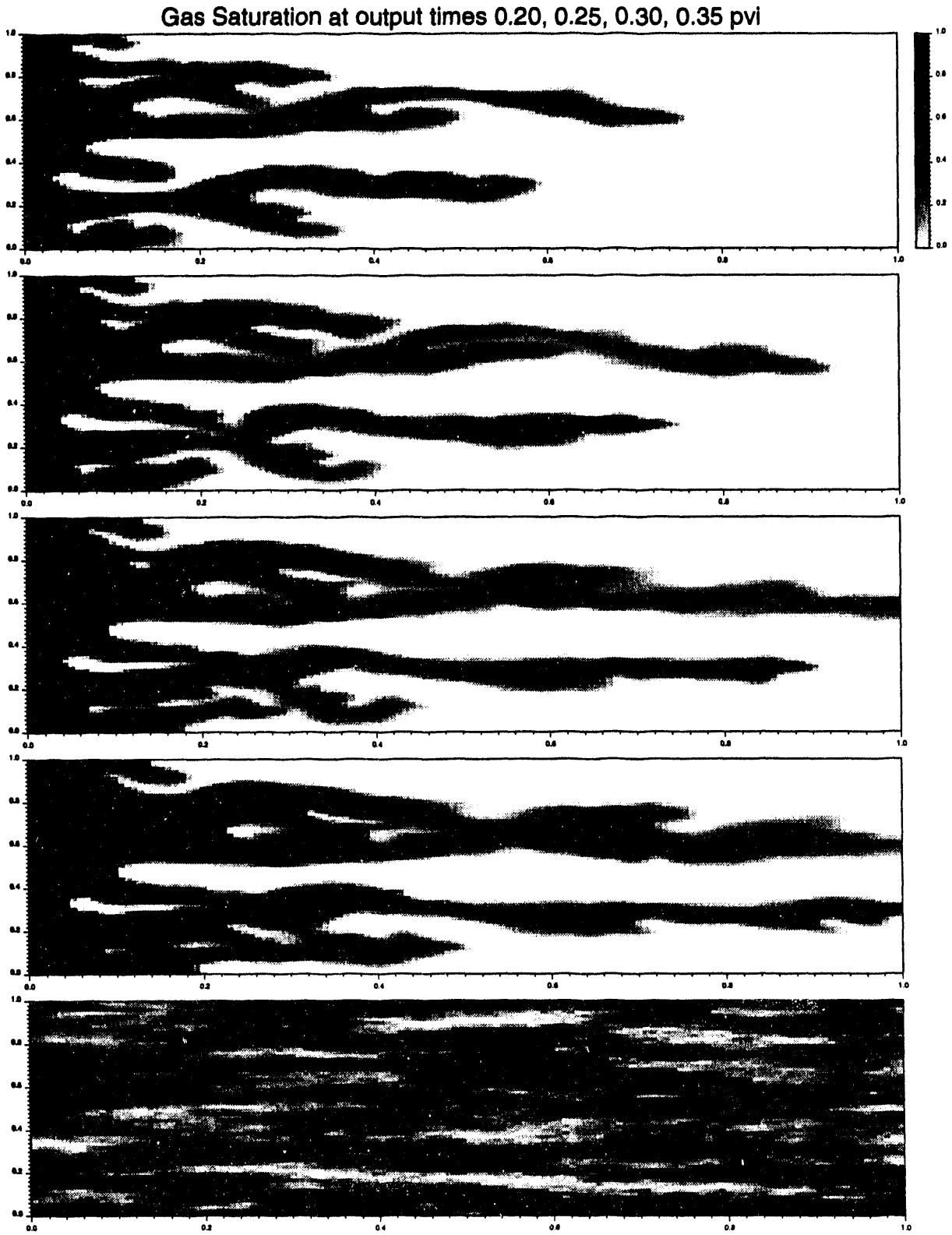

Figure 2.8: MISTRESS run with M = 20 on the fine grid (no gravity).

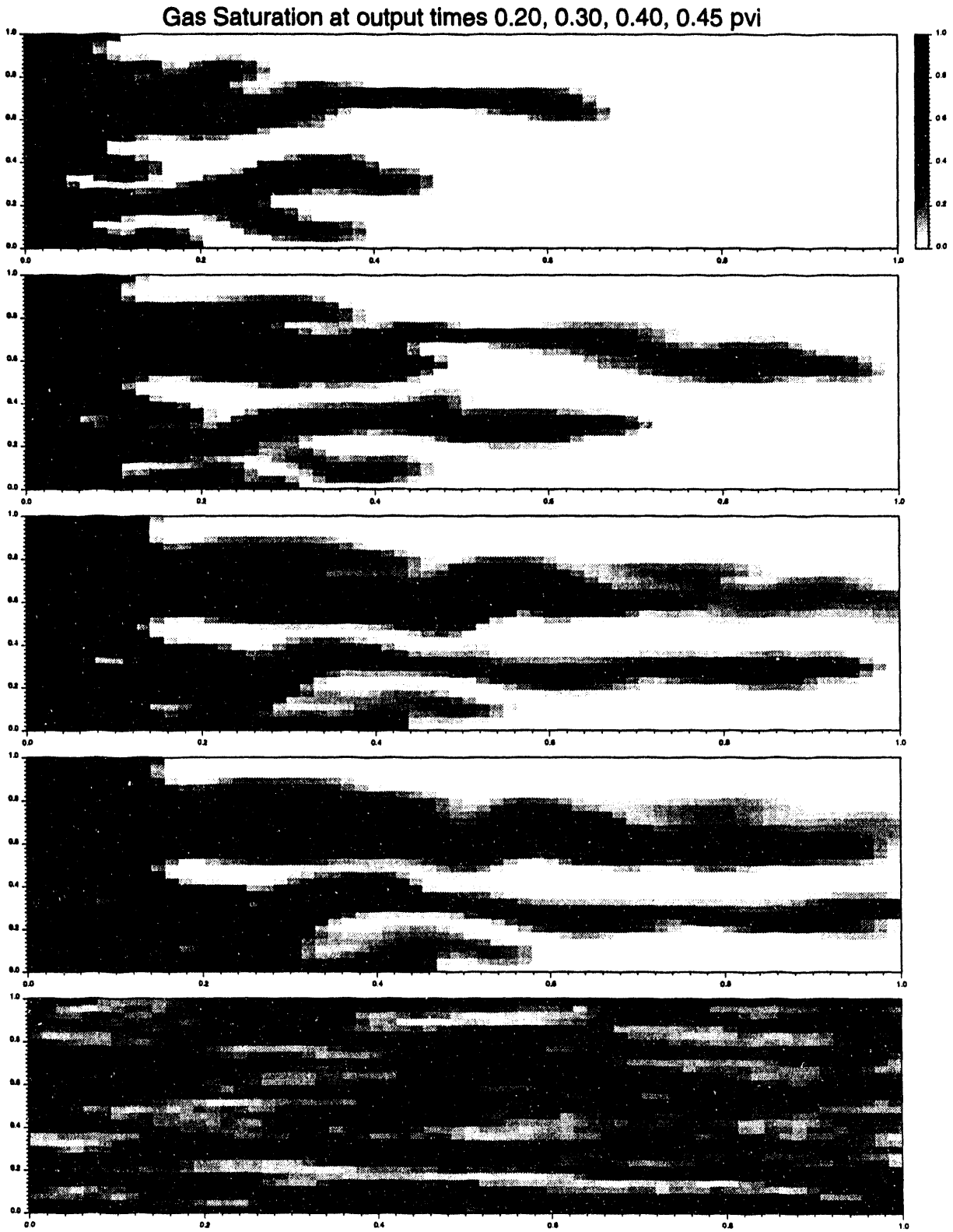

Figure 2.9: MISTRESS run with M = 20 on the coarse grid (no gravity).

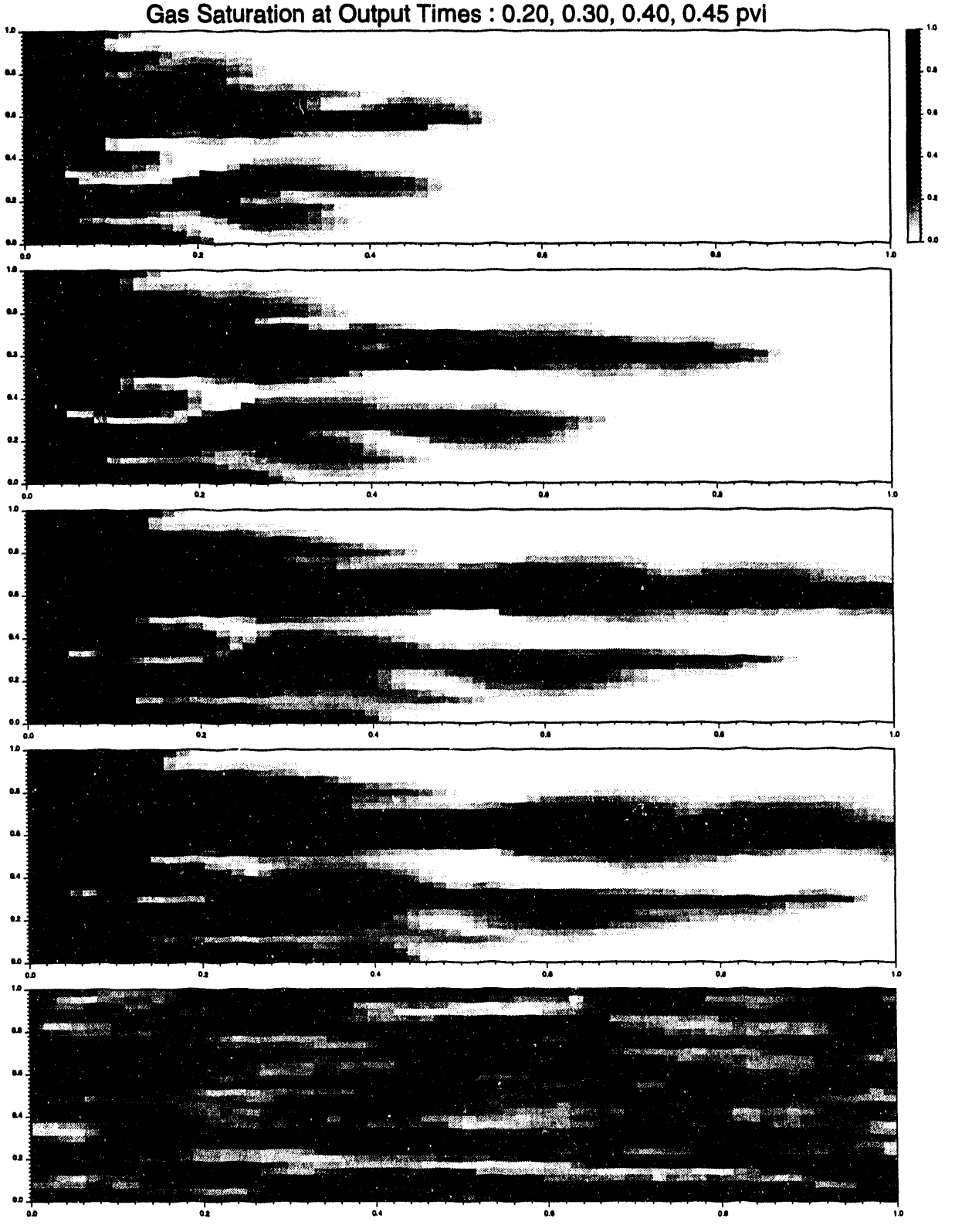

Figure 2.10: MORE "first-contact miscible" run on the reduced grid (M = 20 and no gravity).

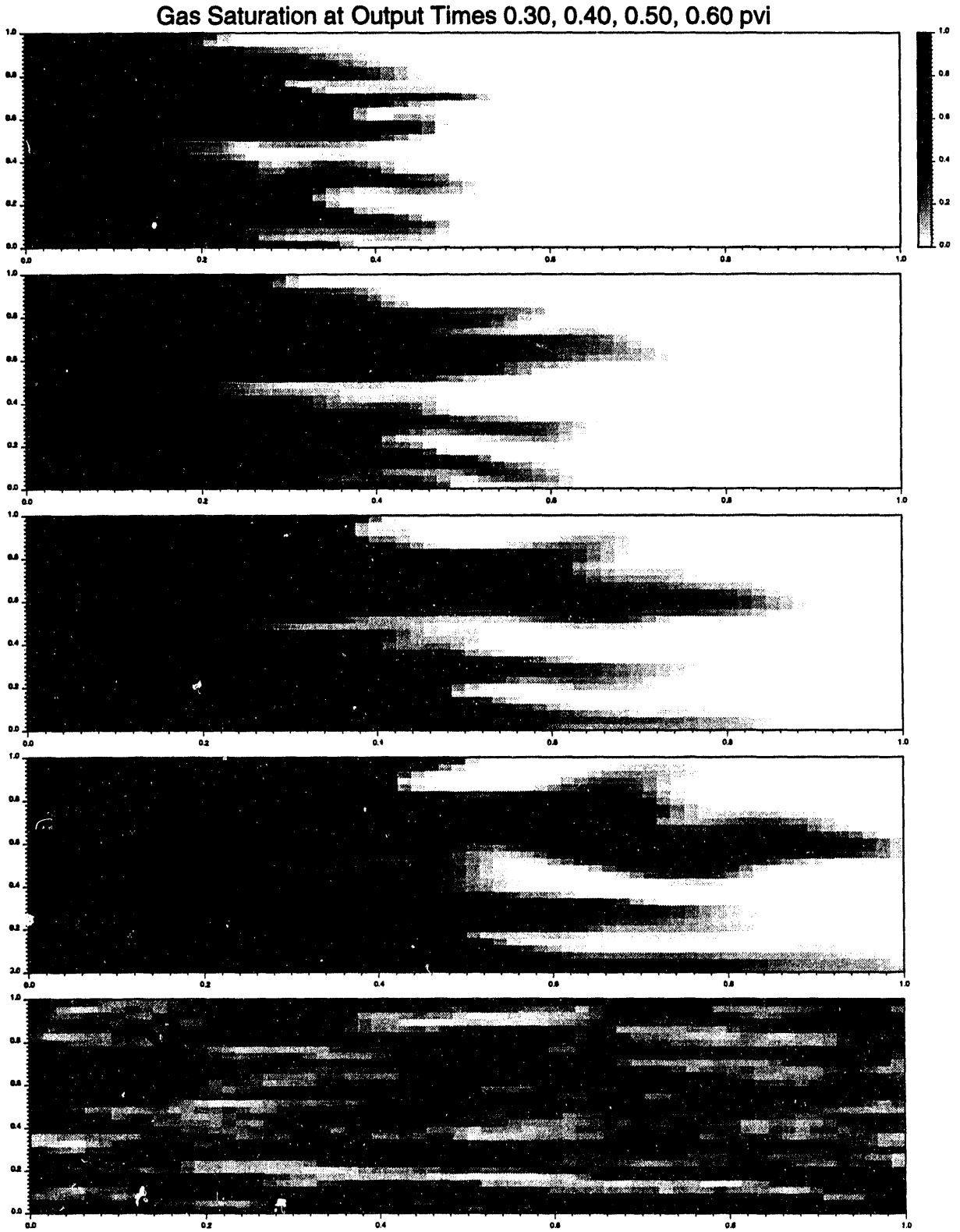

Figure 2.11: MISTRESS run with M = 2.3 on the coarse grid (no gravity).

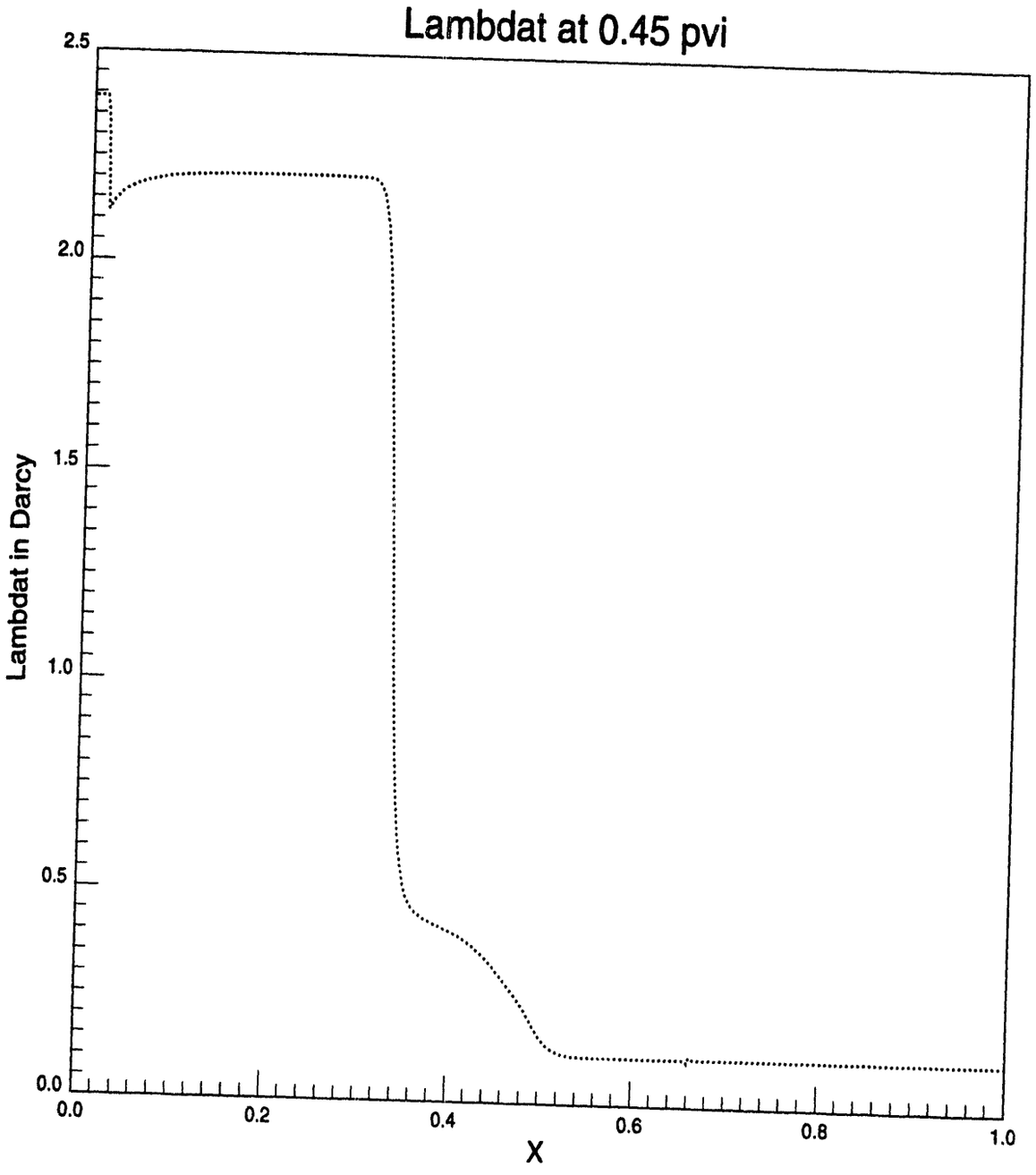

Figure 2.12: MORE four-component run on a homogeneous 1D grid (500 grid blocks).

[25]). However, results for $N_g = 1.0$ shown in Fig. 2.14 now show significant differences from Fig. 2.3. There is a very early breakthrough caused by the thin gravity tongue in the top layer. Using the fine grid gives much the same results, as seen in Fig. 2.15, but with an even finer tongue. It is necessary to decrease the flow rate by another factor of 5 to give $N_g = 0.2$, before gravity essentially overcomes heterogeneity (Fig. 2.16). The permeability distribution creates asymmetry in the effective horizontal and vertical permeabilities, so that $k_{evff}/k_{heff} < 1.0$. This implies N_g in Eq. 2.4 should be rescaled by, which would probably cause the rescaled N_g in the last case to move closer to 0.5, the value at which gravity override is expected to completely overcome viscous fingering in homogeneous cross sections [25]. A first-contact miscible (FCM) calculation for the case $N_g = 1.0$ run on MORE, illustrated in Fig. 2.17, shows considerably less gravity override than observed in the four-component result in Fig. 2.15. The more pronounced gravity effect arises in the immiscible case because the two phases have different densities which give a finite segregation term in the fractional flow equation. The density difference is largest at the small gas saturation values, which therefore gives a significant upward dispersion appearance to the results in Fig. 2.15. We believe this is a real physical effect, and not an artifact arising from numerical dispersion. At $N_g = 0.2$, the FCM-calculation with MORE shown in Fig. 2.18, is nearly dominated by gravity, but nevertheless by not quite as much as in the four-component result in Fig. 2.16. It would be useful to find an effective density difference, or effective vertical permeability, for equivalencing a MISTRESS calculation with gravity effects to the equivalent MORE four-component model. We first ran MISTRESS with trial values of $N_g = 0.33$ and M = 20, as illustrated in Fig. 2.19. The gravity override is too severe and the fingers are too thin. Since M = 5.0 gave the appropriate equivalencing of the mobility ratio in the nongravity case, the next MISTRESS case in Fig. 2.20 was for $N_g = 0.33$ and M = 5.0. The magnitude of gravity override is now somewhat reduced; that is decreasing the mobility ratio causes the growth rate of the gravity tongue to be reduced in favor of the fingers caused by the heterogeneous channels. An FCM-calculation in Fig. 2.21, run on MORE with M = 5.0, $N_g = 0.33$, gives a result slightly closer in appearance to the four-component model in Fig. 2.15, where the additional numerical dispersion helps the comparison. Thus we have found an *ad hoc* correction to the gravity number, which when combined with an appropriate mobility ratio, allows the FCM-calculation to essentially reproduce the compositional behavior. In summary, for cross sections with gravity effects, this work illustrates that enhanced gravity segregation rates can occur with a submiscible process, particularly at the lower gas saturations. The enhancement is of the order of a factor of three (i.e. very significant) in the problem studied. We have not yet found a simple method for predicting this equivalencing factor.

2.1.6 A Simple One-Dimensional Approximation for Heterogeneous Flows Without Gravity

We have seen that a 2D-heterogeneous MISTRESS calculation can be made to represent a MORE 2D-heterogeneous compositional problem provided an appropriate mobility ratio is used. This mobility ratio was chosen from the change in total mobility across the mobility front in Fig. 2.12, implying the need to perform a 1D-compositional calculation as a precursor to the 2D first-contact miscible case. A further step in simplifying these problems can now be contemplated. The Koval model contains the empirical parameter H, which is recommended as a measure of heterogeneity, to correct the effective mobility ratio M_e appropriate to viscous fingering in a heterogeneous system. The Koval fractional flow is given by

$$F = \frac{C}{C + (1 - C)/HM_e} \tag{2.5}$$

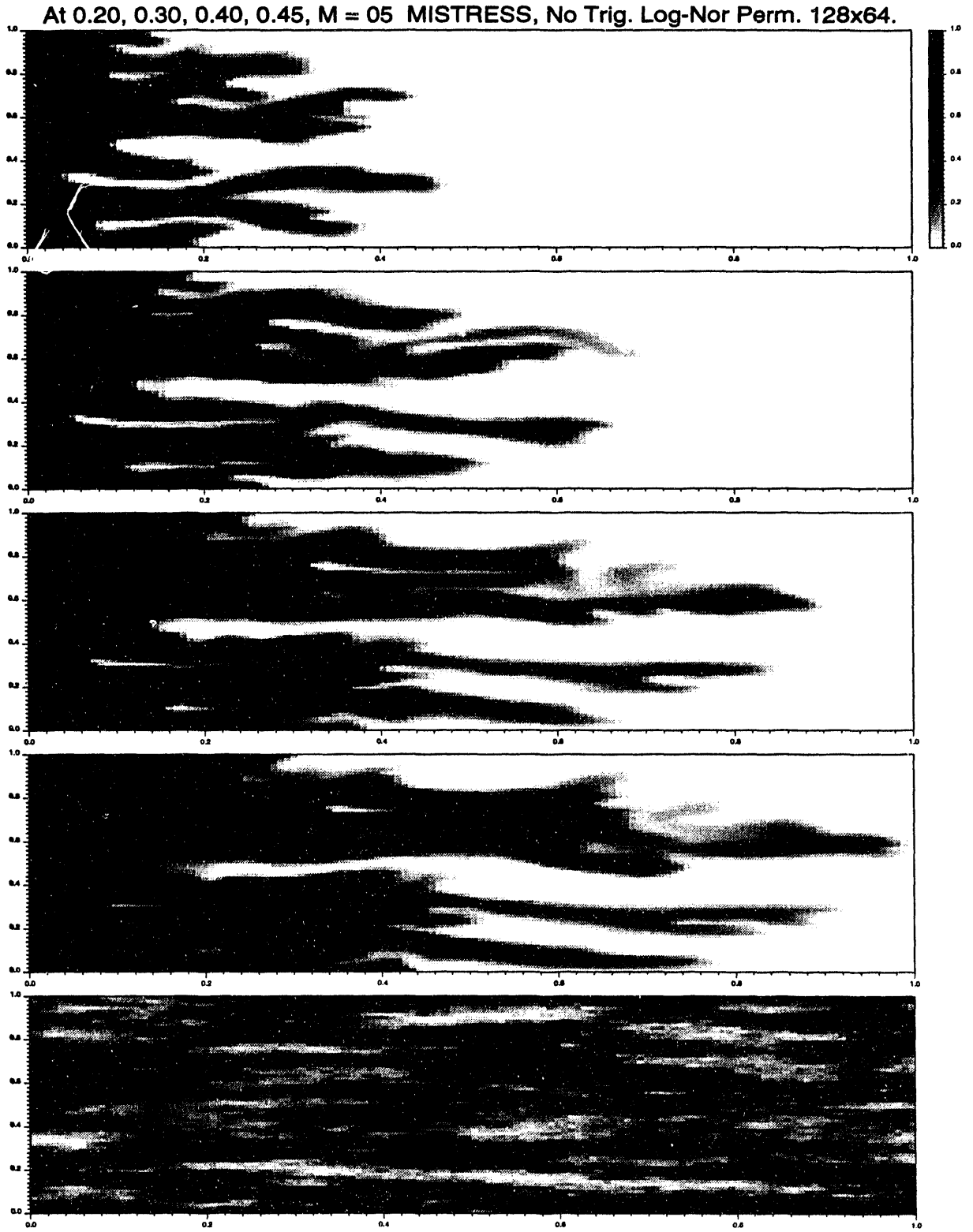

Figure 2.13: MISTRESS run with M = 5 on the fine grid (no gravity).

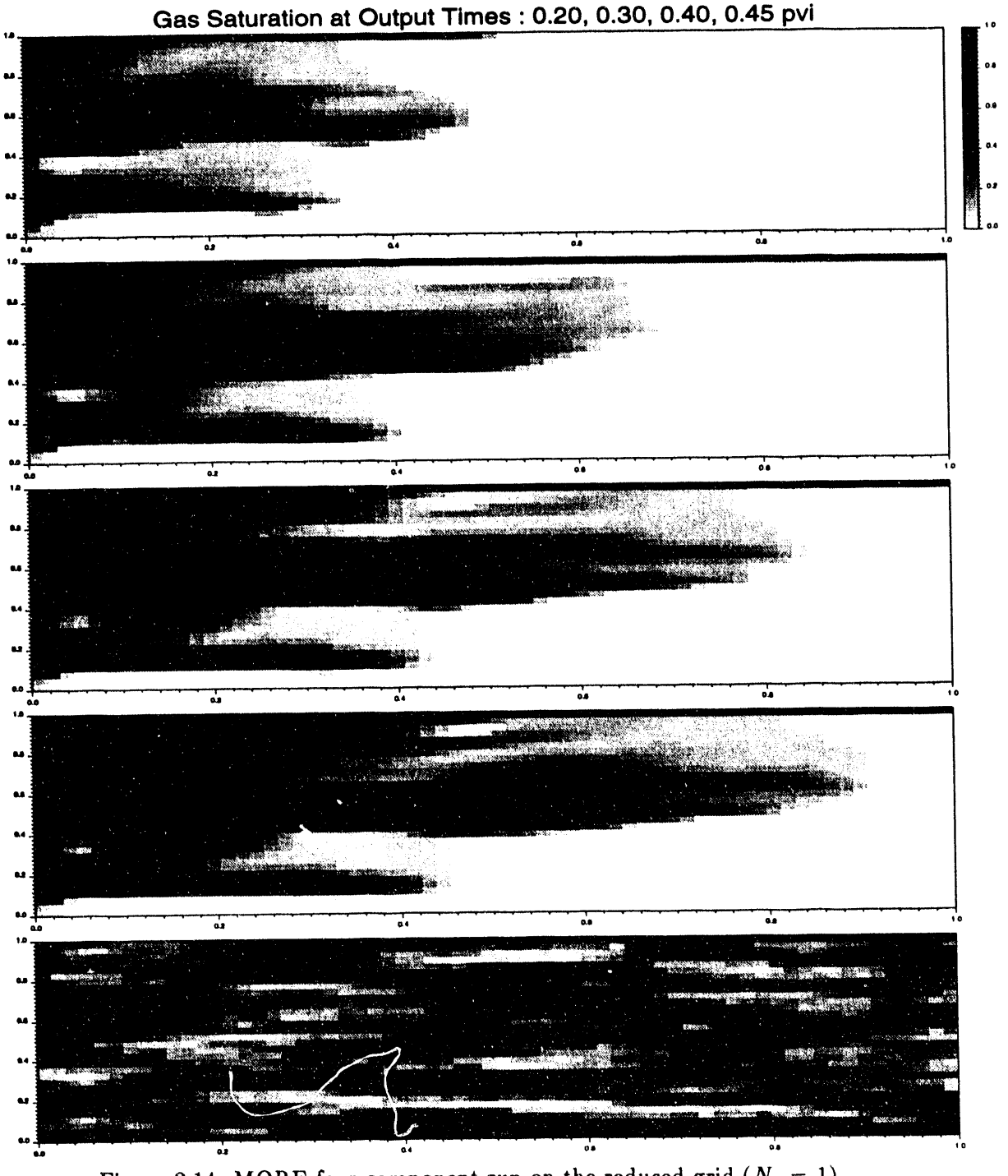

Figure 2.14: MORE four-component run on the reduced grid ($N_g = 1$).

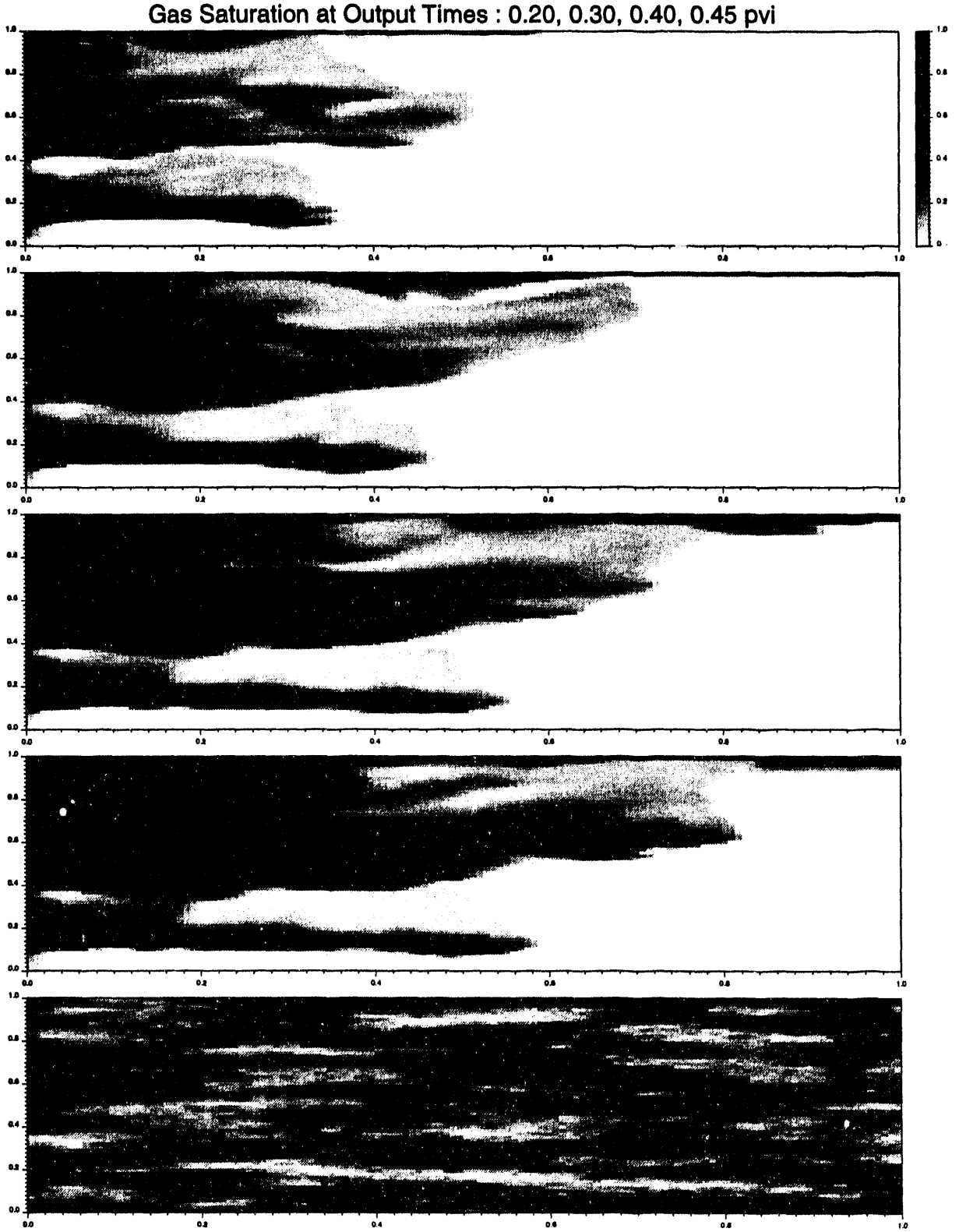

Figure 2.15: MORE four-component run on the fine grid ($N_g = 1$).

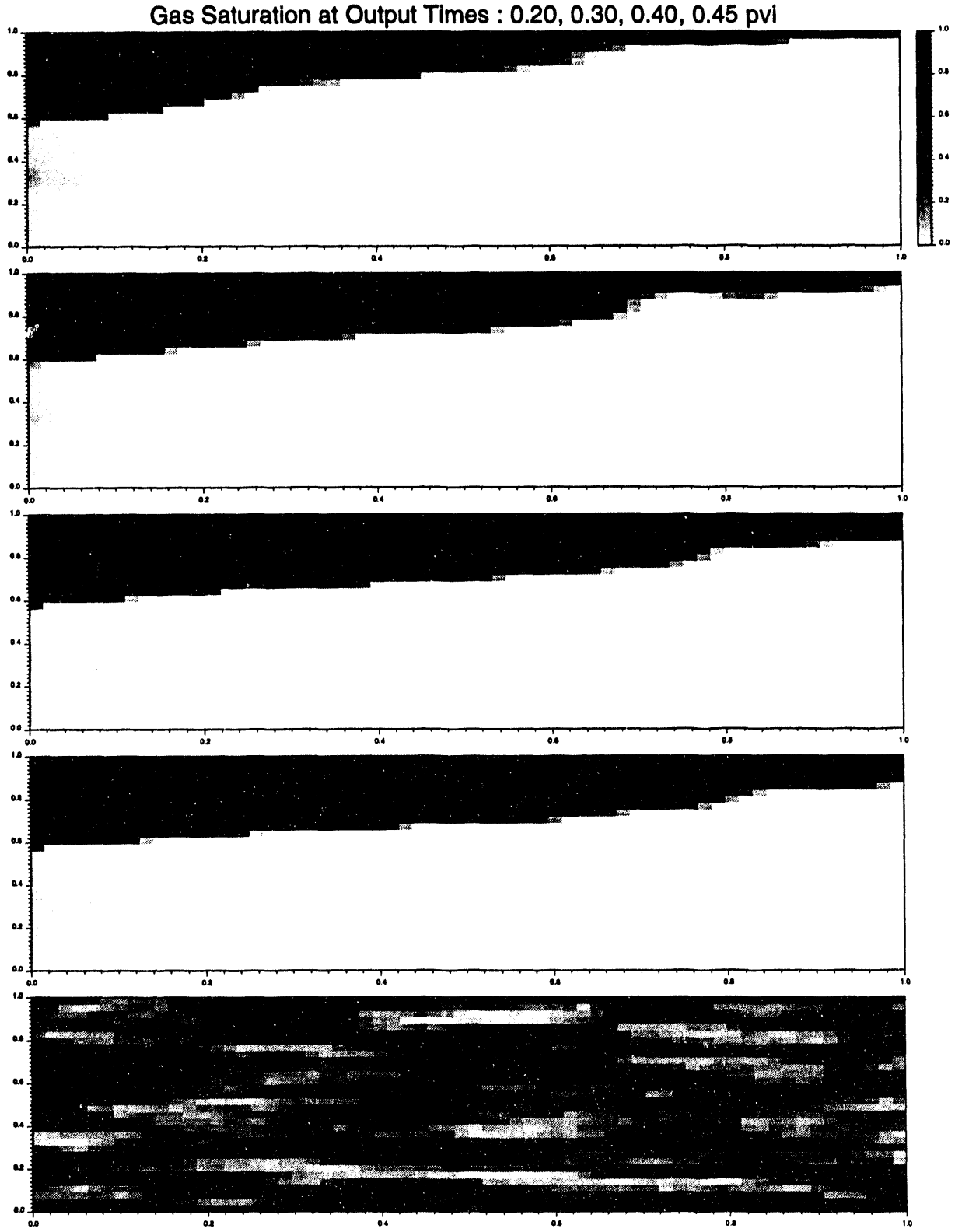

Figure 2.16: MORE four-component run on the reduced grid ($N_g = 0.2$).

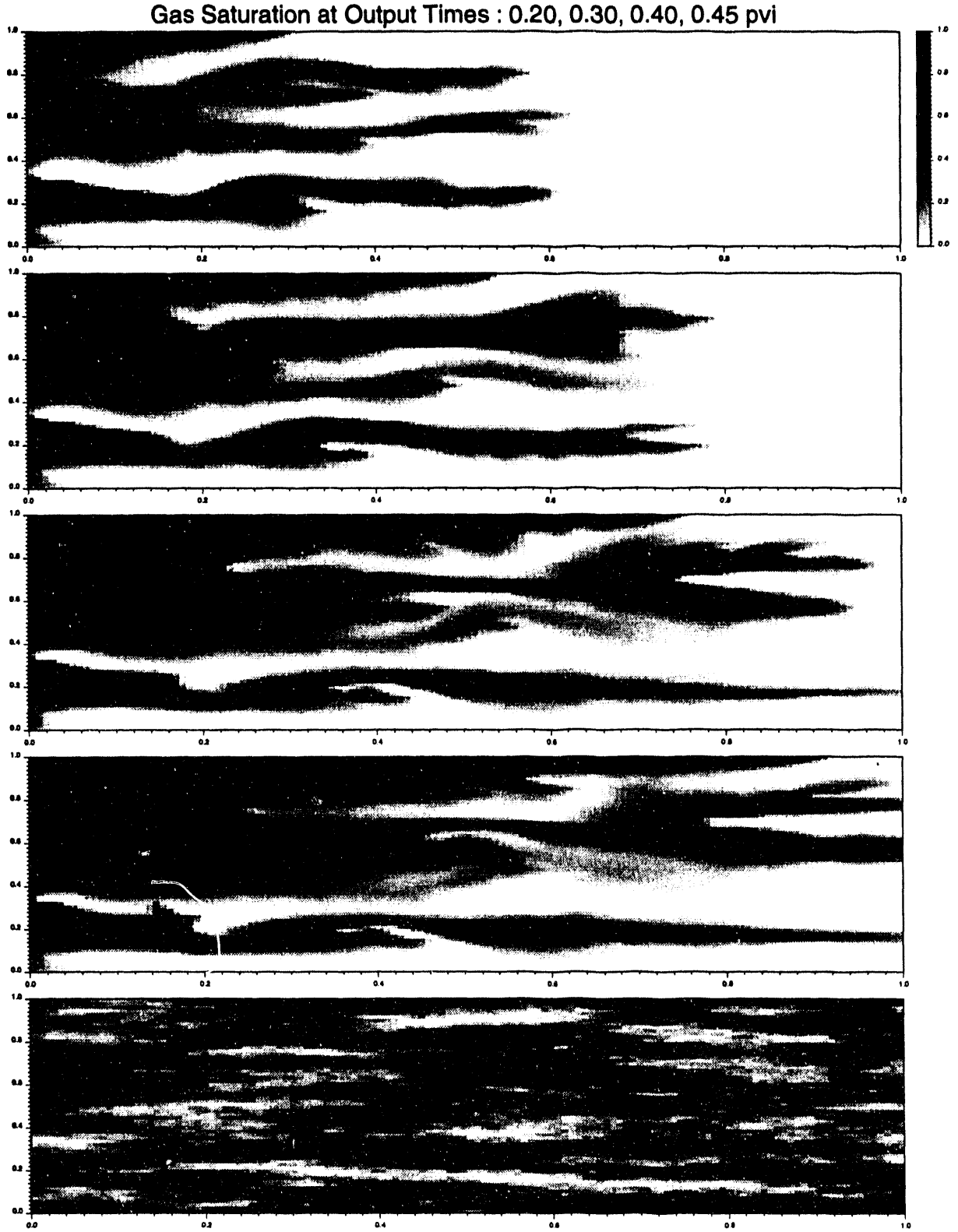

Figure 2.17: MORE "first-contact miscible" run (M = 20) on the fine grid ($N_g = 1$).

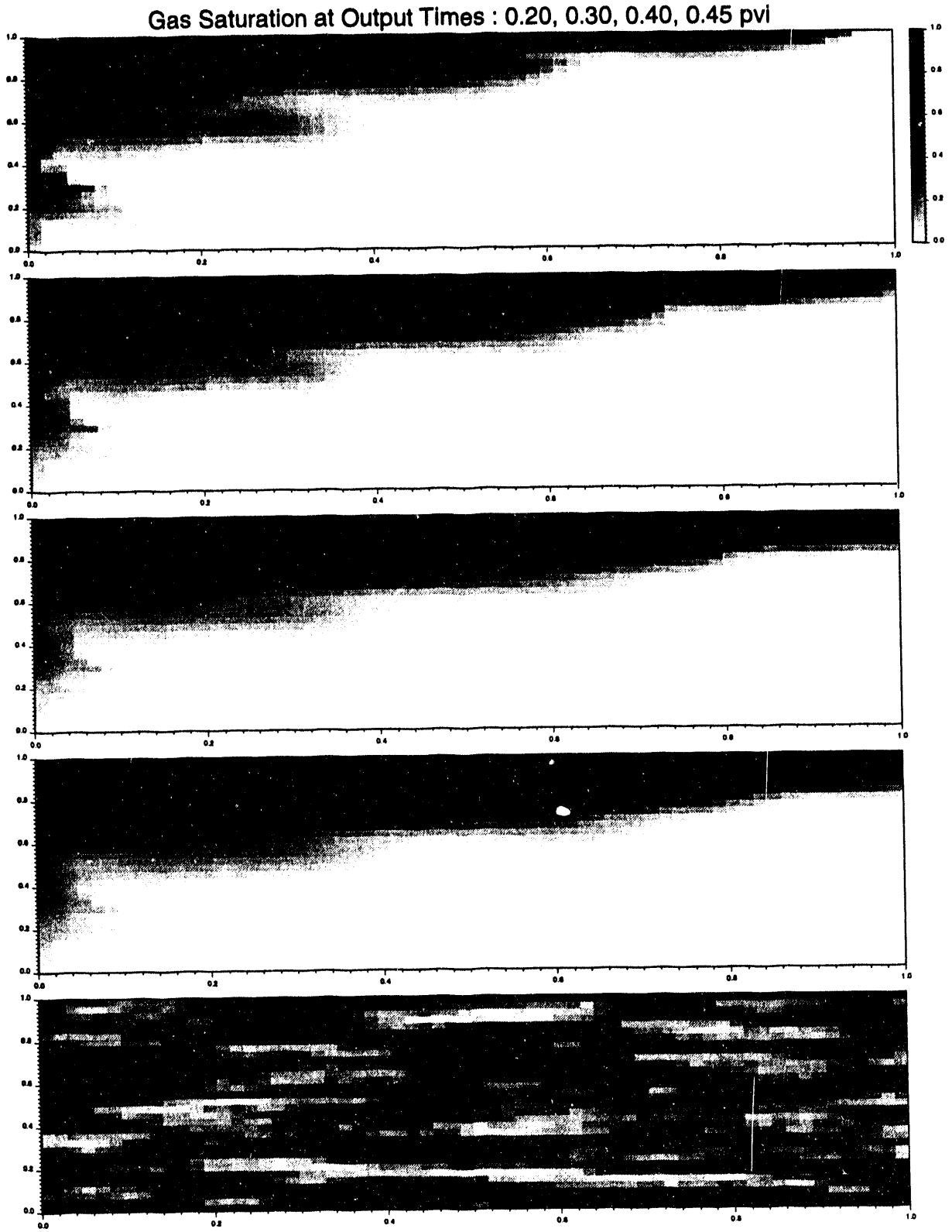

Figure 2.18: MORE "first-contact miscible" run (M = 20) on the reduced grid (N_g = 0.2).

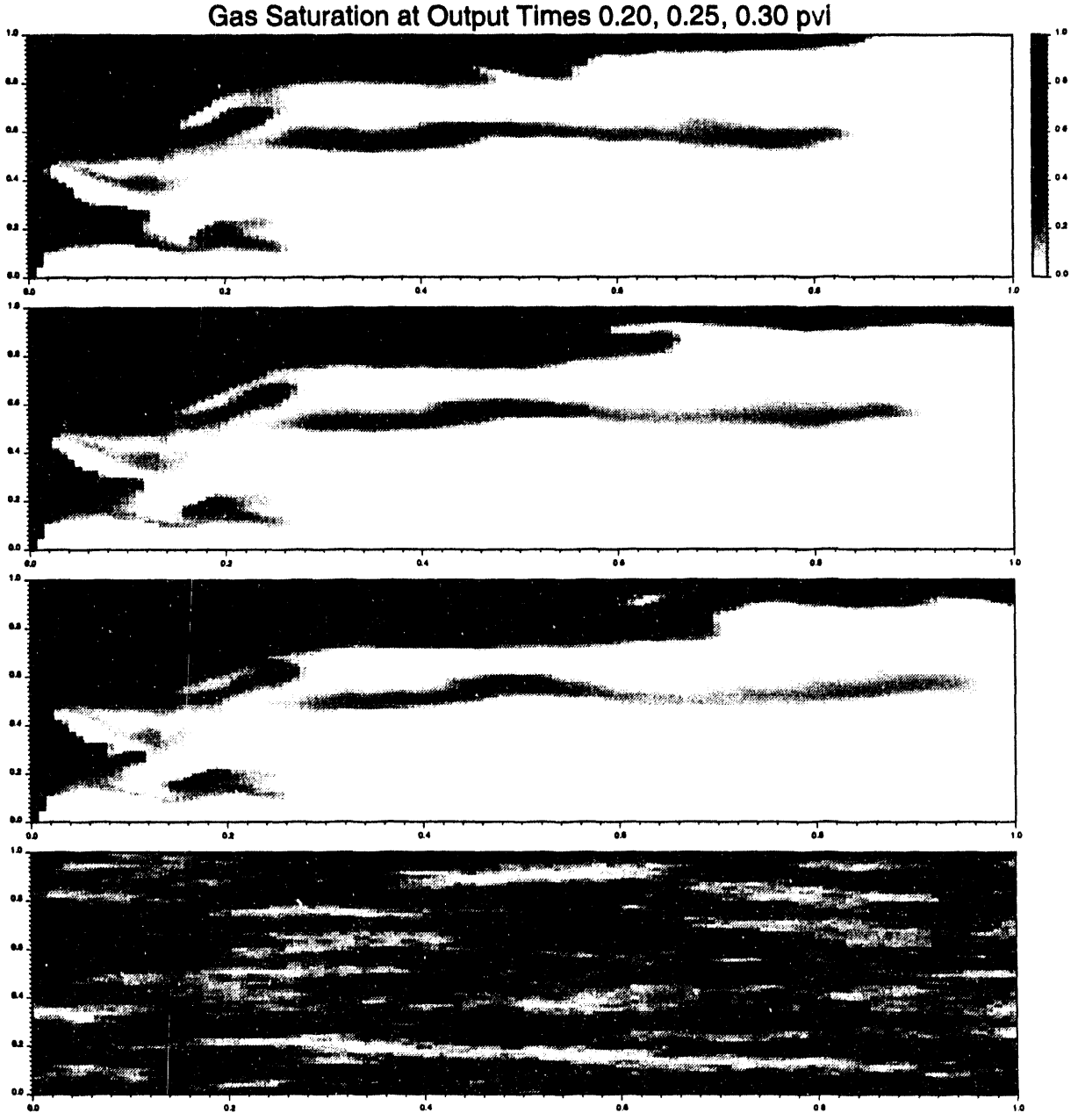

Figure 2.19: MISTRESS run with M = 20 on the fine grid ($N_g = 0.33$).

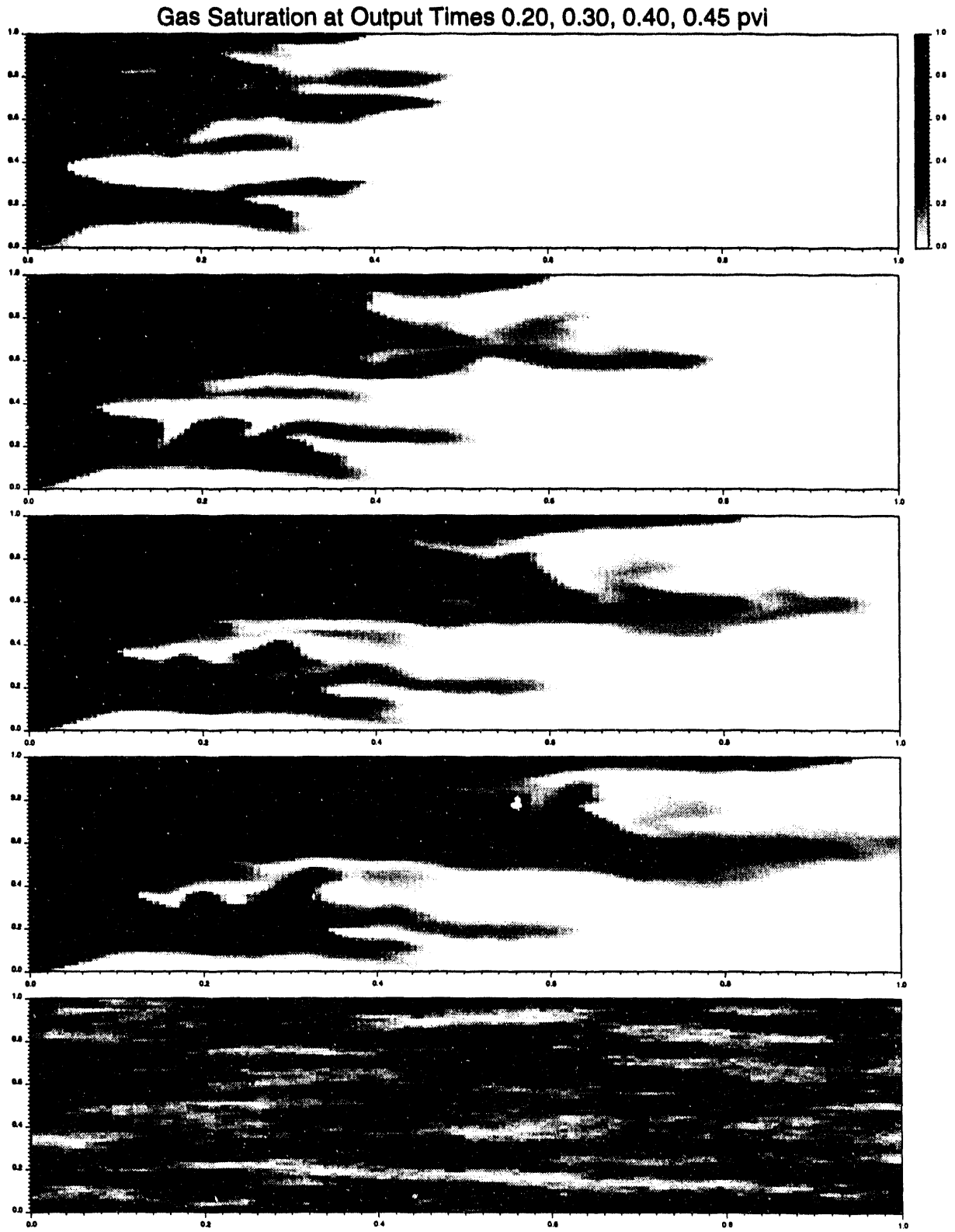

Figure 2.20: MISTRESS run with M = 5.0 on the fine grid ($N_g = 0.33$).

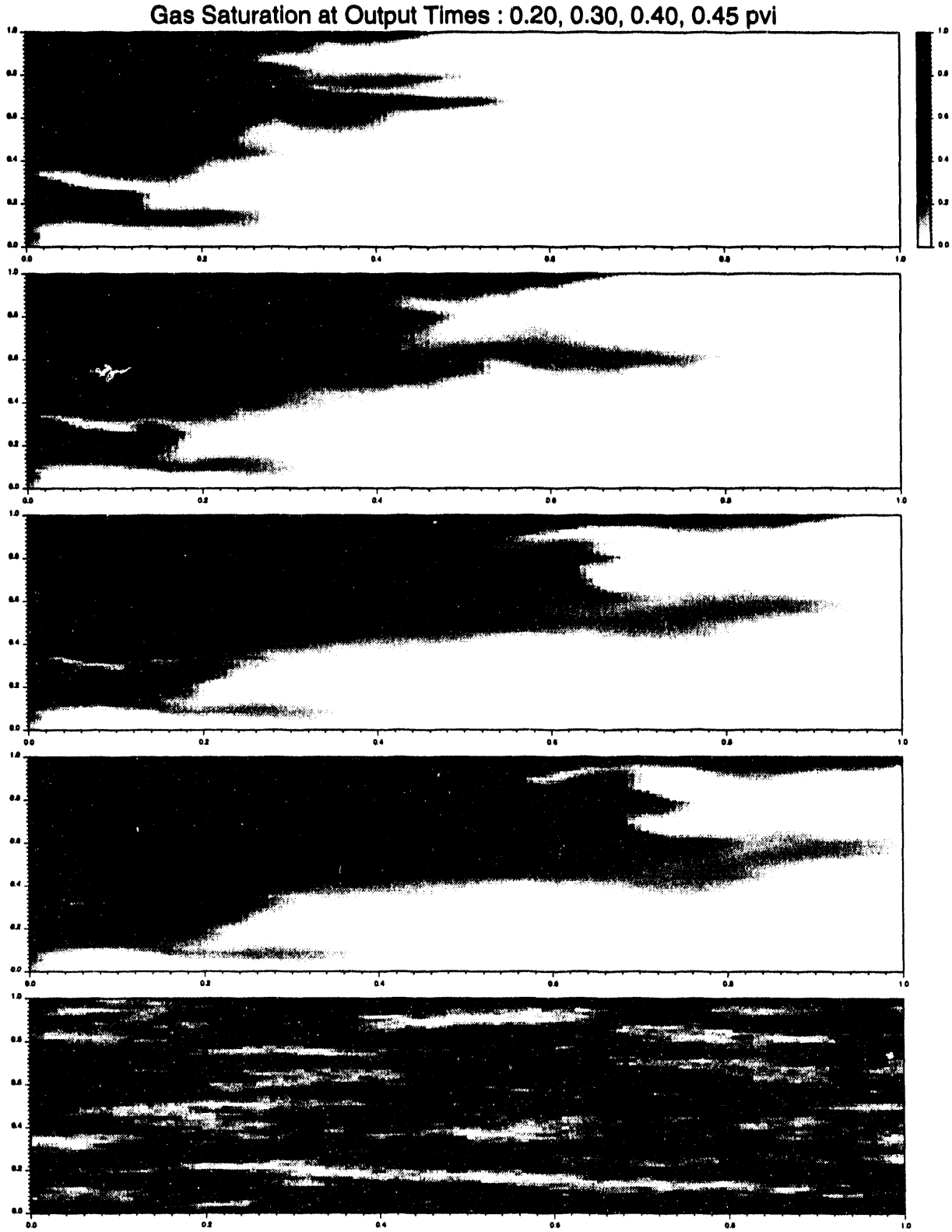

Figure 2.21: MORE "first-contact miscible" run (M = 5) on the fine grid ($N_g = 0.33$).

C is the average solvent concentration across any y-section of the 2D fingering pattern, and M_e is the Koval effective mobility ratio, given by

$$M_e = \mu_o \left(0.22\mu_g^{-1/4} + 0.78\mu_o^{-1/4}\right)^4 \tag{2.6}$$

For homogeneous (H = 1.0) viscous fingering problems, Eq. 2.5 represents the average fractional flow behavior and the consequent average C(x) profiles very well. For the submiscible problem studied in this paper, the appropriate mobility ratios are M = 5 and M_e = 1.512 from Eq. 2.6. It remains to determine the appropriate value for H for our mildly heterogeneous example. Koval recommended that H be determined by fitting to the results of a displacement calculation for the real heterogeneity distribution, run with M = 1.0. The unit mobility problem is simpler than a problem with M = 1.0, since the pressure solution (Laplace's equation) has only to be determined once. Fig. 2.22 shows MISTRESS average concentration distributions obtained for M = 1.0. These are compared with the Koval model for M = 1.0, with a reasonable choice, H = 1.5. This value of H appears to give quite a good fit. Referring back to the earlier M = 5 solution with MISTRESS in Fig. 2.13, the consequent plots of $C(x)$ and the Koval model with H = 1.5 and M_e = 1.512 are compared in Fig. 2.23. Equally good results are also obtained for M = 20, and higher mobility ratios. The need for an explicit M = 1 solution to determine an appropriate value of H could be avoided if there were some simple rule or correlation for calculating this quantity. Koval recommended use of a correlation graph, which is fitted by the equation

$$logH = \frac{V_{DP}}{(1 - V_{DP})^{0.2}} \tag{2.7}$$

This result was largely based on studies for layered systems and for our problem would give 3.75, which is far too large. Araktingi and Orr [2] suggested that an important parameter is the heterogeneity index defined by

$$H_i = \sigma^2_{logk}\alpha_l/L \tag{2.8}$$

This relation gives 0.095, which is below the cut-off suggested by Araktingi and Orr for heterogeneities to significantly influence fingering. It seems unlikely that H will be a simple function of H_i. For example, our results are for L/W = 3.0, and it is known that viscous fingering behavior is dependent on this ratio, and it will also depend on α_t/W, the dimensionless transverse correlation length.

2.1.7 Conclusions

The following conclusions appear to apply to our results for a "mildly" heterogeneous problem, although other examples of heterogeneity would need to be studied:

1. A multicomponent compositional calculation in a heterogeneous medium can be adequately represented by phase behavior from relatively few components (in the range 4-6).

2. A compositional simulator without special differencing methods [7] operated in a first-contact miscible mode, or in a multicomponent mode with straight-line relative permeabilities, will show severe numerical dispersion at low gas saturations, although this is less pronounced at higher saturations. When used with conventional immiscible relative permeabilities, a multicomponent calculation appears to give acceptable dispersion errors.

3. Near-miscible heterogeneous problems run in a compositional framework do not appear to give low enough interfacial tensions to justify use of modified relative permeabilities. This is not likely to be true for capillary pressures for problems at smaller scale sizes [23].

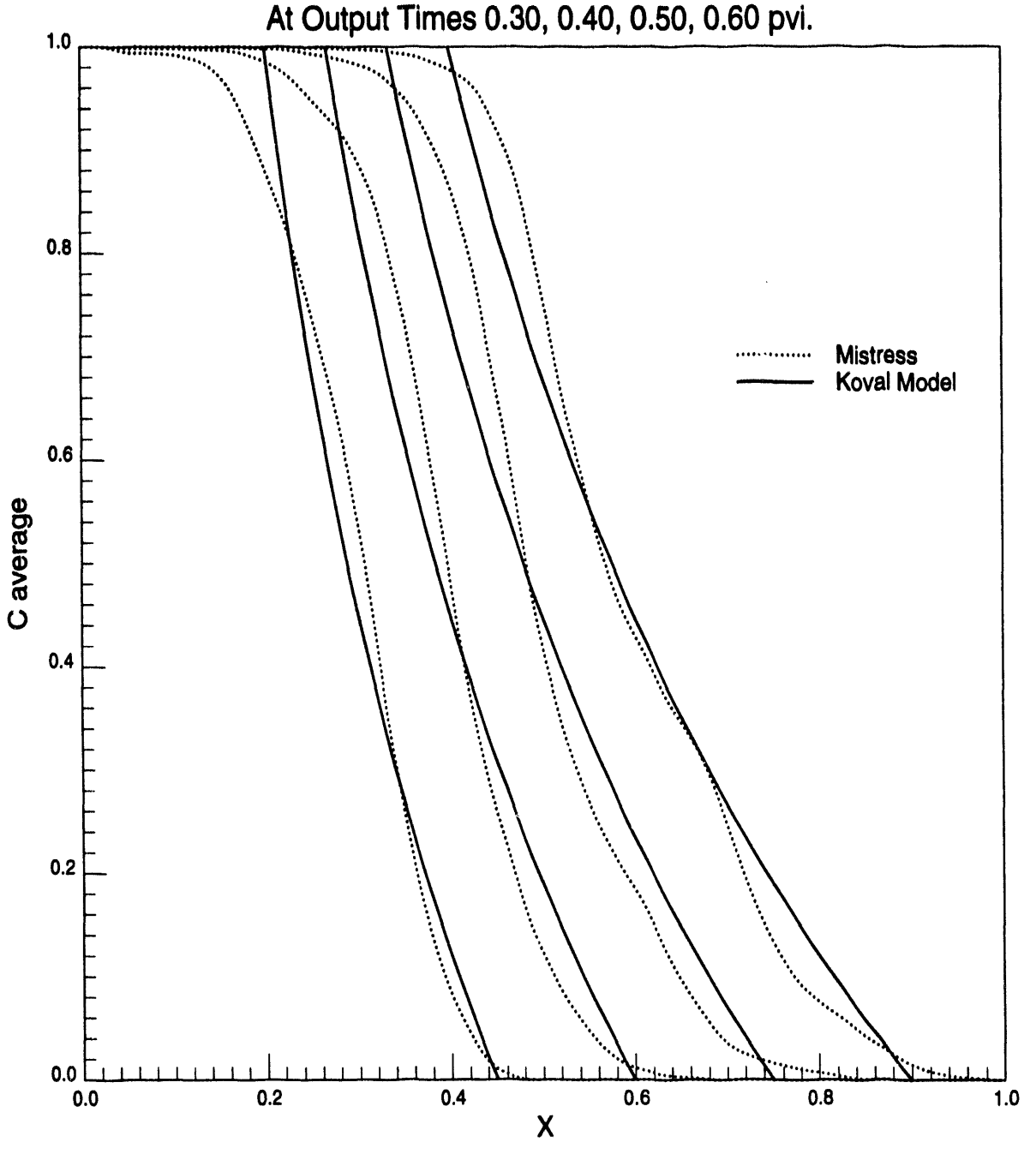

Figure 2.22: Comparison of MISTRESS average concentration profiles with Koval model for M = 1.0 and H = 1.5.

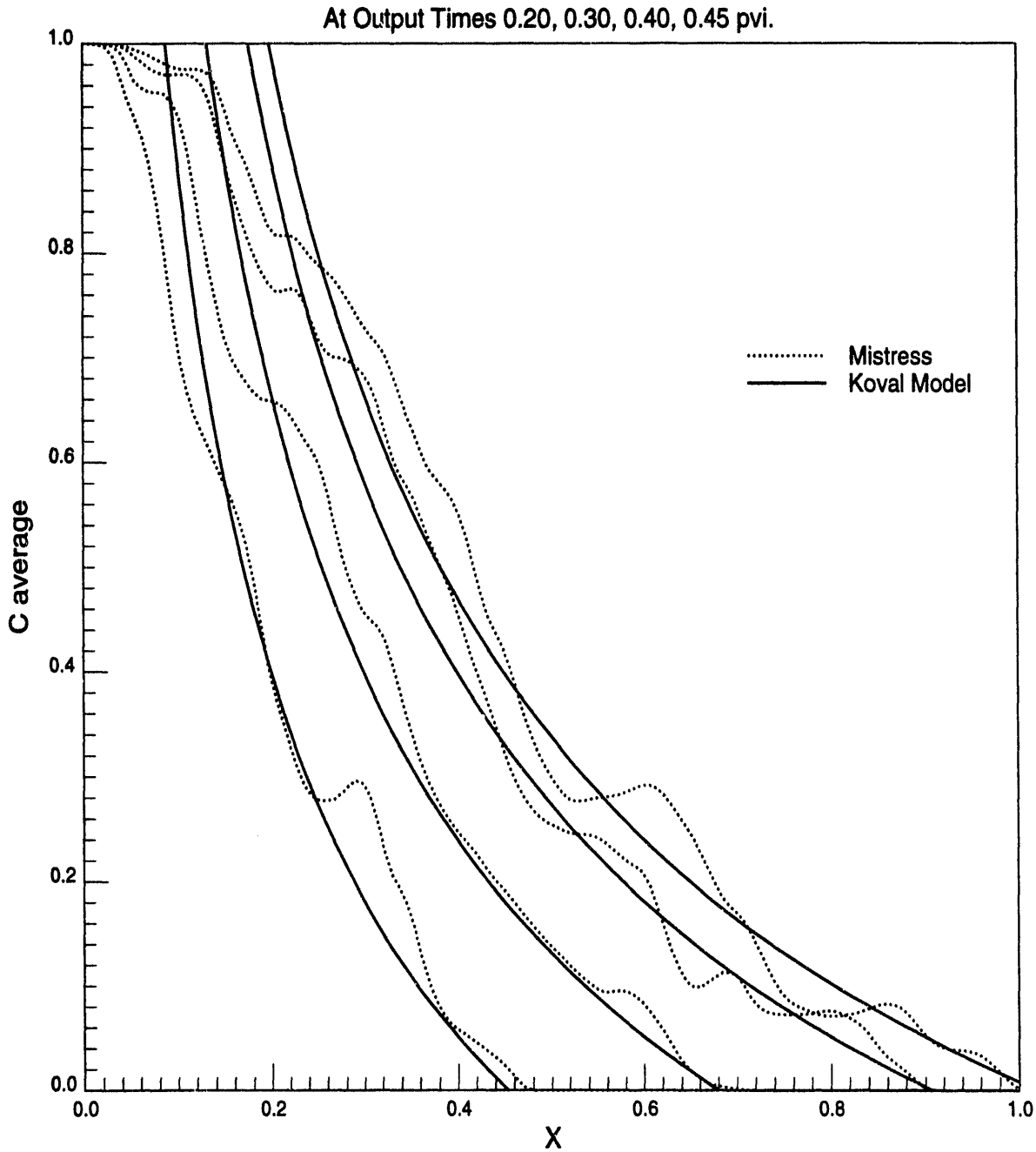

Figure 2.23: Comparison of MISTRESS average concentration profiles with Koval model for M = 5.0 and H = 1.5.

4. First-contact miscible calculations run at the initial fluid mobility ratio show much more adverse viscous fingering in a heterogeneous system than their compositional equivalent, i.e. miscible displacement is less unstable than initial estimates may suggest.

5. An effective mobility ratio can be found for running a nongravity heterogeneous problem in a first-contact miscible mode. This mobility ratio is given by the shock front change in total mobility from an accurate 1D-solution.

6. The first-contact miscible solution for the nongravity heterogeneous problem is well represented by a Koval model with H chosen from the $M = 1$ solution. Better understanding is needed of the factors which control H.

7. Heterogeneities interact strongly with gravity segregation and reduce the magnitude of the latter. Increasing the mobility ratio increases the gravity override for a constant gravity number.

2.2 Interactions of Viscous Fingering, Permeability Heterogeneity and Gravity Segregation in 2D and 3D Flow in Porous Media

H.A. Tchelepi and F.M. Orr, Jr.

2.2.1 Introduction

Viscous fingering, gravity segregation, and reservoir heterogeneity have long been known to affect the performance of the collection of gas injection processes known as miscible floods [63]. Numerical simulations of viscous fingering and gravity segregation have been performed by some investigators to examine the transition from gravity-dominated flow, in which a single gravity tongue forms and early breakthrough of injected fluid occurs, to flow dominated by viscous fingering. Most calculations have been performed only for two-dimensional cross sections, however.

Only recently have investigations of 3D fingering begun. Withjack *et al.* [70] presented 3D computed tomography images from a series of unstable miscible displacement experiments in a 5-spot geometry such that buoyancy in the vertical plane was in competition with the viscous forces in the horizontal plane. They found that recovery correlations for 5-spot geometry based on 2D information overestimate the observed 3D recoveries from the experiments.

Zimmerman [76] simulated growth of viscous fingers in homogeneous porous media in the absence of gravity segregation under conditions of isotropic dispersion using a spectral technique. He found that transversely averaged concentration profiles were similar in 2D and 3D simulations. Christie *et al.* [15] investigated both fingering and gravity segregation in homogeneous media as well as those in which a distribution of shales was also present. In all their calculations, buoyancy forces were quite strong. They found that breakthrough occurred slightly earlier and recovery was slightly lower in 3D flow than in 2D flow. Christie *et al.* [15] did not investigate the transition from gravity-dominated to viscous-dominated flow.

Chang *et al.* [12] performed 2D and 3D simulations of laboratory displacement experiments and found that calculated recovery curves differed only slightly. Mohanty and Johnson [43] simulated corefloods performed in heterogeneous cores. They found that 2D simulations were not good approximations for layered systems with only modest contrast in permeability between layers and found better agreement when 3D simulations were performed.

Because 3D simulations are significantly more expensive to perform than 2D simulations, it would be useful to know when 2D calculations can be used with confidence to predict performance

of reservoir displacement processes. In this paper we report results of simulations that examine when 2D simulations reproduce the behavior of 3D flow and, more importantly, when they do not.

The simulations described here were performed with a particle-tracking technique described in detail by Araktingi and Orr [4], Tchelepi and Orr [64], and Tchelepi *et al.* [65]. Brock and Orr [10] showed that the simulator reproduces accurately the transition from flow controlled by viscous fingering in a 2D homogeneous porous medium to flow controlled by the permeability distribution in heterogeneous porous media. Araktingi and Orr [3] showed that the simulator accurately represents the effects of gravity in 2D flow as well. Thus, the simulator used has been tested extensively against experimental data where available and has been shown to model accurately the effects of heterogeneity, viscous instability, and gravity segregation. In the remainder of this paper, we examine a succession of unstable 2D and 3D displacements to determine when 3D flow differs substantially from 2D flow.

Simulations were performed for flow in a rectangular porous medium with width equal to the height. Unless otherwise stated, the aspect (length to height) ratio was set to L/H = 4. The 3D simulations were performed on 128 x 64 x 32 grids, with 64 particles taken to represent a unit concentration. For 2D simulations, 128 x 64 grids were used. Extensive grid refinement tests showed that no significant changes in results were observed for finer grids. The grids used here were significantly finer in the vertical and transverse horizontal directions than those used by previous investigators. Longitudinal and transverse Peclet numbers were set to 505 and 3750 respectively, a dispersion anisotropy of 30. The computations were performed on massively parallel machines with 8192 or 4096 processors (MasPar, Inc.). The algorithms that implement the model were designed to take advantage of the speed of parallel processing in moving particles. Typical simulation times for the 3D computations were about 5 hours of CPU time.

2.2.2 Homogeneous Porous Media

Displacements without Gravity

A comparison of 2D and 3D displacements in a homogeneous porous medium with viscosity ratio, M, set to 30 is shown in Fig. 2.24. It compares the pattern of viscous fingers in a 2D simulation with several horizontal and vertical slices through the 3D porous medium. Fig. 2.24 shows that in both 2D and 3D, fingers have dimensions and spacing that are nearly the same, though fingers have penetrated slightly farther in 3D. Furthermore, in the absence of gravity, the numbers of fingers and their widths are essentially equal in the horizontal and vertical directions. That result is reasonable because finger dimensions are determined by the level of transverse dispersion, mobility ratio and flow length, factors that act equivalently in 2D and 3D flow.

Another comparison of 2D and 3D fingering is given in Fig. 2.25. It compares concentration profiles obtained by averaging the concentrations of fluid present at a given longitudinal position, again for M = 30. Fig. 2.25 shows that the longitudinal concentration distributions are remarkably similar in 2D and 3D flow in the absence of gravity. The 2D distributions are noisier, presumably because concentrations are averaged over fewer fingers in 2D than in 3D, but otherwise the distributions do not differ in any significant way.

Displacements with Gravity

When gravity is added to the picture, the equivalence of 2D and 3D flow disappears for some displacements. In both 2D and 3D flow, of course, viscous forces that drive the hydrodynamic instability compete with buoyancy forces that act to create a gravity tongue. If the flow is slow enough that gravity forces dominate, then fingering will be suppressed. If the flow is fast enough that viscous forces dominate, then fingers form and the gravity tongue is suppressed. The relative

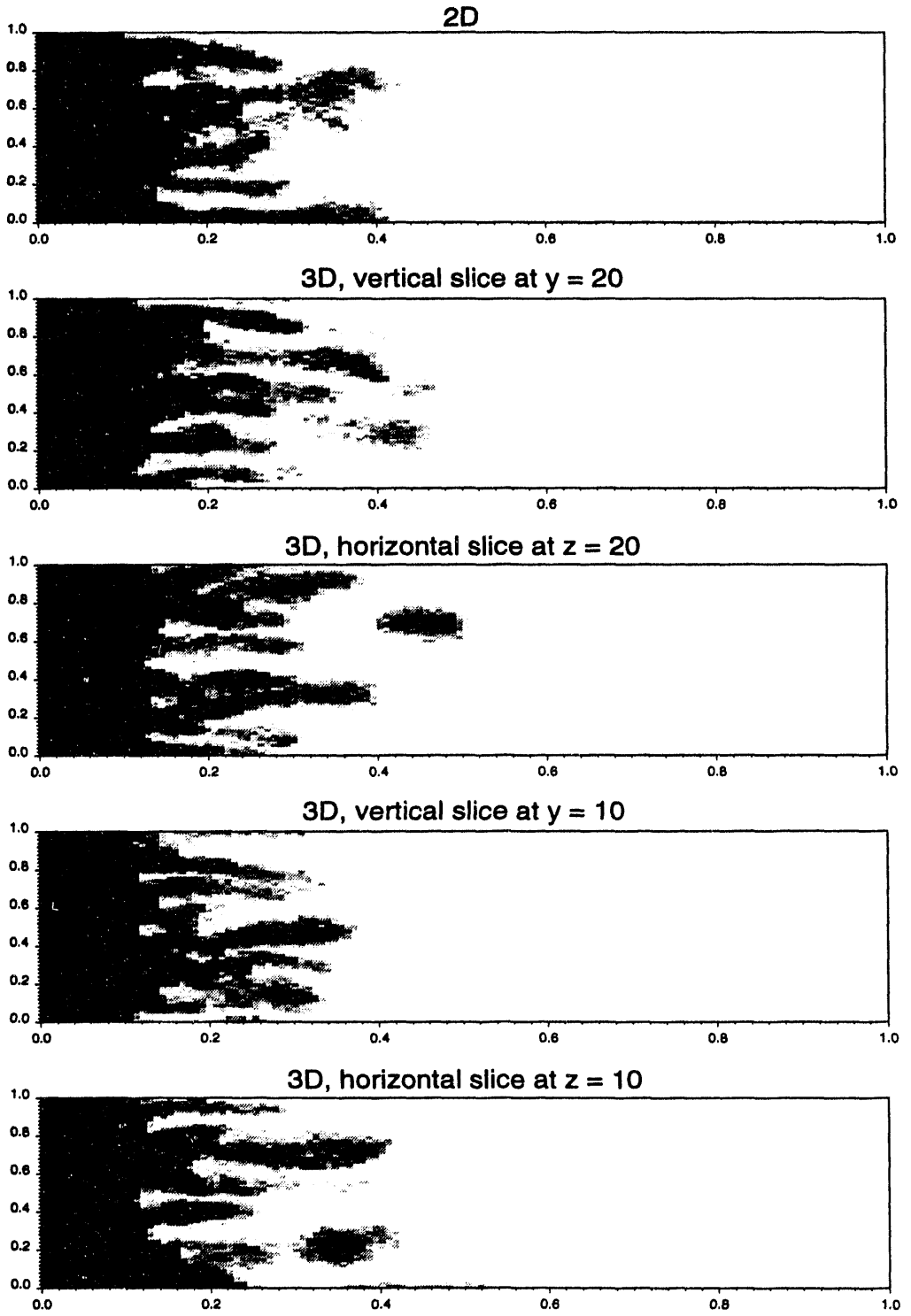

Figure 2.24: Comparison at 0.2 PVI of 2D and 3D displacements with M = 30 in a homogeneous porous medium in the absence of gravity.

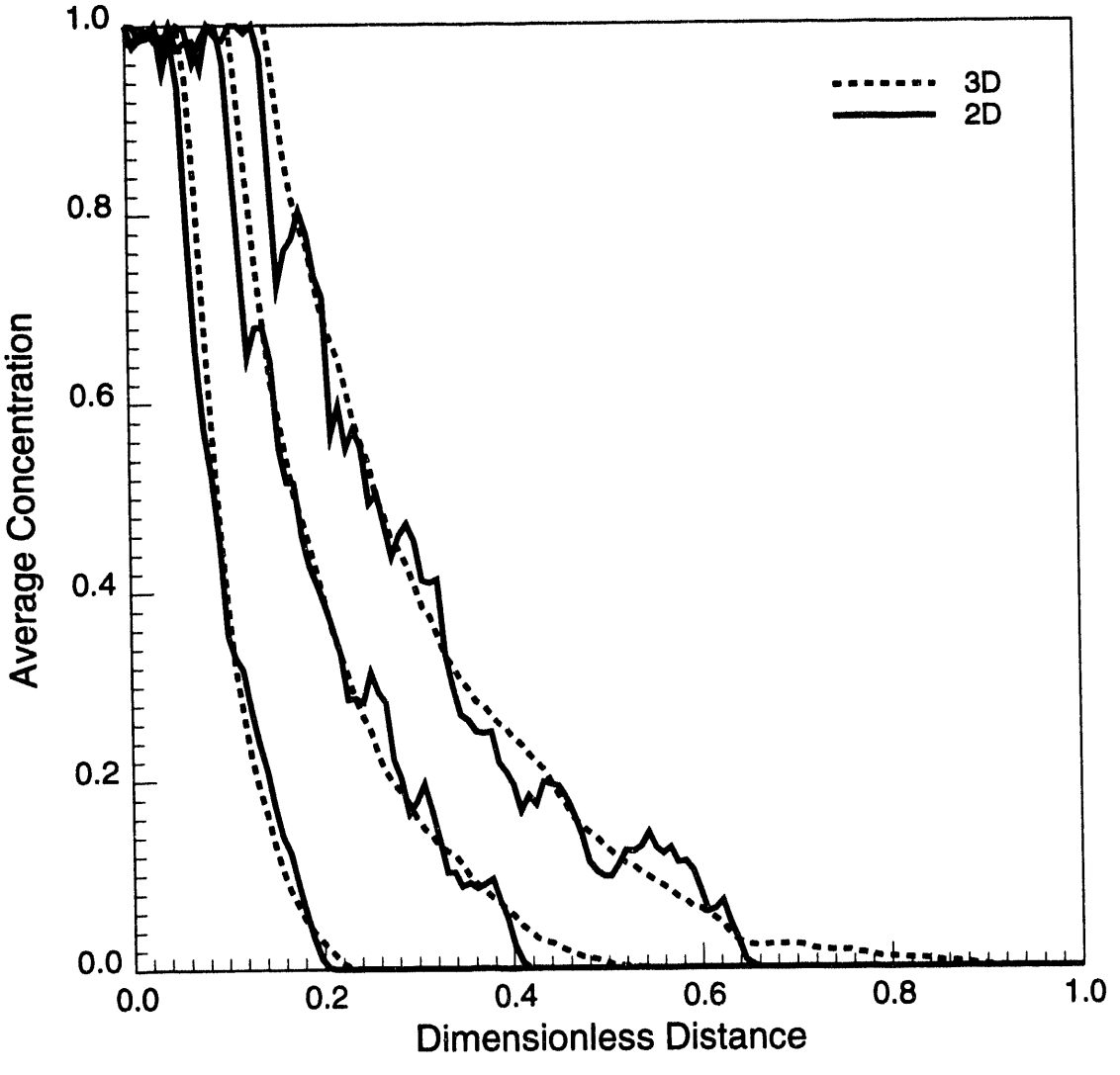

Figure 2.25: Comparsion of transversely averaged concentrations of injected fluid in 2D and 3D displacements with M = 30 at 0.1, 0.2 and 0.3 PVI in a homogeneous porous medium in the absence of gravity.

importance of viscous and gravity forces is measured by a viscous to gravity ratio, $R_{v/g}$. Here we use the definition of Fayers and Muggeridge [27],

$$R_{v/g} = 2\frac{v\Delta\mu}{\Delta\rho g k_z}\frac{H}{L} \tag{2.9}$$

$R_{v/g}$ as defined in Eq. 2.9, without the leading coefficient of 2, can be rigorously derived from the governing equations. $R_{v/g}$ is interpreted as a ratio of characteristic times. It is the ratio of the time it takes a particle to traverse the height of the model, to the time it takes the particle to cover the length of the medium when driven by the mean viscous force at $\overline{u}$. In addition to the obvious fact that segregation requires a density difference, the viscous-to-gravity ratio, $R_{v/g}$, indicates that the following factors, when dispersion is negligible, add to the effectiveness of buoyancy. (1) Slow average displacement velocities, (2) large vertical communication and (3) longer, thinner domains.

The transition from flow dominated by a single gravity tongue to flow dominated by viscous fingering is illustrated for 2D flow in Fig. 2.26. At $R_{v/g} = 1$ and 2, the flow is strongly influenced by gravity-driven vertical flow, which causes a thin gravity tongue to form. As $R_{v/g}$ is increased further, however, viscous fingers begin to form, and the gravity tongue loses strength and becomes smaller. The $R_{v/g} = 5$ and $R_{v/g} = 10$ displacements in Fig. 2.26 are in the transition region where buoyancy and viscous fingering compete for dominance. Finally, when $R_{v/g} = 20$, viscous fingering dominates the flow.

Fig. 2.27 compares 2D and 3D flow for M = 30 and $R_{v/g} = 20$. While there is no evidence of a gravity tongue in the 2D flow, all three vertical slices of the 3D flow show some evidence of gravity override. Fig. 2.28 is a 3D perspective at 0.3 PVI of the M = 30 displacement when $R_{v/g}$ = 20. The presence of a gravity tongue is evident in Figs. 4 and 5. In addition, some of the fingers below the gravity tongues in the 3D flow appear to have been deflected upward by gravity. Apparently, gravity segregation remains important at $R_{v/g} = 20$ for M = 30 in 3D flow, while its effect in 2D flow is virtually absent.

Another indication of the larger effect of gravity in 3D flow is given in Fig. 2.29, which reports recovery at breakthrough of injected solvent for both 2D and 3D flows. In 2D flow, breakthrough recovery increases with $R_{v/g}$ up to about $R_{v/g} = 10$. In 3D flow, however, breakthrough recovery is lower than that for 2D flow (at the same value of M), and the effect of gravity persists to higher values of $R_{v/g}$. In fact, only above $R_{v/g} = 100$ does the effect of gravity on breakthrough recovery disappear.

The effect of gravity on recovery after breakthrough is shown for M = 30 in Fig. 2.30. It shows that for L/H = 4, there is little difference between the 2D and 3D displacements after breakthrough for $R_{v/g} = 5$. As the flow length is increased, the weaker influence of buoyancy in 2D flow gives way to the effects of lateral dispersion and viscous fingering. Hence, when L/H is increased to 16, there is a substantial difference between 2D and 3D flow, as the longer flow length provides more time for gravity segregation, which is more effective for a given $R_{v/g}$ in 3D than in 2D, to take effect.

Fig. 2.31 provides further evidence of the increased effectiveness of gravity segregation in 3D than in 2D at the same value of $R_{v/g}$. Fig. 2.31 is a 3D snapshot for M = 30 and L/H = 4 for $R_{v/g}$ = 100 just before breakthrough. The effect of buoyancy on 3D flow at this high viscous-to-gravity ratio is reflected in preferred fingering near the top of this relatively short model. We saw in Fig. 2.26 that buoyancy was no longer effective in 2D flow at M = 30 and L/H = 4 when $R_{v/g}$ was 20. The enhanced effectiveness of gravity segregation in 3D flow was experimentally observed by Withjack *et al.* [70] in unstable miscible displacements in a 5-spot geometry.

We offer the following explanation for the difference between 2D and 3D flow behavior in the transition region of $R_{v/g}$ where both gravity and viscous forces influence the flow. In unstable 2D flow (see Fig. 2.26) at intermediate values of $R_{v/g}$, the effect of gravity is to cause upward flow

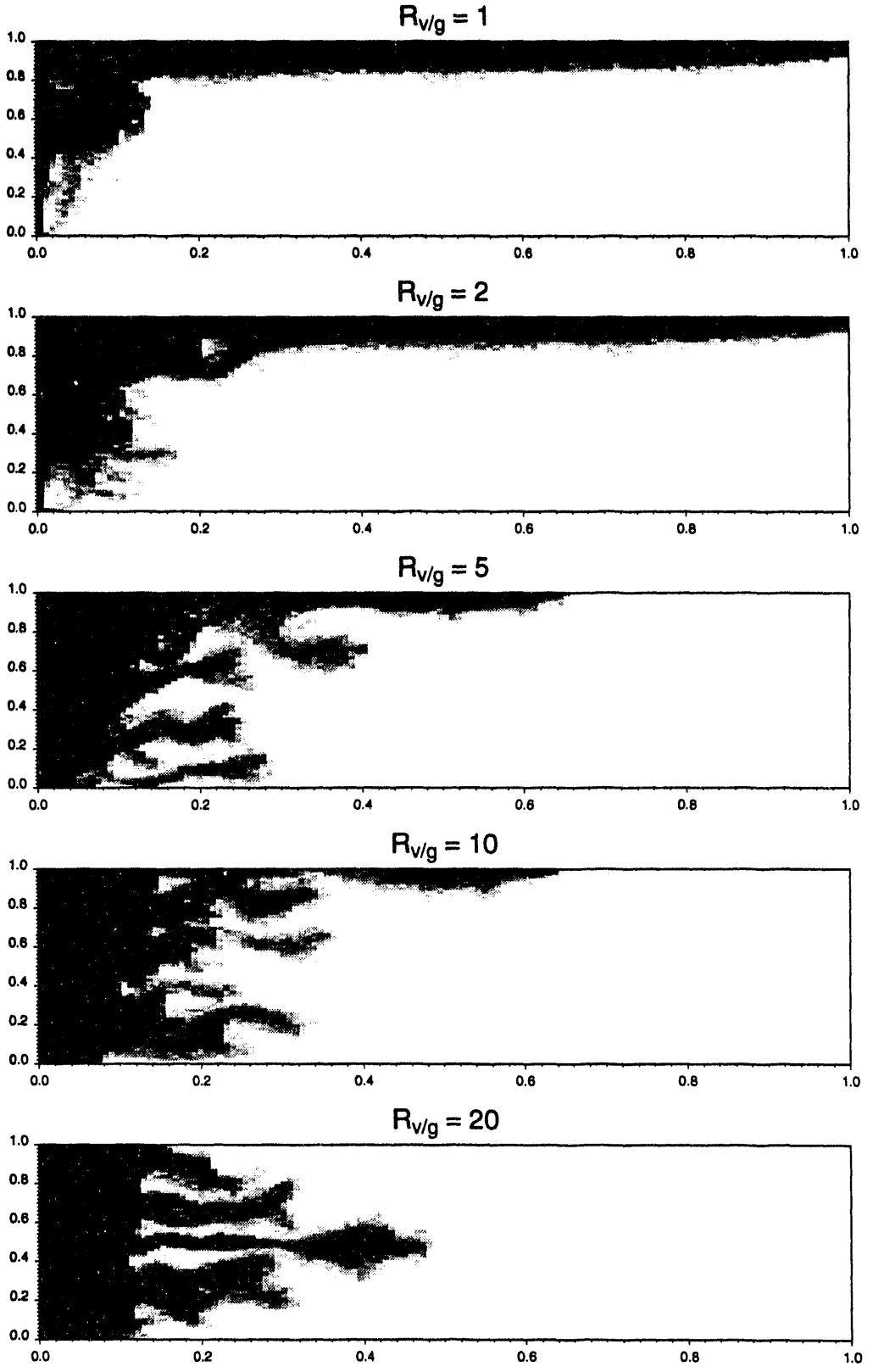

Figure 2.26: Effect of viscous to gravity ratio, $R_{v/g}$, in 2D displacements for M = 30 at 0.2 PVI.

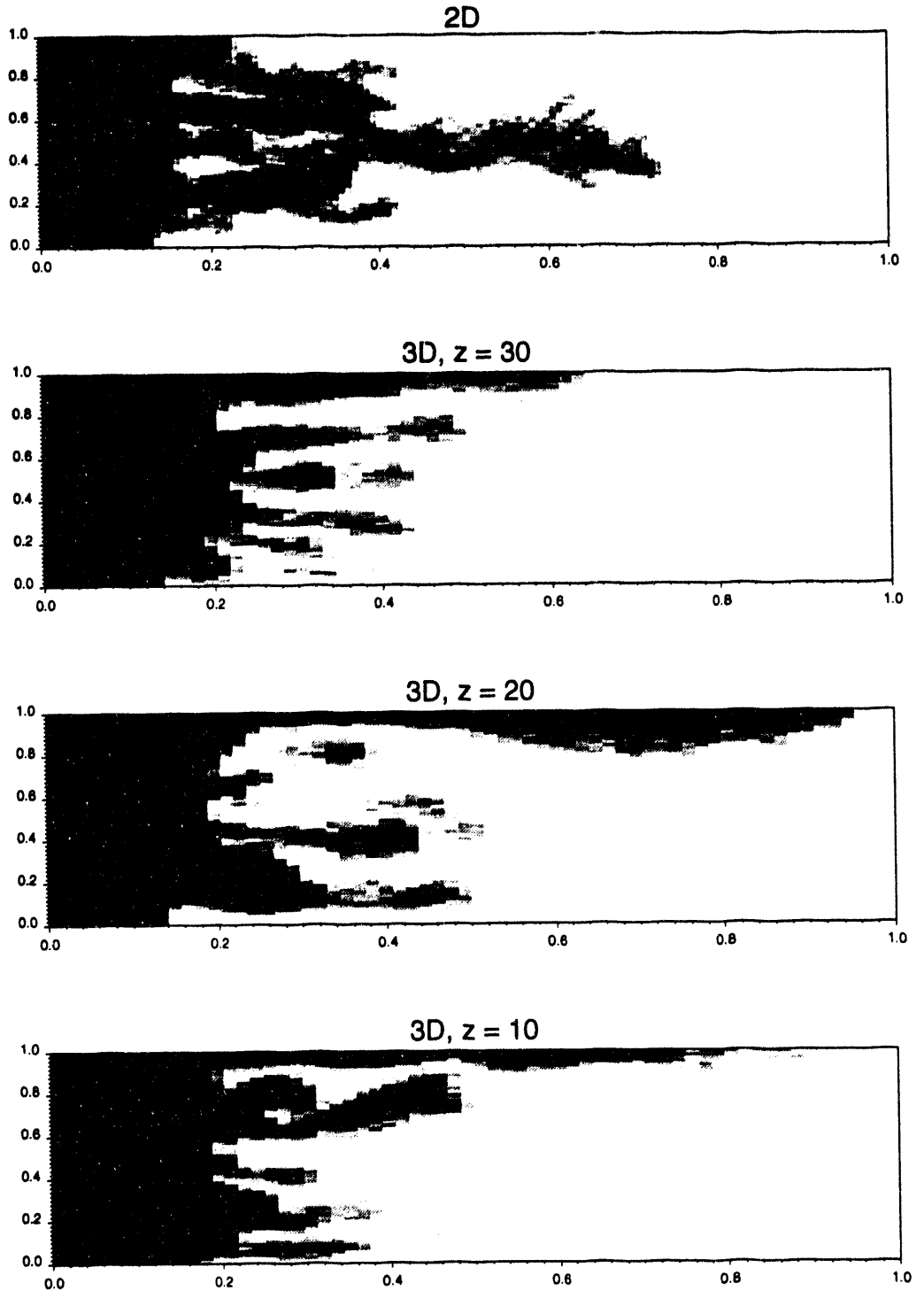

Figure 2.27: Comparison at 0.3 PVI of 2D and 3D displacements with M = 30 and $R_{v/g} = 20$ in a homogeneous porous medium.

M = 30, Rvg = 20, PVI = 0.3

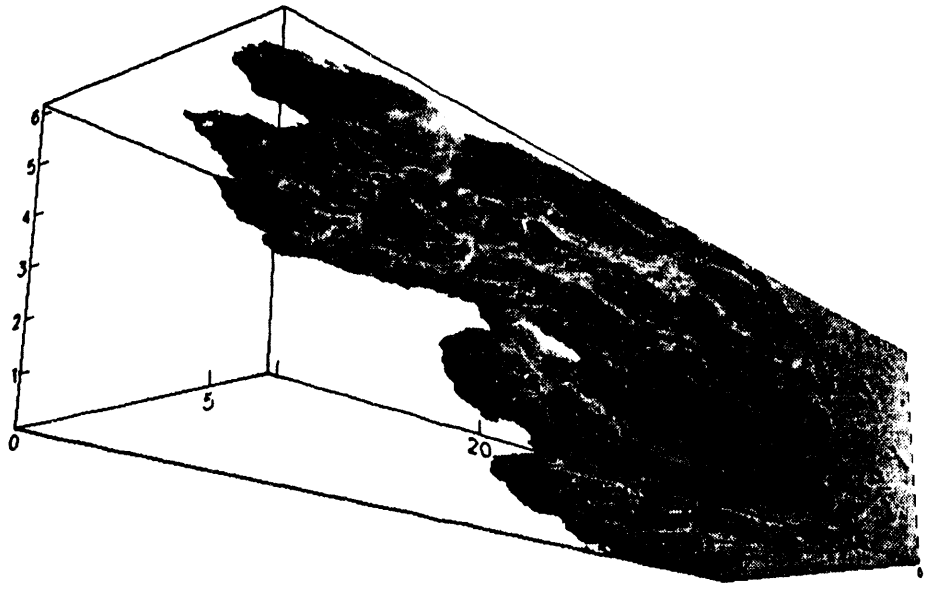

Figure 2.28: A 3D snapshot for M = 30 and $R_{v/g}$ = 20 in a homogeneous porous medium at 0.3 PVI.

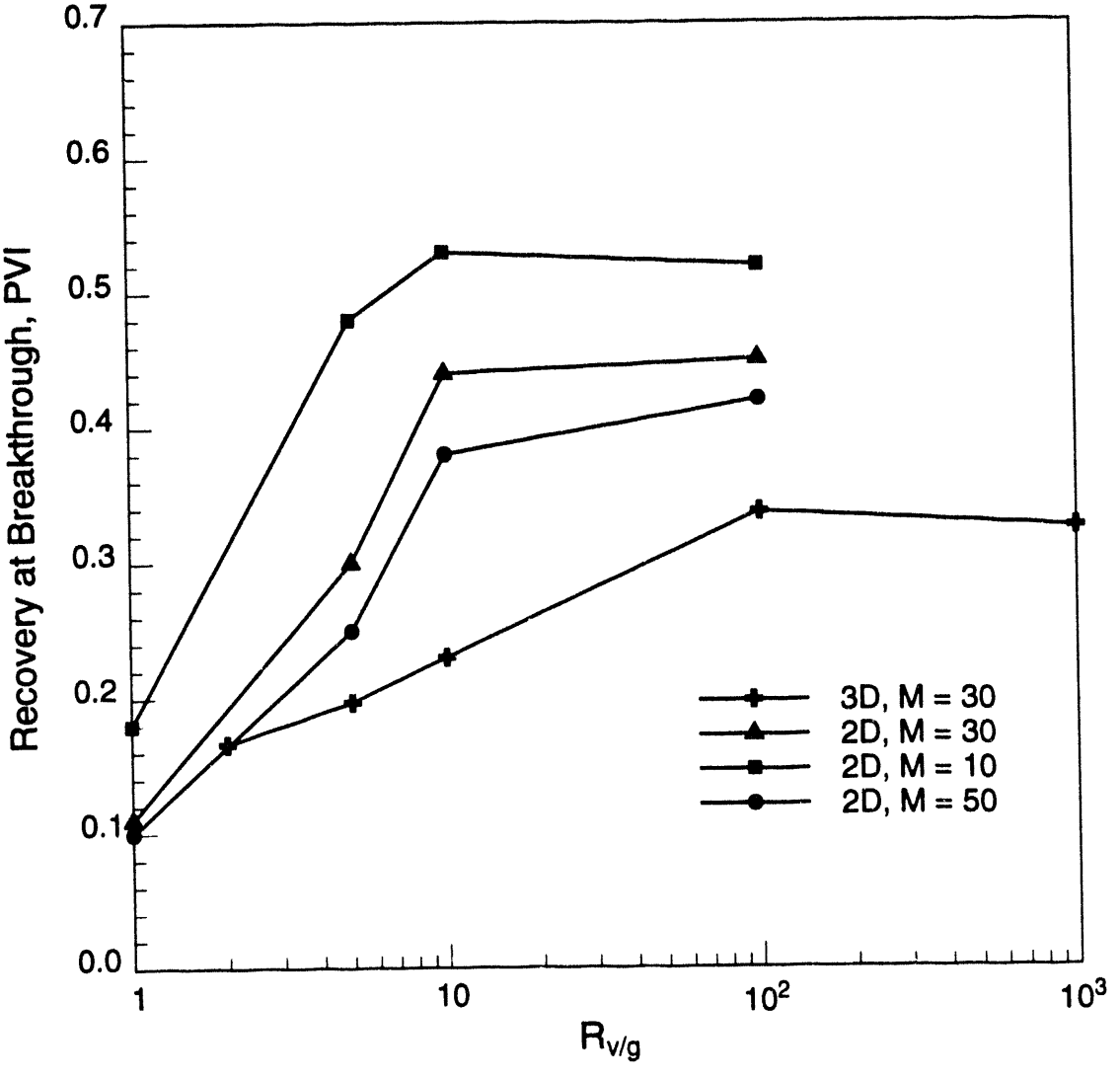

Figure 2.29: Effect of viscous to gravity ratio, $R_{v/g}$, on breakthrough recovery for 2D and 3D displacements when L/H = 4.

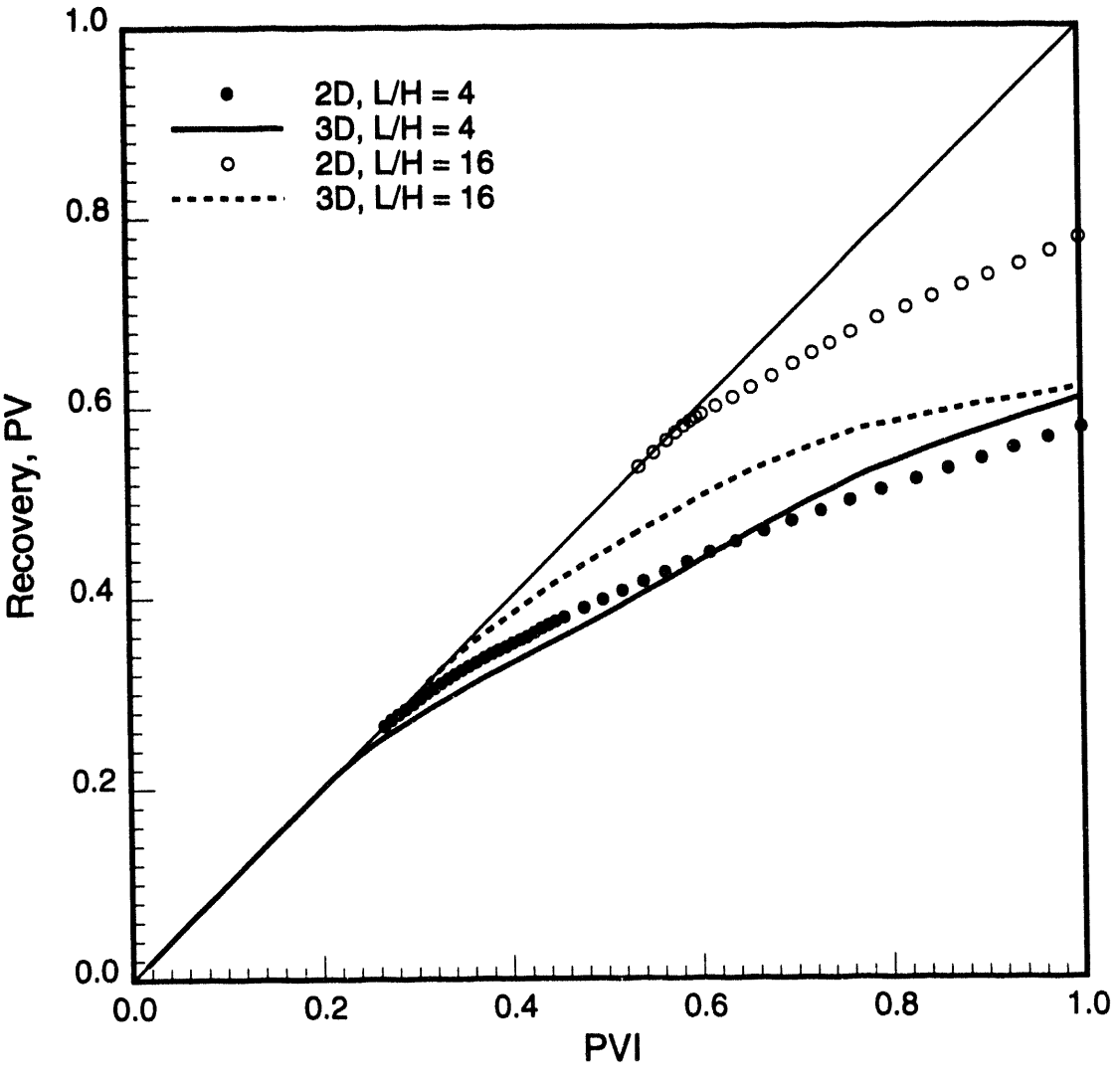

Figure 2.30: Comparison of calculated oil recovery for 2D and 3D simulations in homogeneous porous media for $R_{v/g} = 5$.

M = 30, Rvg = 100, PVI = 0.33

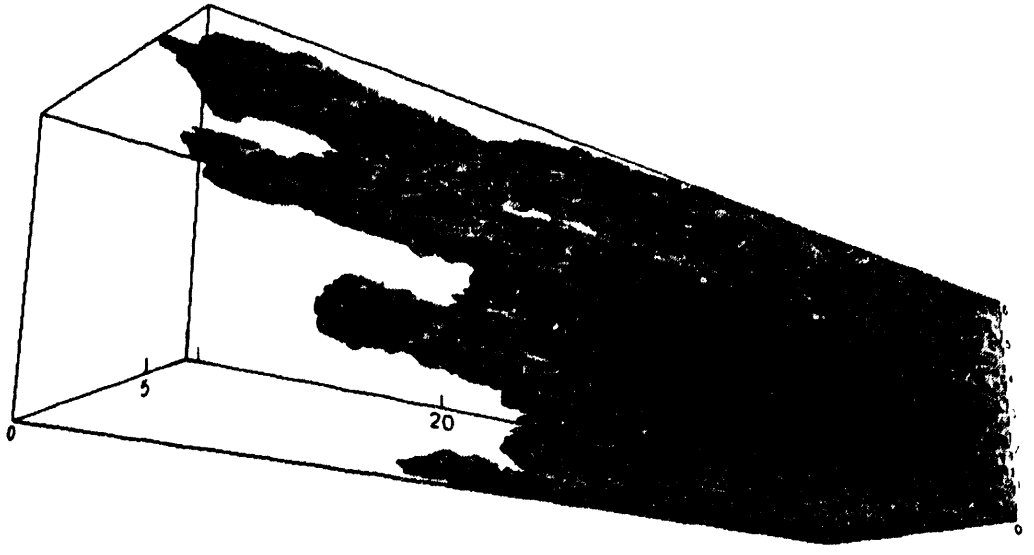

Figure 2.31: A 3D snapshot for M = 30, L/H = 4 and $R_{v/g}$ = 100 in a homogeneous porous medium at 0.33 PVI.

of injected fluid witin the fingers and downward flow of the resident, more viscous fluid between the fingers. In 2D flow, the vertical displacement must cause mixing of the two fluids because the flow can only occur in a single plane. That mixing reduces the local contrasts in viscosity and density, which limits the driving force for vertical transport.

In 3D flow, however, vertical flow need not take place in a single plane. Instead, downward flow of the heavy, more viscous fluid can take place between fingers. As a result, less mixing takes place, the viscosity and density contrasts remain higher than in 2D flow, and hence, segregation remains important at higher values of $R_{v/g}$. Thus, 2D calculations can yield inaccurate predictions when $R_{v/g}$ is in the transition region and L/H is large, as it is likely to be in field-scale flows.

2.2.3 Heterogeneous Porous Media

To investigate how the presence of permeability heterogeneities affects the interplay of gravity segregation and viscous fingering, a series of computations was performed for 2D and 3D correlated permeability distributions for Dykstra-Parsons coefficients V_{DP} = 0.2, 0.4, and 0.8 and dimensionless correlation lengths λ_D = 0.05, 0.1 and 0.2. Here we illustrate the results for V_{DP} = 0.8 and λ_D = 0.2. The permeability distributions were generated by Gaussian sequential simulation, and the 2D and 3D distributions were generated independently. Simulations were performed for mobility ratios of 10, 30, and 50.

When the permeability field was nearly uncorrelated (small λ_D), fingering behavior was nearly the same in 3D flow as that observed for 2D flow, and both were similar to the behavior described above for homogeneous porous media. Simulations with gravity were not performed for those fields, but we speculate that gravity would also have effects similar to those for homogeneous porous media.

When the correlation length is longer (λ_D = 0.2), the resulting permeability fields contain preferential flow paths that interact strongly with viscous forces to determine where injected fluid flows most easily. Fig. 2.32 shows transversely averaged concentration profiles for displacements with M = 1 and M = 10 in 2D and 3D porous media (labeled 2DF6 and 3DF6) with λ_D = 0.2 in all coordinate directions. Gravity effects are not included in the displacements of Fig. 2.32. The displacement at M = 1 shows how much spreading of the transition zone arises from the permeability distribution. Dispersion also contributes to that spreading, but its effect is small compared to that of the permeability distribution. Here again, the averaged profiles are similar for the 2D and 3D flows, though the 3D profiles are smoother, probably because they are averaged over more flow paths in 3D. When the displacement is unstable at M = 10, the transition zone is longer still, as viscous forces amplify the effects of the heterogeneity. When gravity effects are absent, the differences between 2D and 3D flow are small in this example in which the mean flow direction is parallel to one of the principal axes of the correlation structure. In simulations in which the mean flow direction was not so aligned, 2D simulations did not match the results of 3D simulations even when gravity effects were not included.

Fig. 2.33 gives another view of the effect of heterogeneity on the flow. Fig. 10a compares the averaged concentration profile for unstable (M = 30) 3D flow without gravity for permeability field 3DF6 with that for a homogeneous porous medium. The effect of the heterogeneity is to lengthen the transition zone substantially. In this case viscous fingers find and flow along the preferential flow paths present in field 3DF6 that are oriented more or less parallel to the mean flow direction. Fig. 10b shows the effect of gravity in the homogeneous displacement along with the profile for field 3DF6 without gravity. In the homogeneous porous medium, a significant gravity tongue forms, though it still does not lengthen the transition zone as much as heterogeneity alone in 3DF6.

The effect of gravity in field 3DF6 is shown in Fig. 10c, which gives profiles for $R_{v/g}$ = 0.1, 5, 10 and 20. At those values of $R_{v/g}$, a significant gravity tongue forms in a 3D homogeneous

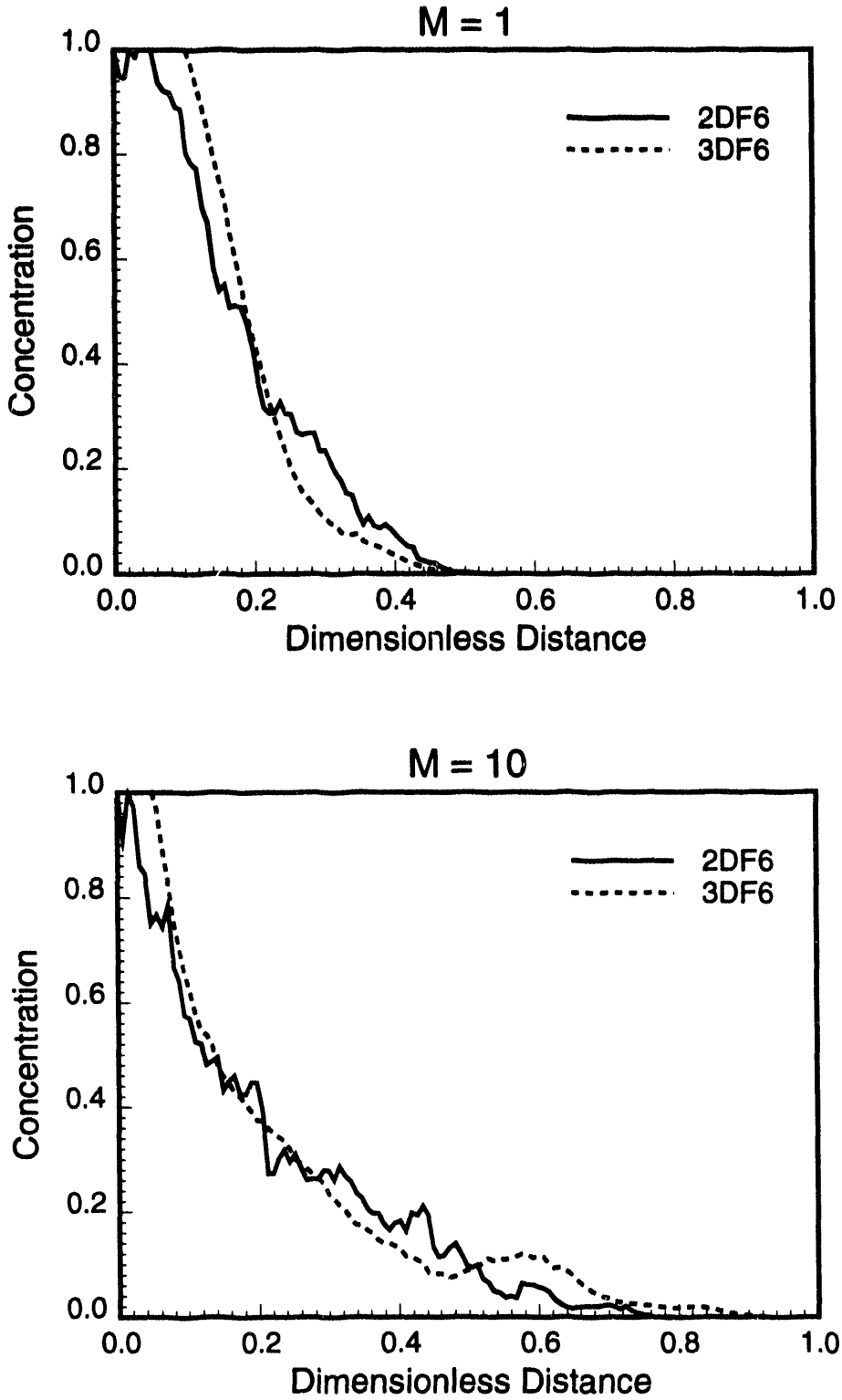

Figure 2.32: Comparison at 0.2 PVI of transversely averaged concentration profiles for M = 1 and M = 10 from simulations using 2DF6 and 3DF6 with no gravity segregation effects.

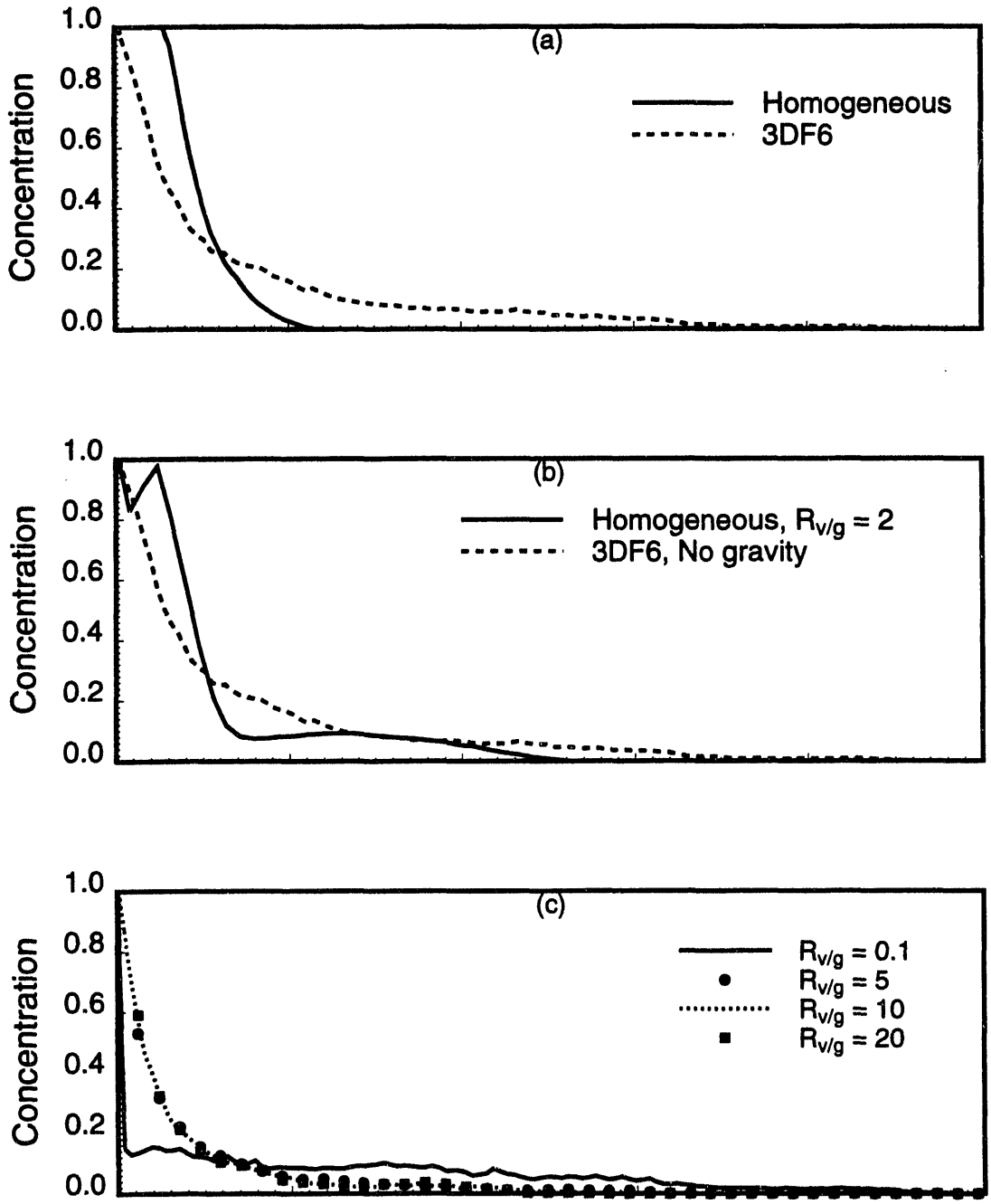

Figure 2.33: Comparison of transversely averaged concentration profiles for displacements for M = 30 in homogeneous and heterogeneous porous media with and without gravity effects. Figures (a) and (b) at 0.2 PVI and figure (c) at 0.1 PVI.

porous medium. In 3DF6, however, the profiles for $R_{v/g}$ = 5, 10, and 20 are indistinguishable. Figs. 2.34 and 2.35 are 3D snapshots at breakthrough for displacements in field 3DF6 at $R_{v/g}$ of 100 and 5 respectively. At $R_{v/g}$ = 100 (Fig. 2.34), two high-permeability channels join near the bottom of the model and the system breaks through along the bottom of the model. When $R_{v/g}$ is 5 (Fig. 2.35), some of the flow is reallocated to the top depriving the high permeability channels near the bottom from some of the flow. When $R_{v/g}$ = 5, breakthrough occurs near the top of the model. While the details of the flow are altered as $R_{v/g}$ is lowered from 100 to 5 in 3DF6, the average behavior in terms of sweep is not significantly affected. In Fig. 10c, only at the lowest value, $R_{v/g}$ = 0.1, is evidence of a significant gravity tongue apparent. Fig. 2.36 is a 3D snapshot of the M = 30 displacement in 3DF6 for $R_{v/g}$ = 0.1 at breakthrough. Thus, for field 3DF6, the gravity viscous transition occurs for values of $R_{v/g}$ between 0.1 and 5 for M = 30, in contrast to the behavior of a homogeneous porous medium, for which the transition occurs in the range $1 < R_{v/g} < 100$.

We argue that the difference in behavior between homogeneous and heterogeneous porous media is the result of restrictions to vertical flow in the heterogeneous medium. Evidently, the variations in permeability place some zones of low permeability in locations that slow gravity-driven vertical flow, while high permeability zones amplify the effects of viscous forces in the horizontal flow. As a result, the transition region occurs for lower values of $R_{v/g}$ when the heterogeneities of field 3DF6 are present. Here again, for displacements in the transition region, 2D simulations are unlikely to reproduce accurately the fluid distribution and recovery behavior of the 3D flow.

2.2.4 Discussion

The examples presented indicate that results of unstable displacements in 3D porous media can be very different from those obtained for 2D porous media when the combined effects of gravity segregation, heterogeneity, and viscous instability are considered. The differences are largest for systems with high values of L/H when the value of $R_{v/g}$ is in the transition region from gravity-dominated flow to viscous-dominated flow. If either gravity segregation or viscous forces dominate, however, 2D and 3D simulations produce similar results as long as the 2D permeability field represents adequately the correlated permeability structure of the 3D field. Thus, use of some 3D simulations to assess the relative importance of viscous and gravity forces is desirable, though it is clear that such computations will continue to be limited by the computation time required and by the availability and resolution of 3D reservoir descriptions. The particle-tracking technique used here is a relatively efficient technique that can be used to determine whether extensive 3D simulations are required, for example to investigate optimum injection rates, or whether 2D representations are adequate.

2.2.5 Conclusions

Comparison of 2D and 3D simulations of unstable displacements leads to the following conclusions:

Homogeneous Porous Media

1. If gravity effects are absent, 2D and 3D simulations predict similar finger dimensions and averaged concentration profiles.

2. 3D flow behavior differs substantially from 2D flow behavior for displacements in which neither gravity forces nor viscous forces dominate ($1 < R_{v/g} < 100$).

F6, M = 30, Rvg = 100, PVI = 0.105 (BT)

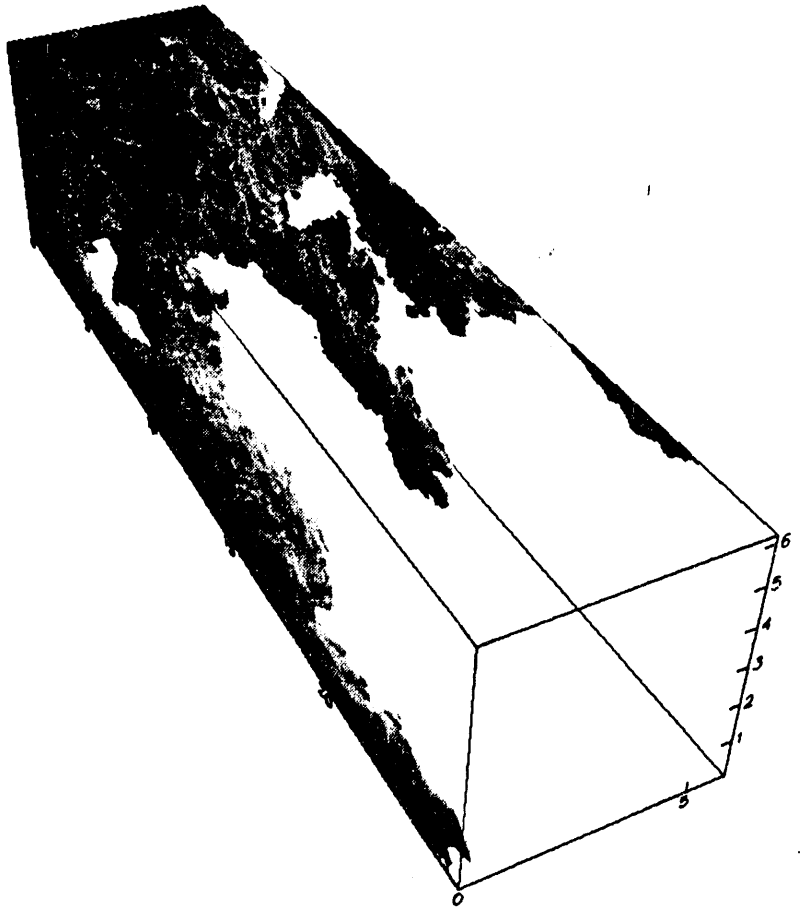

Figure 2.34: A 3D snapshot for M = 30 in permeability field 3DF6 with $R_{v/g} = 100$ at breakthrough (0.105 PVI).

F6, M = 30, Rvg = 5, PVI = 0.07 (BT)

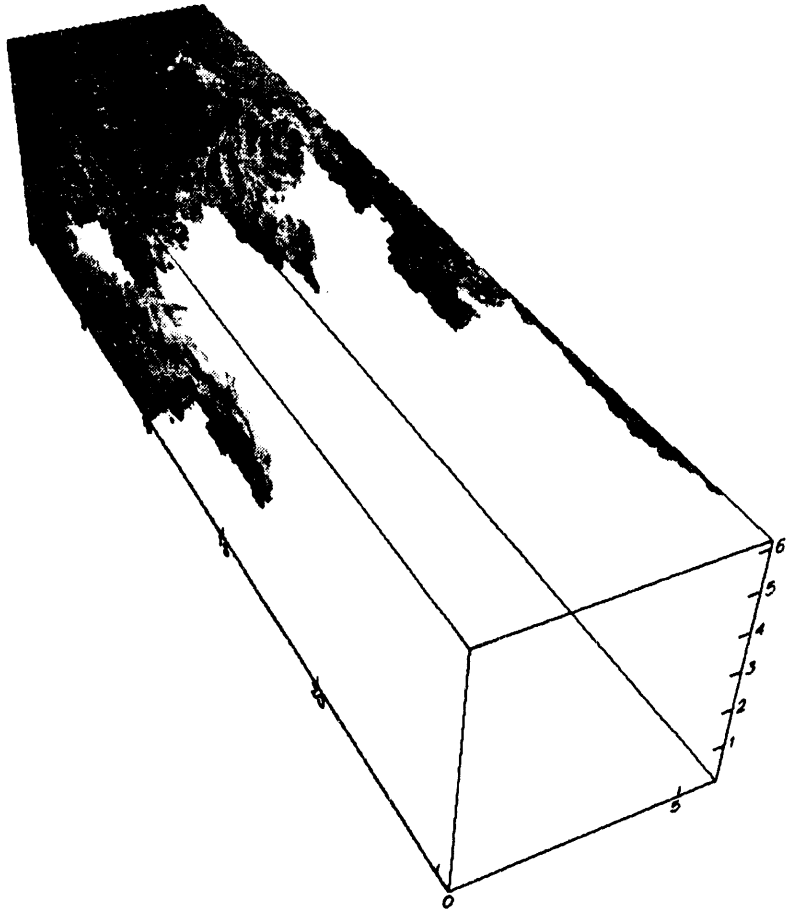

Figure 2.35: A 3D snapshot for M = 30 in permeability field 3DF6 with $R_{v/g} = 5$ at breakthrough (0.07 PVI).

F6, M = 30, Rvg = 0.1, PVI = 0.04 (BT)

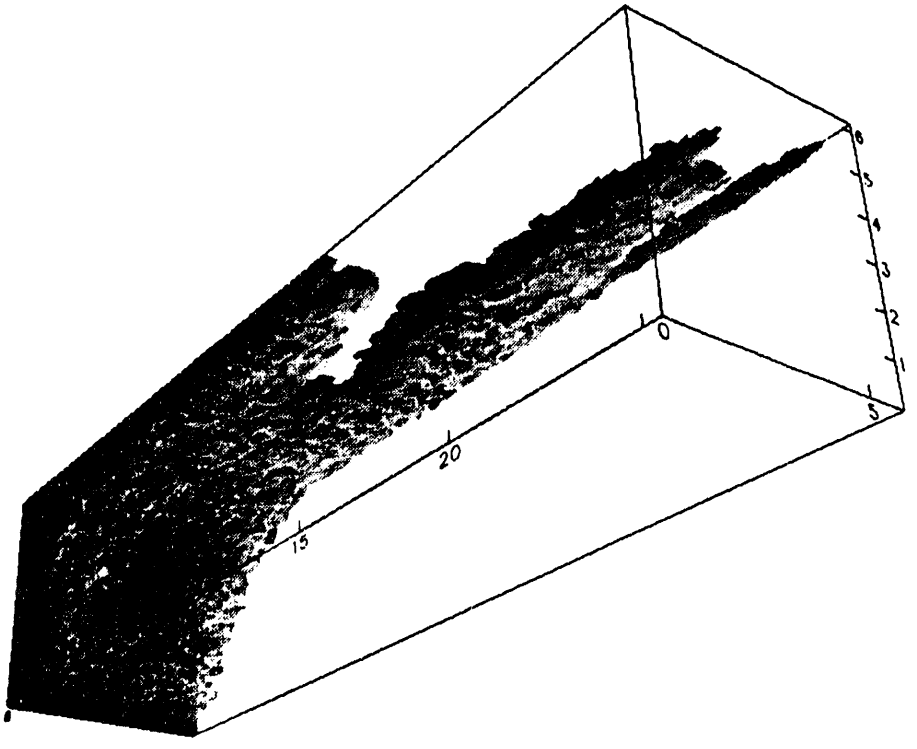

Figure 2.36: A 3D snapshot for M = 30 in permeability field 3DF6 with $R_{v/g} = 0.1$ at breakthrough (0.04 PVI).

Heterogeneous Porous Media

3. In correlated permeability fields in the absence of gravity, 2D and 3D simulations agree well as long as the principal axes of the correlation structure are aligned with the mean flow direction.

4. The presence of correlated heterogeneities can significantly alter the range $R_{v/g}$ over which the transition from gravity-dominated flow to flow controlled by viscous forces is observed.

3. Predicting Flow in Heterogeneous Systems Using Streamtubes

Marco R. Thiele and Martin Blunt

3.1 Introduction

Streamtubes have been used in the petroleum and groundwater literature to characterize flow patterns in two-dimensional domains. Some early work was done by Higgins and Leighton [30], Higgins *et al.* [31], and Martin and Wegner [42]. More recent attempts have been by Hewett and Behrens [29] and King *et al.* [38]. An excellent reference on streamtubes is Bear [6]. In general though, streamtubes have not been used as successfully in the petroleum literature as they have been in the field of groundwater modeling. Groundwater flows are generally single phase, and the velocity field does not change with time. Most petroleum engineering applications on the other hand, such as water and gas flooding, are multiphase displacements that see a significant change of the total velocity with time. Unlike groundwater applications then, the geometry of the streamtubes will change as the displacement takes place.

Overcoming this problem is the main focus of the work presented here. Streamtubes are appealing because they may be treated as quasi-one-dimensional, homogeneous systems. Many one-dimensional analytical solutions exist and streamtubes offer a natural way to map such solutions onto a two-dimensional, heterogeneous domain. Furthermore, analytical solutions are by definition exact and a mapping of this type would allow for a solution free of numerical diffusion.

By eliminating numerical diffusion and the problems associated with it, streamtubes offer a way to study the interaction of reservoir heterogeneity and the nonlinearities of various displacement processes. A further appealing feature of numerical modeling by streamtubes is the absence of any type of stability criterion. In traditional reservoir simulation, the time step used to solve the hyperbolic conservation equations must satisfy the Courant-Friedrichs-Lewy (CFL) condition which is given by $N_c \leq 1$ where $N_c = (v_{max}\Delta t/\Delta x)$. For highly nonlinear problems this may impose very small time steps and/or alternatively a very fine grid to obtain a solution at all, leading to prohibitively expensive numerical computations. By mapping analytical solutions for the conservation equations, the problem is completely side-stepped in the streamtube approach. A solution is always obtained. Rather, the question becomes how many times the streamtubes need to be updated in order to reach a converged solution.

First results indicate that two orders of magnitude fewer matrix inversions are needed compared to traditional finite difference simulators, allowing for a very rapid evaluation of the displacement efficiency.

3.2 The Mathematics of Streamtubes

A streamtube, by definition, is bounded by two streamlines. A streamline is a line everywhere tangent to the velocity vector at a given instant. In parametric form, a streamline can be written as

$$x = x(s)\,; \quad y = y(s)\ . \tag{3.1}$$

By definition

$$\frac{dy/ds}{dx/ds} = \frac{u_y}{u_x}\ , \tag{3.2}$$

which can be rewritten as

$$u_y \frac{dx}{ds} - u_x \frac{dy}{ds} = 0 \ . \tag{3.3}$$

Consider now a function Ψ, called the streamfunction, that is constant along a streamline. Then it is true that

$$d\Psi = \frac{\partial \Psi}{\partial x}\frac{dx}{ds} + \frac{\partial \Psi}{\partial y}\frac{dy}{ds} = 0 \ , \tag{3.4}$$

and by equating terms with Eq. 3.3 we get that

$$\frac{\partial \Psi}{\partial x} = u_y \ \ ; \ \ \frac{\partial \Psi}{\partial y} = -u_x \ . \tag{3.5}$$

Substituting for Darcy's law for phase velocities u_x and u_y gives

$$\frac{\partial \Psi}{\partial x} = -\lambda_y \frac{\partial P}{\partial y} \ \ ; \ \ \frac{\partial \Psi}{\partial y} = \lambda_x \frac{\partial P}{\partial x} \ , \tag{3.6}$$

where λ_x and λ_y are the total mobilities in the x and y direction and given by

$$\lambda_x = \sum_{j=1}^{N_p} \frac{k_x k_{rj}}{\mu_j} \ \ ; \ \ \lambda_y = \sum_{j=1}^{N_p} \frac{k_y k_{rj}}{\mu_j} \ , \tag{3.7}$$

where j is the phase index, and N_p is the total number of phases present. Solving for the pressure gradients from Darcy's law gives

$$\frac{\partial P}{\partial y} = -\frac{1}{\lambda_y}\frac{\partial \Psi}{\partial x} \ \ ; \ \ \frac{\partial P}{\partial x} = \frac{1}{\lambda_x}\frac{\partial \Psi}{\partial y} \ . \tag{3.8}$$

Pressure must be single valued everywhere in the domain. Therefore, the mixed partials must be equal giving the relation

$$\frac{\partial}{\partial x}\left(\frac{\partial P}{\partial y}\right) = \frac{\partial}{\partial y}\left(\frac{\partial P}{\partial x}\right) \ . \tag{3.9}$$

Substituting for the pressure gradients gives

$$\frac{\partial}{\partial x}\left(-\frac{1}{\lambda_y}\frac{\partial \Psi}{\partial x}\right) = \frac{\partial}{\partial y}\left(\frac{1}{\lambda_x}\frac{\partial \Psi}{\partial y}\right) \ , \tag{3.10}$$

and rearranging finally returns the governing equation for the streamfunction Ψ as

$$\frac{\partial}{\partial x}\left(\frac{1}{\lambda_y}\frac{\partial \Psi}{\partial x}\right) + \frac{\partial}{\partial y}\left(\frac{1}{\lambda_x}\frac{\partial \Psi}{\partial y}\right) = 0 \ . \tag{3.11}$$

3.3 The Linear Problem

3.3.1 M=1 Displacements With No Physical Diffusion

For unit mobility displacements the streamtube method is exact, because λ_x and λ_y are constant in time and the streamtube geometry is fixed. The problem formulation then becomes

$$\frac{\partial}{\partial x}\left(\frac{1}{\lambda_y}\frac{\partial \Psi}{\partial x}\right) + \frac{\partial}{\partial y}\left(\frac{1}{\lambda_x}\frac{\partial \Psi}{\partial y}\right) = 0$$

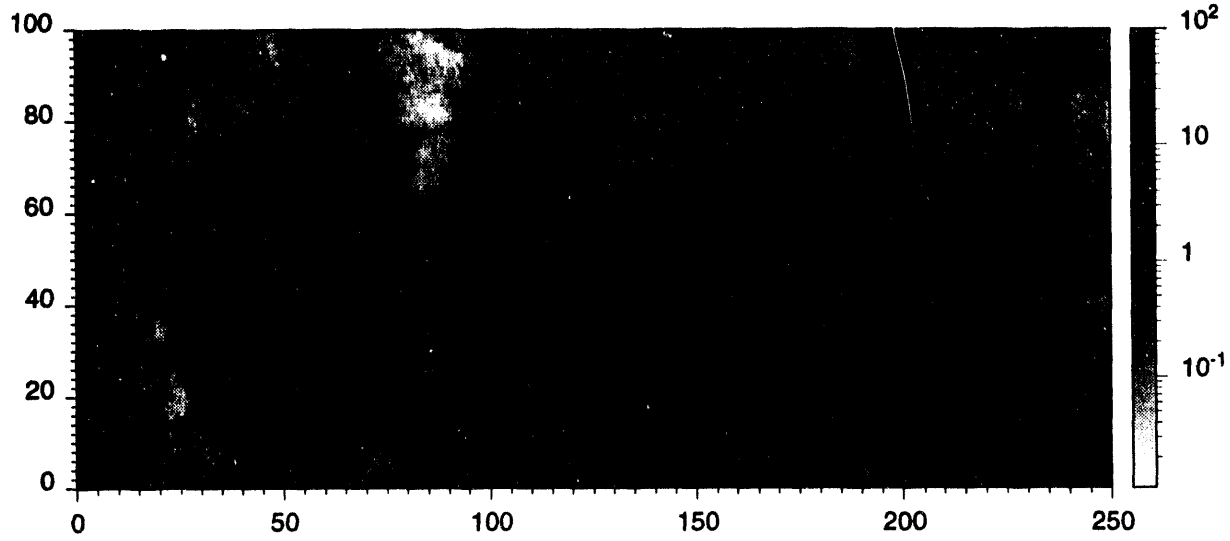

Figure 3.1: Permeability map with logarithmic scaling - (250x100 Grid).

with the following boundary conditions for $0 \leq x \leq 1$, $0 \leq y \leq 1$

$$\Psi(x, y = 0) = 0 \tag{3.12}$$
$$\Psi(x, y = 1) = Q_{tot} \tag{3.13}$$
$$\Psi_x(x = 1, y) = 0 \tag{3.14}$$
$$\Psi(x = 0, y) = yQ_{tot} \tag{3.15}$$

Consider the permeability map shown in Fig. 3.1. Solving for the streamfunction using Eq. 3.11 and the appropriate boundary conditions returns a map of streamlines shown in Fig. 3.2. To find the displacement profile for a unit mobility ratio, the one-dimensional analytical solution must simply be mapped onto each streamtube.

The one-dimensional M=1 analytical solution is, of course, a piston-like front as shown in Fig. 3.3. Mapping the solution onto a streamtube simply involves "filling-in" each tube up to the desired time t_D. An example is shown in Fig. 3.4. By mapping the solution at different times, a history of displacement is easily put together as shown in Fig. 3.5. Several key ideas are present in these plots:

Numerical Diffusion. The solution is free of any numerical diffusion, because the hyperbolic conservation equation is solved for analytically and then mapped onto each tube directly. Some smearing is introduced when the sharp interface of the analytical solution falls on a gridblock or when two (or more) streamtubes, one of which is "full" and the other "empty" cut across a gridblock. In either case the smeared front can never be larger than the width of a single gridblock. Contrary to traditional finite difference simulation, this type of diffusion does not grow with time since it is solely an artifact of the mapping algorithm and independent from the underlying equations describing the physics of flow.

Fig. 3.6 compares the solution obtained using streamtubes with solutions obtained from two finite difference simulators, MISTRESS and ECLIPSE. MISTRESS is a research code written by BP Research and features a flux corrected transport (FCT) formulation Christie and Bond [14], while ECLIPSE is a commercially available code with standard one point upstream

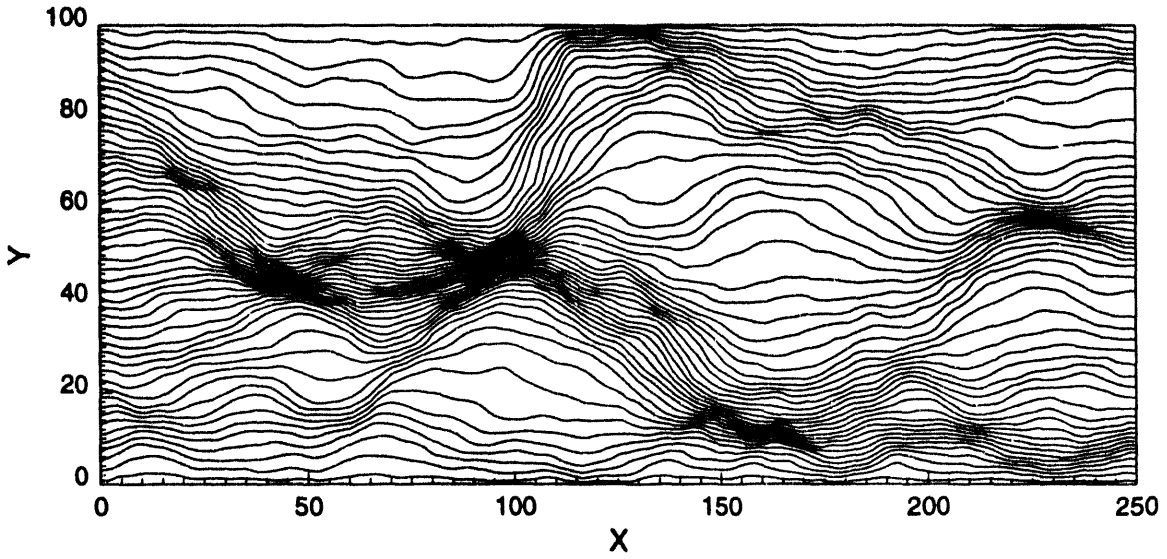

Figure 3.2: Streamlines for permeability map shown in Fig. 5.15.

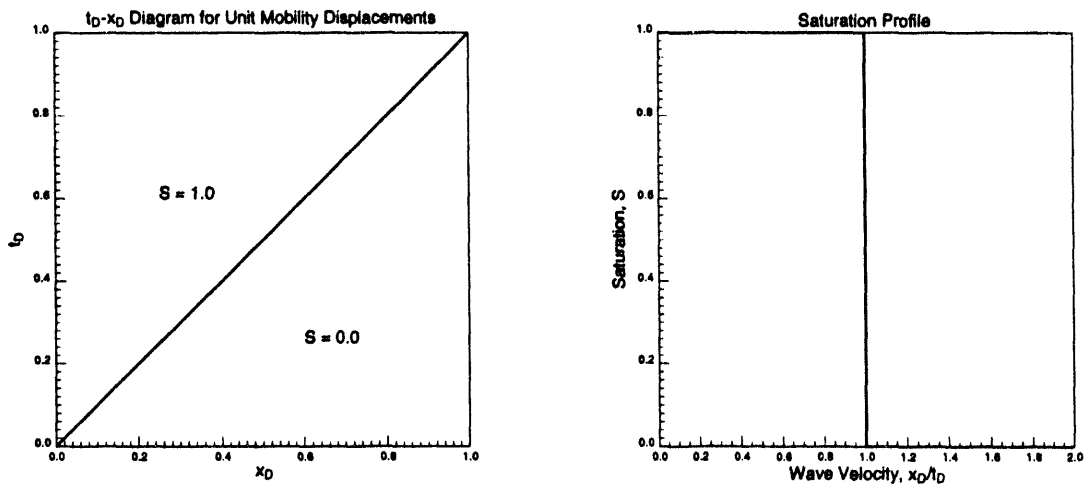

Figure 3.3: One-dimensional analytical solution for a unit mobility displacement.

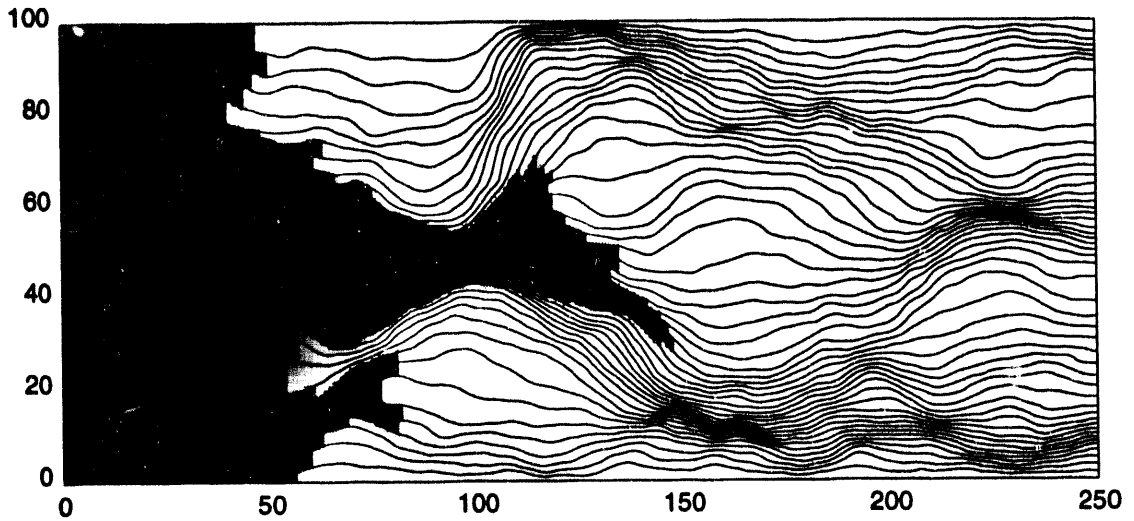

Figure 3.4: Mapping analytical solution at $t_D = 0.3$ onto 50 streamtubes generated by the permeability map shown in Fig. 3.1.

weighting. The profile obtained using streamtubes clearly establishes what the limiting, diffusion-free solution to the heterogeneity field in Fig. 3.1 should look like.

Time Stepping. The streamtube solution does not involve any time stepping for mapping a solution at a particular time t_D. The reason for this is that the one-dimensional analytical solution allows solving for the saturation/concentration profile for a given dimensionless time t_D immediately. This profile is then mapped onto each tube giving the two-dimensional solution to the heterogeneous field at that desired time. Standard finite difference simulators, on the other hand, must solve the concentration equation repeatedly for a specified time step Δt until the desired time is reached. Although this is an explicit calculation and therefore fairly fast, it still adds to some overhead and, of course, is the reason for numerical diffusion.

Heterogeneity-Dominated Flow. The underlying assumption in using streamtubes is that the flow is dominated by the large-scale heterogeneities of the system creating channels of preferential flow. These flow paths are identified and mapped out by the tubes.

No Crossflow. A streamline is a no-flow boundary. Therefore, any orthogonal flow to the main direction of flow in a tube cannot be considered by this type of model. Examples of such orthogonal flow are physical diffusion and capillary crossflow.

3.3.2 M=1 Displacements With Physical Diffusion

Much work in petroleum research has gone into describing subgrid heterogeneities by introducing an effective diffusivity that smears the piston-like front in Fig. 3.3. For a recent treatment on the subject the reader is referred to Wattenbarger [69]. A more realistic unit mobility displacement may therefore be one modeled by the well known convection-diffusion equation given by

$$\frac{\partial C}{\partial t_D} + \frac{\partial C}{\partial x_D} = \frac{1}{N_{Pe}} \frac{\partial^2 C}{\partial x_D^2} \tag{3.16}$$

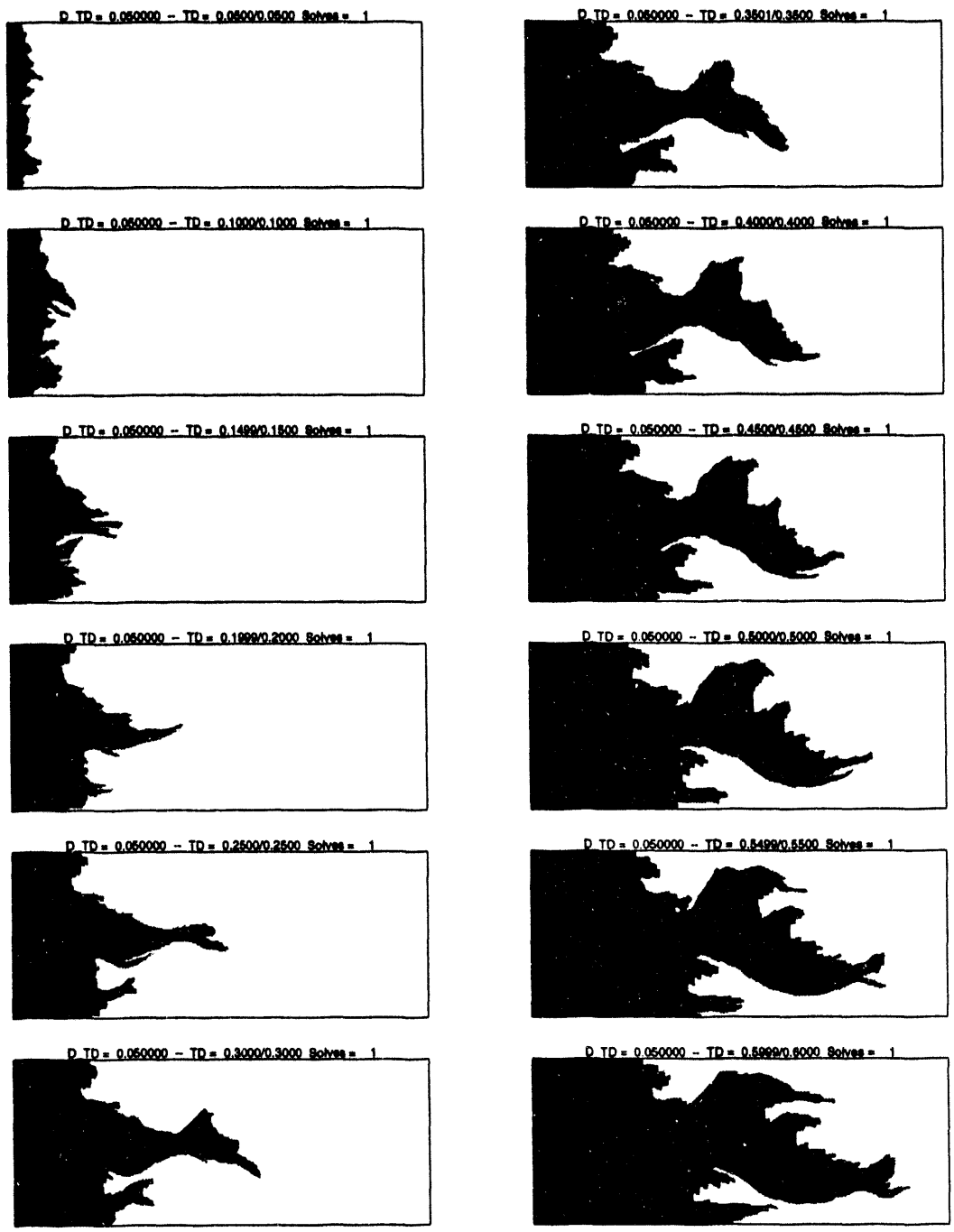

Figure 3.5: Displacement history at $\Delta t_D = 0.05$ intervals for the permeability map shown in Fig. 3.1.

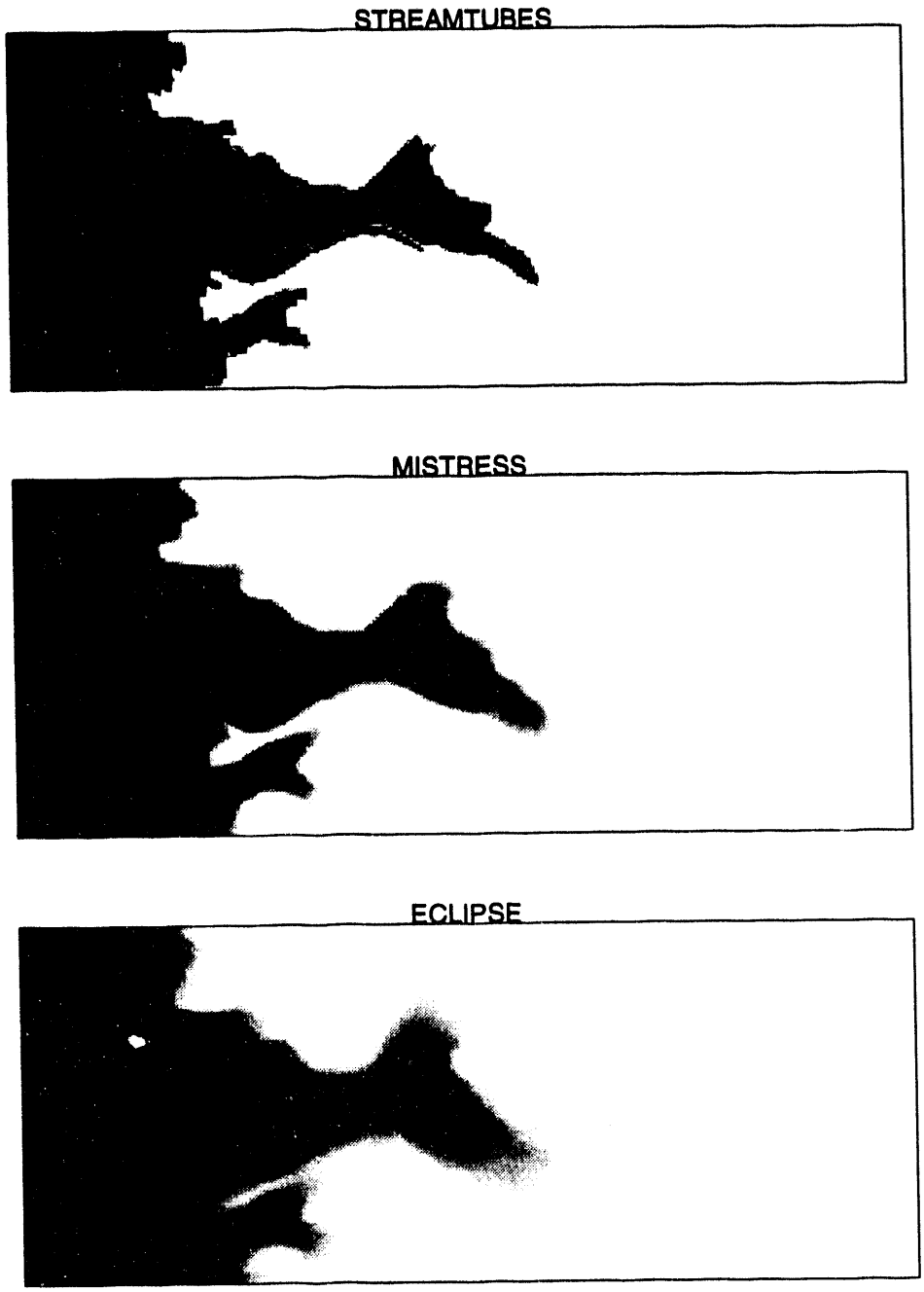

Figure 3.6: Comparison of saturation profiles showing extent of numerical diffusion in finite difference simulators. Streamtube method vs. MISTRESS, a BP research code with flux corrected transport (FCT) (CFL = 0.2) and ECLIPSE, a commercially available reservoir simulator with single point upstream weighting and automatic time step selection.

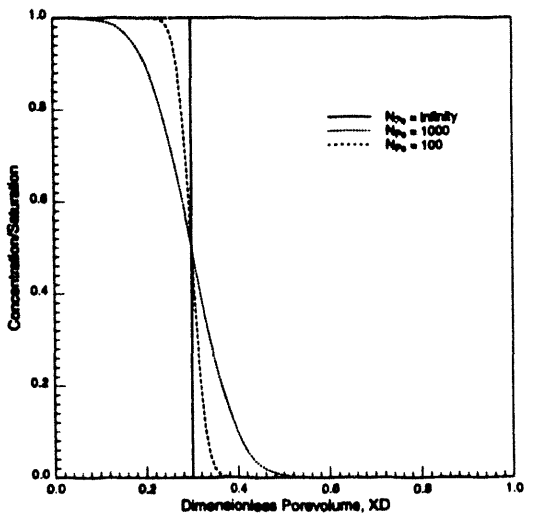

Figure 3.7: One-dimensional analytical solutions for the convection-diffusion equation at $t_D = 0.3$ and three values of N_{Pe}.

where N_{Pe} is the Peclet number given by

$$N_{Pe} = \frac{L}{\alpha} \tag{3.17}$$

and α is the dispersivity of the permeable medium. An approximate solution [39], using the following initial and boundary conditions,

$$C(x_D, t_D = 0) = 0 \tag{3.18}$$

$$C(x_D = 0, t_D) = 1 \tag{3.19}$$

$$C(x_D \to \infty, t_D) = 0 \tag{3.20}$$

is given by

$$C(x_D, t_D) = \frac{1}{2}\text{erfc}\left(\frac{x_D - t_D}{2\sqrt{\frac{N_{Pe}}{t_D}}}\right). \tag{3.21}$$

Adding physical diffusion along a streamtube amounts to mapping Eq. 3.21 onto each streamtube for a given value of N_{Pe} and t_D. Examples of analytical solutions at $t_D = 0.3$ for $N_{Pe} \to \infty$, $N_{Pe} = 1000$, and $N_{Pe} = 100$ are shown in Fig. 3.7 which, when mapped onto the streamtubes for the heterogeneous permeability field, give rise to the concentration profiles shown in Fig. 3.8. By comparing Figs. 3.6 and 3.8, it becomes apparent that the numerical diffusion created by the finite difference scheme is not equivalent to physical diffusion added along each streamtube. Numerical diffusion arises because of differencing and therefore will always have an x and y component and is not necessarily proportional to the magnitude of the flow velocity. This type of numerical diffusion is therefore not to be mistaken with longitudinal or transverse physical diffusion which is respectively aligned and orthogonal to the main direction of flow and proportional to its magnitude. As in diffusion-free case, the solutions shown in Fig. 3.8 are to be interpreted as exact, limiting solutions for a unit mobility displacement with physical longitudinal diffusion. In most cases longitudinal dispersion is taken to be an order of magnitude or more larger than transverse diffusion. Thus, the streamtube method allows to captures the dominant physics of flow for these type of displacements.

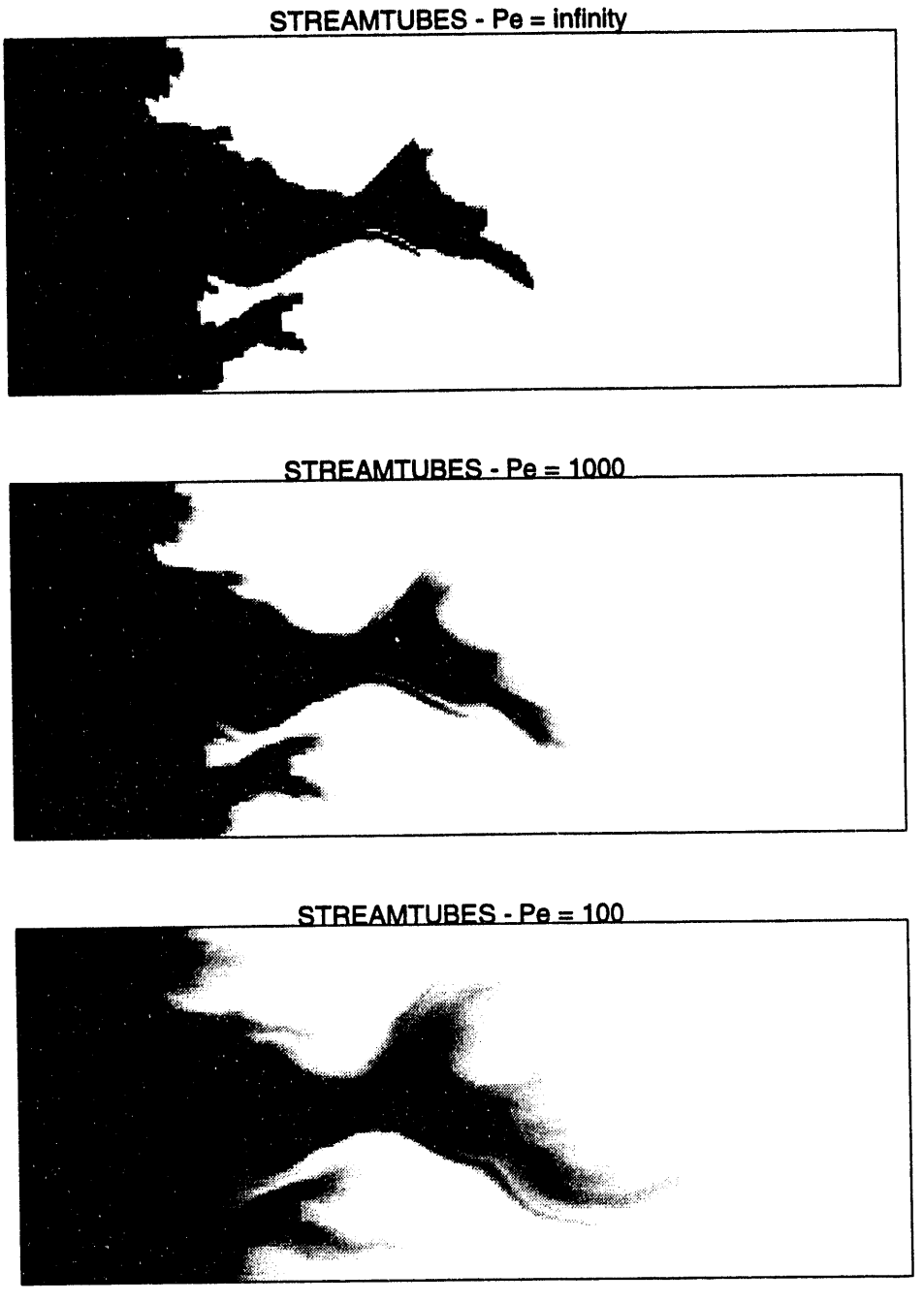

Figure 3.8: Including physical diffusion in M=1 displacement by mapping the convection-diffusion equation along each streamtube. Examples at $N_{Pe} \to \infty$, $N_{Pe} = 1000$, and $N_{Pe} = 100$

.

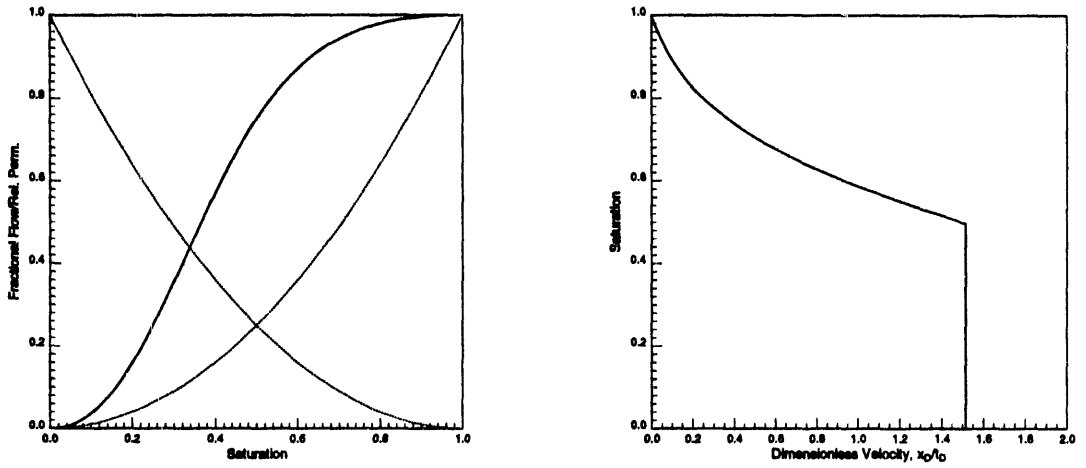

Figure 3.9: Buckley-Leverett analytical solution for a fractional flow function having quadratic relative permeability curves ($k_rw = S_w^2$, $k_ro = (1 - S_w)^2$) and a viscosity ratio of 3 ($\mu_o = 3$, $\mu_w = 1$).

3.4 The Nonlinear Problem (Buckley-Leverett)

The one dimensional conservation equation describing the flow of two immiscible, incompressible phases (oil and water) is well documented in the petroleum literature and given by Buckley and Leverett [11], Dake [17], and Lake [39]

$$\frac{\partial S_w}{\partial t_D} + \frac{\partial f_w}{\partial x_D} = 0 \tag{3.22}$$

where S_w is the water saturation, f_w is the fractional flow function, and t_D and x_D are dimensionless time and distance respectively. Eq. 3.22 is a quasi-linear hyperbolic partial differential equation which is solved using the following initial and boundary conditions

$$\begin{aligned} S_w(x_D,0) &= S_{wI} \;\; ; \;\; x_D \geq 0 \\ S_w(0,t_D) &= S_{wJ} \;\; ; \;\; t_D \geq 0 \end{aligned} \tag{3.23}$$

Eq. 3.22 is usually solved by the method of characteristics and depending on the shape of the fractional flow function f_w, the solution $S_w(x_D,t_D)$ may involve a spreading, a sharpening, or a mixed wave. For a good review on this subject the reader is referred to Johns [34]. Fig. 3.9 shows an example solution for a fractional flow having a mixed character. In a waterflood, the phase mobilities are a function of saturation, and thus implicitly of x and y. The total mobilities λ_x and λ_y are no longer constant in time and the streamlines are now a function of the mobility field and change as the displacement takes place. In other words, every saturation distribution will give rise to its own Ψ-field. To map the analytical solution shown in Fig. 3.9, the following simple algorithm is proposed.

1. Given some initial fluid mobility distribution, solve for the streamfunction Ψ.
2. Map the analytical solution onto the streamtubes by integrating from 0 to t_D (i.e., map the solution of Eq. 3.22 subject to the initial and boundary conditions given by Eq. 3.23).
3. Given this new mobility distribution recalculate for the streamfunction Ψ.

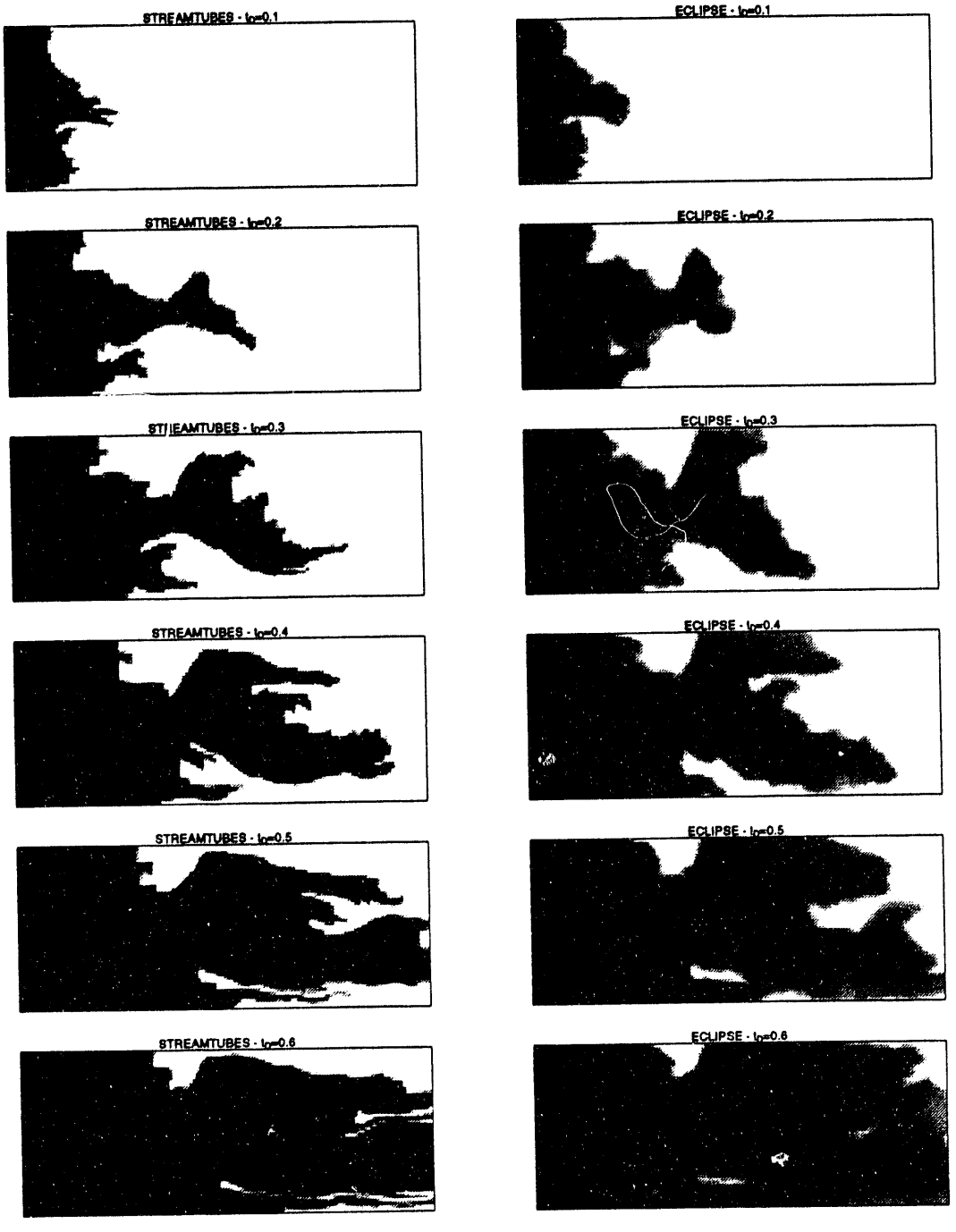

Figure 3.10: Comparison of displacement profiles at $\Delta t_D = 0.1$ generated by A) mapping the Buckely-Leverett solution shown in Fig. 3.9 along streamtubes and B) using ECLIPSE.

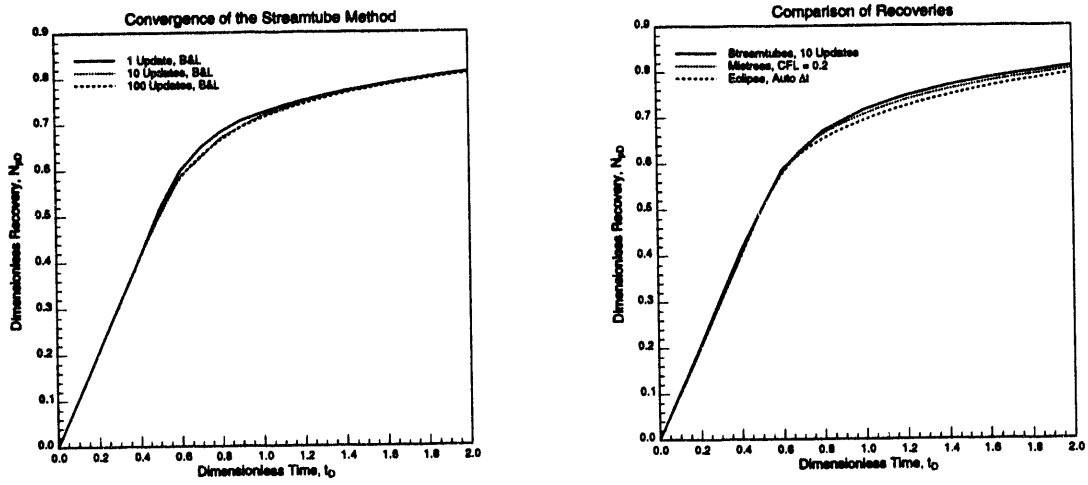

Figure 3.11: Recovery curves for different number of updates of the streamtubes to capture the nonlinearity of the Buckley-Leverett problem and comparison of recovery curves with those obtained using MISTRESS and ECLIPSE.

4. Repeat step 2 by integrating from 0 to $t_D + \Delta t_D$.

The reason for step 4 lies in the nature of the analytical solution. The Buckley-Leverett solution is known for the initial and boundary conditions given in Eq. 3.23. Because there is a discontinuity at $x_D = t_D = 0$, these conditions are commonly referred to as Riemann conditions, and we refer to the analytical solution as a Riemann solution.The real implication is that the analytical solution is known only for uniform initial and boundary conditions. Solving step 4 as a mapping from t_D to $t_D + \Delta t_D$ would contradict this by implying nonuniform initial conditions. Thus the only known analytical solution is, in fact, one from 0 to $t_D + \Delta t_D$.

To map out a history of the displacement then, the streamtubes are periodically recalculated and the Buckley-Leverett solution is mapped onto the new tubes as a true Riemann solution. An example of a waterflood using the permeability map of Fig. 3.1 is shown in Fig. 3.10 which also shows profiles computed using ECLIPSE. The streamtube method clearly agrees well with the finite difference simulation.

One question raised by solving nonlinear problems using streamtubes is the number of times the streamtubes need to be updated in order to capture the changing flow field correctly. It is always possible, of course, to solve for the streamtubes only once and map the Buckley-Leverett solution at several dimensionless times t_D to get a displacement history and a recovery curve. That approach would overestimate recovery, because the flow field would not be allowed to adjust to the changing mobility distribution. How many times then, must the Ψ be solved for to converge onto a solution? Fig. 3.11 suggests an answer to that question. Fig. 3.11 also shows how the streamtube method compares to recoveries obtained using MISTRESS and ECLIPSE. Mapping the analytical solution onto a streamtube map updated ten times is sufficient to match the responses obtained from MISTRESS and ECLIPSE. This is a very encouraging result since it compares extremely well with hundred of updates needed to calculate recoveries from these finite difference simulators.

A word of caution should be voiced at this point. It is important to understand that the converged solution obtained by updating the streamtubes and mapping a one-dimensional Riemann solution along each tube is an approximation of the real solution, which, of course, is not known. The work presented here suggests that this approximation is very good. The results summarized in Fig. 3.11 are in fact quite startling because they suggest that ten updates using streamtubes

gives almost the exact same response as a hundred updates. In other words, the streamtubes are a very weak function of the changing mobility field and a converged solution is obtained after only ten updates. The reason may be due to the fact that although the end-point mobility ratio for the displacement is $M = 3$, the frontal mobility ratio is only $M_{frt} \approx 0.75$. Similar behavior is observed.

3.5 Concluding Remarks

By treating streamtubes as quasi one-dimensional systems it is possible to map analytical solutions onto two-dimensional heterogeneous domains. The resulting solution is free of numerical diffusion and has no stability constraint.

For linear problems in which the velocity field remains constant with time, the streamtube method is equivalent to finite difference methods but offers solutions completely devoid of numerical diffusion. Furthermore, because the solution along a streamtube is analytical no time-stepping is involved to find the concentration/saturation profile at any given time.

Physical diffusion may be added in the longitudinal direction by mapping the convection-diffusion equation for a given Peclet number along a streamtube. Transverse diffusion and capillary crossflow though, are not included since streamtubes are by definition one-dimensional.

For nonlinear problems the changing mobility field now forces the streamtube geometries to become a function of time. Furthermore, in order to map the analytical solution onto the changing tubes requires that the solution be mapped as Riemann problems. For the Buckley-Leverett problem investigated here, the streamtube geometries are only a very weak function of time requiring only ten updates to estimate recovery correctly, a substantial improvement to many hundreds of times the pressure field is solved for in regular finite difference simulators.

Thus, streamtubes offer an efficient way to estimate the displacement efficiency on a particular heterogeneous domain of interest. The speed of the calculation therefore offers a unique opportunity to investigate different geostatistical realizations of the same domain and obtain a distribution of recovery responses.

4. Experimental Verification of MOC Theory

Roderick P. Batycky

Analytical solutions to model multicomponent, two-phase flow, based on the Method of Characteristics (MOC) have been developed by several authors [45, 48, 19, 35, 34]. This solution method was applied to four-component systems with the conclusion that miscibility can develop in a way not previously identified. Specifically, in condensing/vaporizing (C/V) systems the tie-line controlling miscibility is the "crossover" tie line, and not the injection or initial tie line [35].

This chapter deals with testing the analytical theory through experiments with water/alcohol/iso-octane systems. The flow tests are conducted in a glass bead packed medium under conditions where the MOC theory will apply (dispersion free, stable flow, no capillary pressure). The purpose is to validate the analytical description of the C/V process and the existence of a crossover tie line.

The current work involves experiments with a three-component system, testing experimental procedures to measure the data, and construction and subsequent comparison with analytical solutions. As discussed above, the real test of the theory will come with the four-component system, but since little is known of the fractional flow characteristics of water/alcohol/iso-octane, current experiments have been aimed at the three-component system. The idea then is to apply this knowledge to the four-component system.

4.1 Experimental Design and Procedures

4.1.1 Fluid System

The three-component system used in these experiments includes, pure water, iso-propyl alcohol (IPA), and iso-octane (i-C_8) (Fig.4.1). Tie lines and the shape of the two-phase region were determined by analyzing equilibrium samples at room temperature and pressure by gas chromatography (GC).

Note that component mass fractions are shown rather than volume fractions (concentrations). Mass fractions are used because they are measured directly for the displacement processes, so that material balance calculations can be performed without correction for volume change on mixing. The loss of any mass in closing a material balance on each component will indicate experimental errors.

The only component properties measured were the pure component densities. Values obtained are shown in Table 4.1. Viscosities and interfacial tensions for this phase diagram were taken from references [47] and [54]. For water-rich phases, viscosities range from 1 cp pure water, up to about 3 cp for 40% H_2O / 60% IPA. I-C_8-rich phase viscosities range from 0.48 cp to 0.51 cp. Interfacial tensions range from 38 mN/m at the base of the diagram to 0.5 mN/m near the plait point. To summarize, the wetting phase (H_2O-rich) is more viscous and more dense than the nonwetting phase (i-C_8-rich). The phase diagram in Fig.4.1 was used for all three-component experiments.

The four-component system studied included the addition of n-propanol (NPA) to the original system. The addition of NPA to i-C_8 and water produces a ternary phase diagram similar to that shown in Fig.4.1. The phase viscosities and IFT's between each phase were assumed to be the same as the IPA system, given the similarity of IPA and NPA.

Table 4.1: Pure Component Densities

Component	Density (g/cm^3)
Water	0.996
IPA	0.777
I-C8	0.673

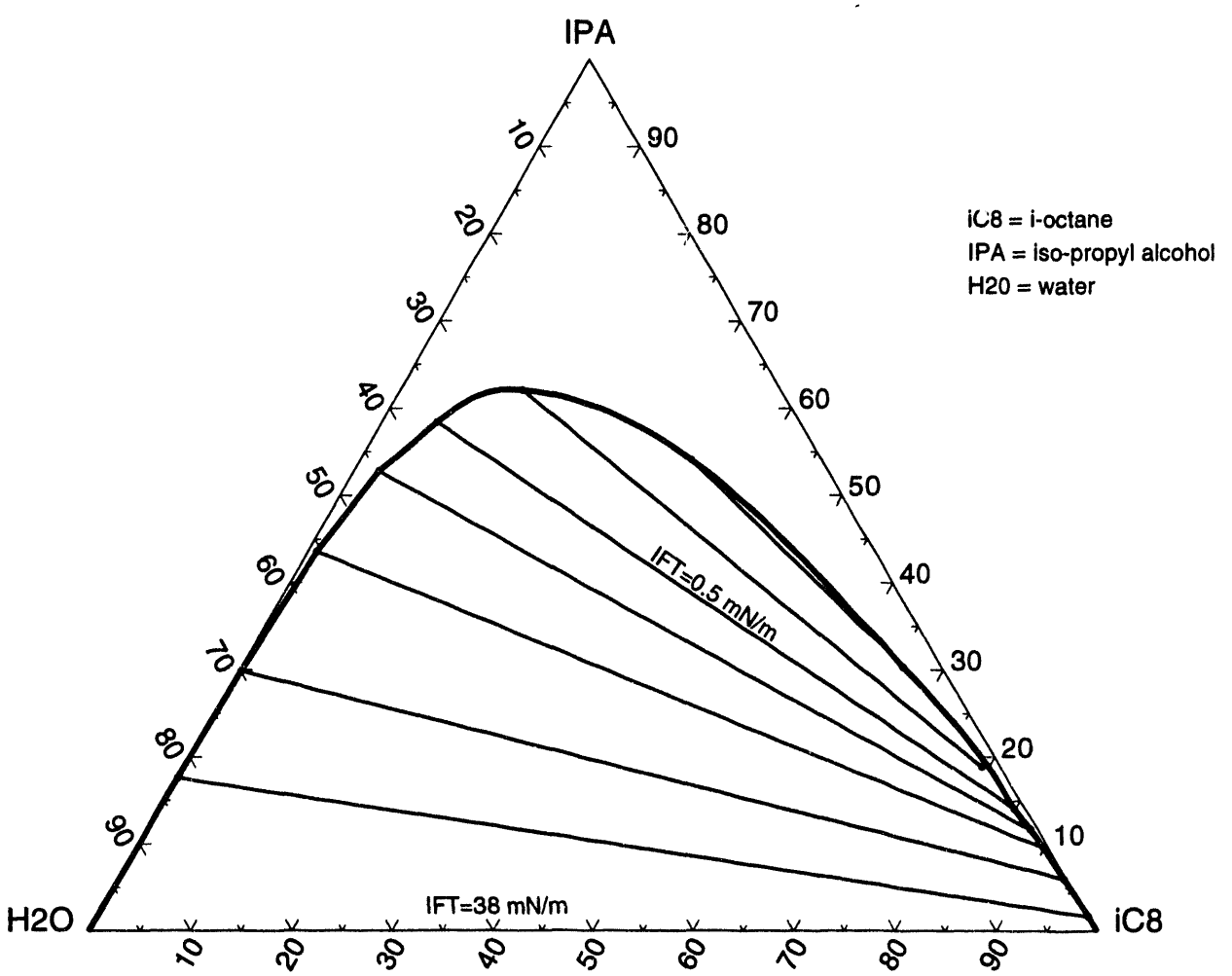

Figure 4.1: Water/IPA/I-C8 Phase diagram for Water/IPA/I-C_8 mixtures, (in mass fractions).

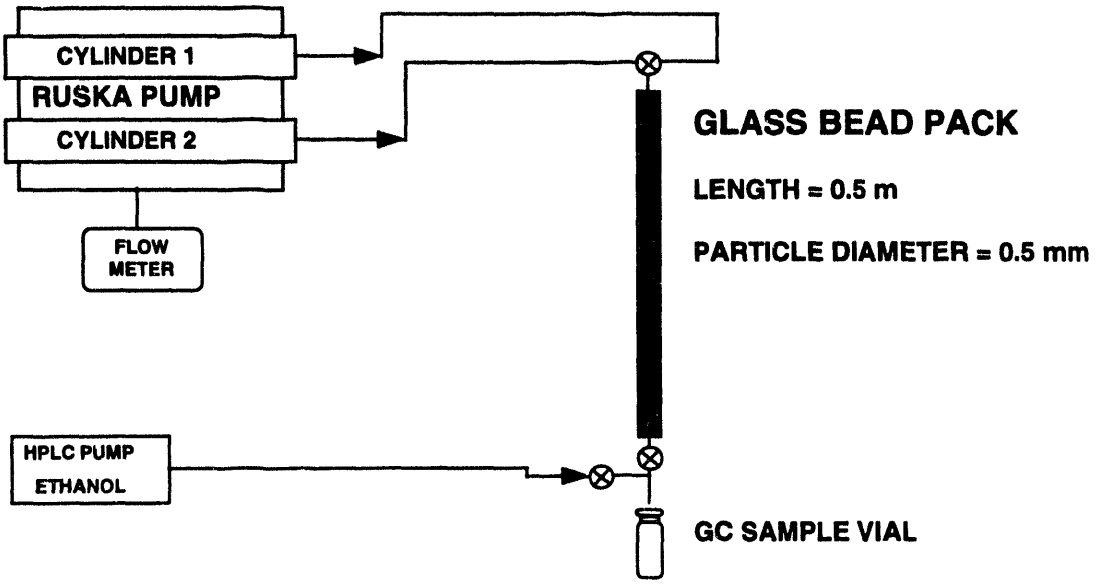

Figure 4.2: Experimental Equipment

4.1.2 Equipment and Procedure

All flow experiments were conducted with a 0.5 m long 0.0244 m diameter glass bead packed column (Fig.4.2). Standard glass beads of 35-40 mesh size were used, giving a column porosity of 35.7%. Nylon end plugs with 70 mesh screens held the bead pack in place.

The inlet header is connected to two inlet lines from a Ruska pump. Each cylinder contains either the initial column composition or the injection composition. The pump speed, which is held at a constant rate for the duration of a given run, can be varied from 0.1 cm^3/min up to 16 cm^3/min.

The fluid flowed out of the exit header and was collected in vials for GC analysis. Also attached to this header was an ethanol line. Ethanol was added at this location of the displacement process to make single-phase mixtures for any two-phase samples that resulted from runs that passed through the two-phase region. Single phases were then analyzed by chromatography.

For each run, exit fluid sampling was done by hand. The sampling rate was a function of the resolution in the production composition profile desired. A high frequency of sampling was used near the arrival times of shocks (4 per minute), while a low sampling rate (1-5 minutes per sample) was used when exit compositions changed slowly. On average, 40-70 samples were taken for a given run with each sample containing about 0.3% PV of fluid. At the end of each run the column was flushed with ethanol and all contents were collected and measured to determine the final mass of each component in the column.

4.1.3 Dispersion

One of the main assumptions in the derivation of the analytical solutions is that all displacements are dispersion free. In any laboratory displacement there will be some dispersion, but its effects can be limited by operating at conditions where the Peclet number (N_{Pe}) is large; i.e ., $N_{Pe} > 100$.

Lake points out that at laboratory flow rates the Peclet number can be defined as [39],

$$N_{Pe} = \frac{L}{\alpha_l} \tag{4.1}$$

where L is the displacement length and α_l is the medium dispersivity in the longitudinal direction. Dispersivity is a function of the medium only, its packing arrangement and particle size.

For the glass bead pack described above, fully miscible displacements of IPA by a solution of 70% IPA and 30% NPA were conducted to measure the medium's dispersivity, and hence the magnitude of the Peclet number. Analysis of two such displacements yielded, $\alpha_l = 0.002$ m giving $N_{Pe} \approx 255$. Thus, a low level of dispersion was present, and shocks predicted by the theory were smeared slightly in the experiments.

4.1.4 Viscous Stable Displacements

The MOC theory also assumes that all displacements are stable. The stability assumption implies that there is no fingering of injected fluid as a result of viscous or gravity forces. In cases where the injected fluid is more mobile and less dense (i-C_8-rich) than the initial fluid (water-rich), gravity forces can be used to eliminate viscous fingers if the displacement is downwards. The maximum (critical) rate at which the front will remain stable is given by Richardson as [56],

$$V_{cr} = \frac{(\rho_j - \rho_i)\sin\alpha}{\mu_i/k_i - \mu_j/k_j}. \tag{4.2}$$

For the case when a more viscous fluid (water-rich) displaced a less viscous fluid (i-C_8-rich), the displacement was always stable over laboratory flow rates. Experiments of this type showed plug flow with little two-phase flow occurring. Those runs provide minimal information to test MOC theory. Thus for the three-component system used here, useful displacements can proceed in only one direction on the phase diagram. The i-C_8-rich phase must displace the water-rich phase. A similar conclusion applies to the four-component system.

4.1.5 Capillary Forces

Capillary pressure differences are also not included in the MOC theory. However, they are always present in laboratory displacements that exhibit two-phase flow. Capillary forces can smear sharp fronts and cause hold up of the wetting fluid at the outlet end of the bead pack.

Samra and Bentsen [59] have defined the capillary number below

$$N_c' = \frac{A_c K_{wor}}{V L \mu_w} \tag{4.3}$$

to characterized the stability of saturation profiles. They suggest that phenomena due to capillarity, including end effects, are minimized when $N_c' < 0.1$. Eq.4.3 can be rearranged to give the minimum flow velocity needed to satisfy that requirement. For non-equilibrium displacements Eqs. 4.2 and 4.3 were applied to the two limiting (injection and initial) tie lines. Thus, two sets of results for maximum allowable flow rate and the magnitude of capillary effects were obtained. In practice, calculations based on the initial tie line generally determined the desired flow rate, because the saturation changes are greatest across the initial shock on this tie line.

Table 4.2: Run 5E, LVI-Vaporizing Type

Initial Composition	40% H_2O; 60% IPA
Injection Composition	100% i-C_8
Actual Flow Rate (cm^3/min)	3.417
Max Stable Flow Rate (cm^3/min)	6.8
N_c'	0.0074
N_{Pe}	255

4.2 Results

Johns described the four classes of displacements that can occur in a three-component displacement [34]. For the phase diagram previously described, only two of the four classes can be examined in these experiments (stability argument). We are specifically restricted to low-volatility intermediate (LVI) component-type displacements, where an i-C_8-rich phase displaces a water-rich phase. In the LVI-type, the two displacements are either vaporizing or condensing. The distinction based on MOC theory is in how the displacement switches between the injection tie line and the initial tie line. Vaporizing displacements exhibit an intermediate shock, while condensing displacements will have a continuous variation of compositions between the tie lines.

In this section the two classes of displacements are examined and compared with analytical results.

4.2.1 Vaporizing Displacement

A vaporizing displacement on the phase diagram in Fig.4.1 occurs when the IPA fraction in the vapor phase increases as the displacement proceeds. Any displacement where the initial tie line is above the injection tie line will suffice. In this type of process, the greater the separation between the initial and injection tie lines, the more pronounced the intermediate shock.

Run 5E was performed with an initial tie line IFT of 0.5 mN/m and an injection tie line coincident with the base of the phase diagram (water - i-C_8). The properties of this run are summarized in Table 4.2. The production path and analytical solution in flowing composition space are shown in Fig.4.3. The production profiles and corresponding analytical solution are shown in Fig.4.4.

A mass balance summary is shown in Table 4.3. The balance shows that total mass was conserved although water production was under estimated somewhat. This is a reflection on the accuracy of integrating the production data. The integral of this data, cumulative recovery of each component, is show in Fig.4.5. All data are normalized with respect to the total mass originally present at the start of the displacement (73.5 g).

Construction of the Analytical Solution

To construct the analytical solution, the main piece of information required, aside from phase behavior, is the fractional flow function for each tie line the displacement occurs on. In this LVI type displacement, only the initial and injection tieline flow functions are needed since a jump (shock) occurs between the two. Hence the analytical solution based on MOC is quite simple to construct.

Fractional flow functions were determined by running a displacement along each individual tie line (equilibrium displacement). For Run 5E, such a displacement was only performed for the

Table 4.3: Run 5E, Material Balance Summary

Component	Initial (g)	Injected (g)	Produced (g)	Remaining (g)	Lost (g)
Water	29.4	00.0	23.6	0.007	5.79
IPA	44.1	00.0	45.3	0.273	-1.52
i-C_8	00.0	172.3	116.9	57.89	-2.46
Total	73.5	172.3	185.8	58.17	1.81

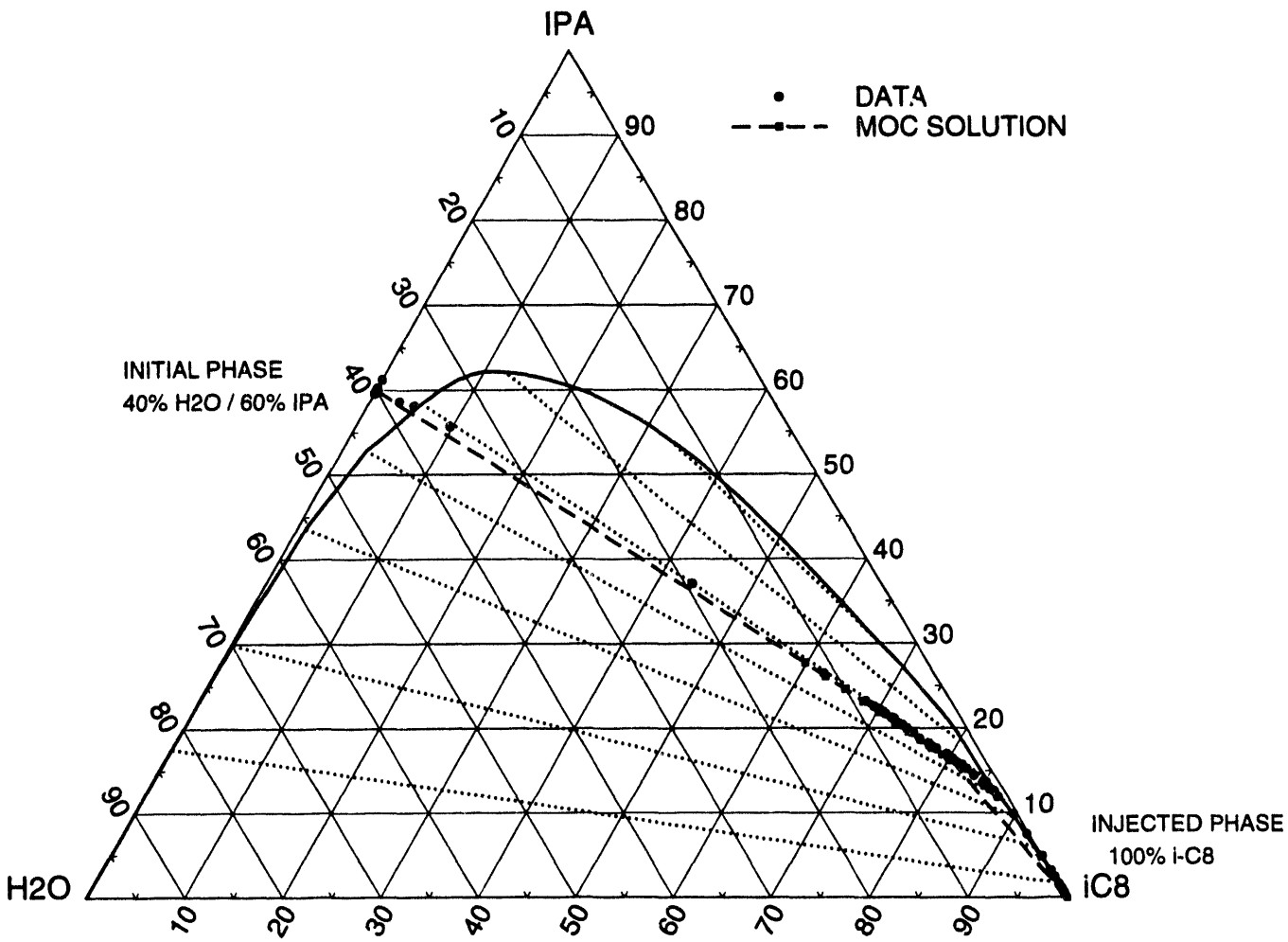

Figure 4.3: Run 5E, Flowing phase composition path.

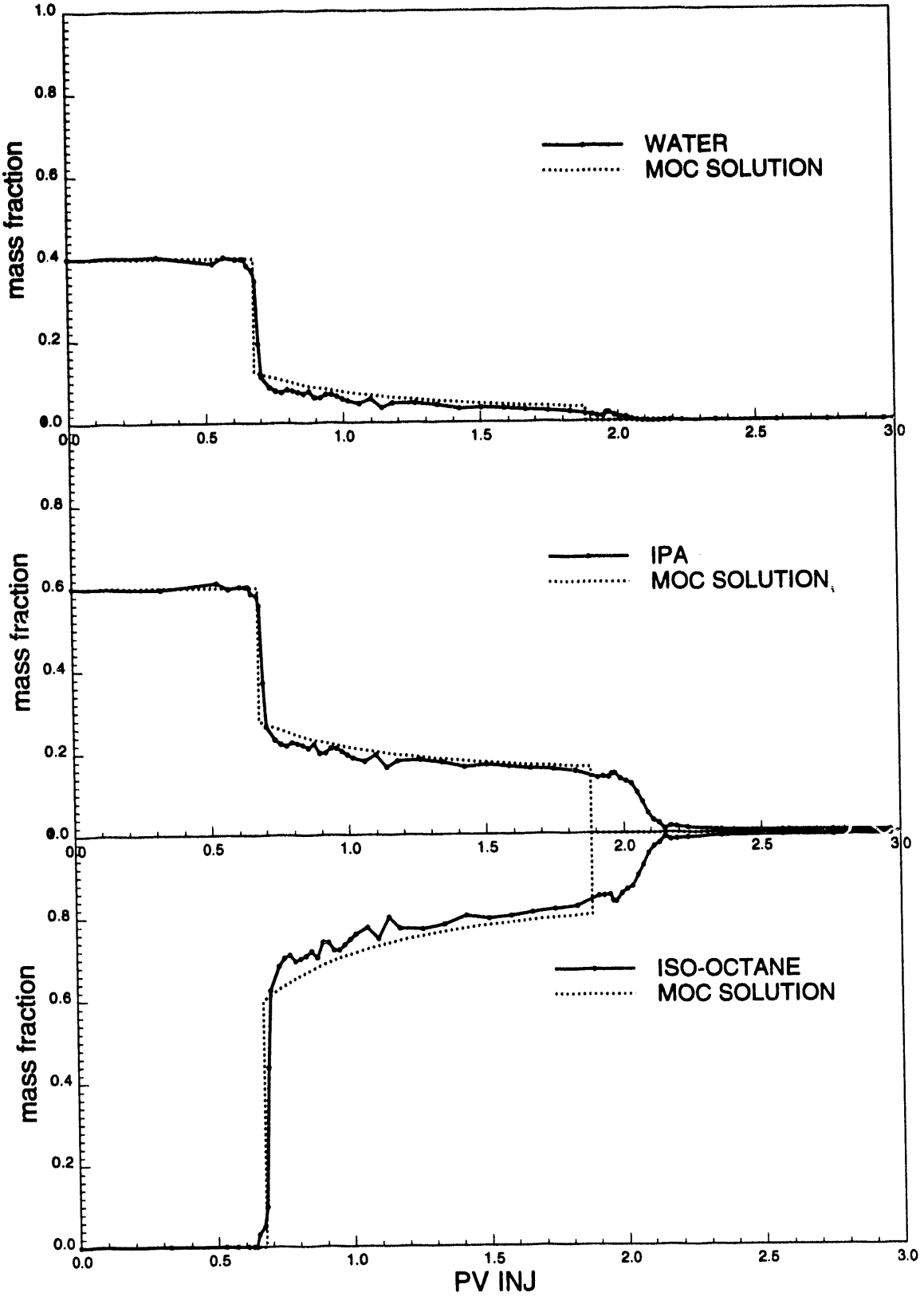

Figure 4.4: Run 5E, Component production profiles.

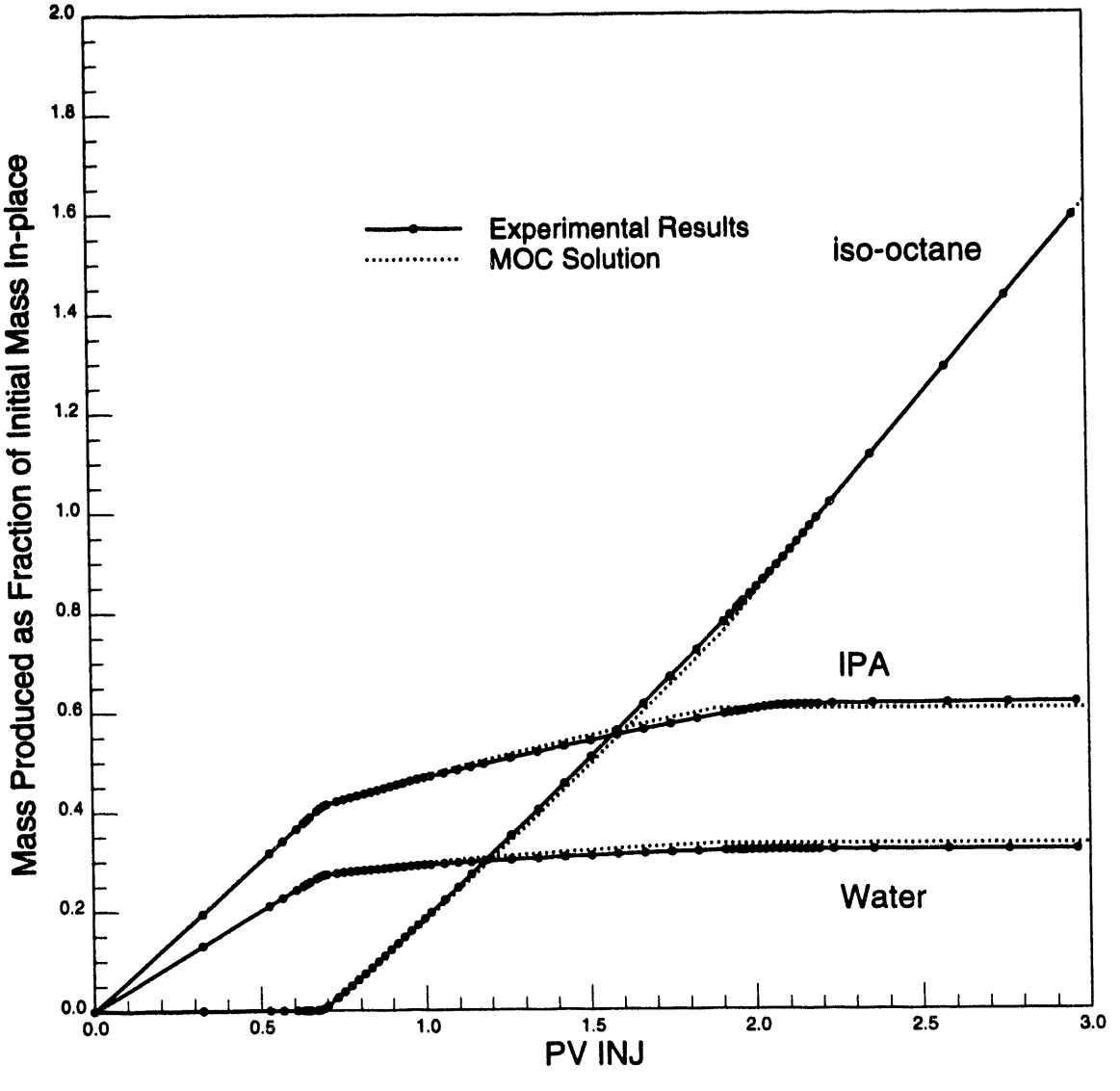

Figure 4.5: Run 5E, Normalized component mass produced, (as % of original total mass in-place).

initial tie line, and the fractional flow function calculated. Relative permeability data from Leverett were used to determine the fractional flow curve for the injection tie line [41].

The MOC solution was calculated using a small spreadsheet program. This program solves the shock balance equations for the initial and intermediate shock on the initial tie line. The continuously varying zone between the two shocks is constructed next.

Discussion

Figs.4.3, 4.4, and 4.5 all show excellent agreement between the MOC solution and measured data. The figures clearly show that the initial shock and following continuous variation occur on the tie-line extending through the initial composition. The intermediate shock is also seen in both data sets. For this particular run, the injected phase is on the binodal curve so there is no trailing shock to allow the final column composition to reach 100% i-C_8. A shock would only occur if the injected phase were outside of the two phase region. In fact the final measured column composition indicates that there was still 0.4 % of the initial water phase by volume remaining.

Note that the intermediate shock landing point is on the binodal curve at the injection composition, implying single-phase production of i-C_8. This occurs because flowing compositions are measured. The analytical solution is initially cast to track total compositions, but to compare with lab data, the solution is converted to flowing compositions via the fractional flow curve for each tie line. The end result is that since the residual wetting phase saturation on the injection tie line is 10%, but the landing point (in total composition space) occurs at S_w = 5%, only the nonwetting phase (i-C_8) flows. The fractional flow of the water phase is zero.

Finally, examination of Fig.4.4 shows a slight difference in arrival times for the trailing shock. This trailing shock arrival time differs by about 8% from the actual time. The cause is due to evaluating a tangent shock on the fraction flow curve where the curvature is almost flat, making the actual tangent point difficult to calculate.

4.2.2 Condensing Displacement

Displacements in which the injection tie line lies above the initial tie line on Fig.4.1 are condensing drives, according to the terminology in standard use. Run 7D was performed to test the agreement of the analytical solution for a condensing displacement with a spreading wave associated with the nontie-line path. Again a large initial and injection tie-line separation will result in a pronounced nontie-line path. This choice is balanced with keeping IFT's on the initial tie line low enough that capillary forces do not influence the experiment unduly. Hence an intermediate tie line was chosen, rather than the pure water i-C_8 tie line.

Fig.4.6 shows the measured flowing composition path of an LVI-condensing type run. The properties of this run (Run 7D) are summarized in Table 4.4, and a material balance summary is given in Table 4.5. Again there were slight errors invloved in integrating the prodution data to determine cumulative masses produced, but overall only 6 grams was unaccounted. The production profiles are shown in Fig.4.7 and cumulative recovery profiles in Fig.4.8.

Construction of the Analytical Solution

Constructing analytical solutions to include a variation along the nontie-line path for a real system is considerably more difficult than the previous case. The primary reason is that the nontie-line path cannot be determined by shock balances, rather an eigenvalue problem like that outlined by Johns must be solved [34]. Data on all tie-lines, between the limiting two, is also required to make the calculation.

A fortran program was written to calculate the MOC solution. The phase envelope was modeled based on the measured diagram. It is divided into seven regions (Fig.4.6) such that any

Table 4.4: Run 7D, HVI-Condensing Type

Initial Composition	70% H_2O; 30% IPA
Injection Composition	87% i-C_8; 13% IPA
Actual Flow Rate (cm^3/min)	2.051
Max Stable Flow Rate (cm^3/min)	9.0
N_c'	0.082
N_{Pe}	255

Table 4.5: Run 7D, Material Balance Summary

Component	Initial (g)	Injected (g)	Produced (g)	Remaining (g)	Lost (g)
Water	57.9	00.0	57.9	4.62	-4.62
IPA	24.8	30.0	42.4	10.9	1.50
i-C_8	00.0	201.0	153.4	50.73	-3.13
Total	82.7	231.0	253.7	66.3	-6.25

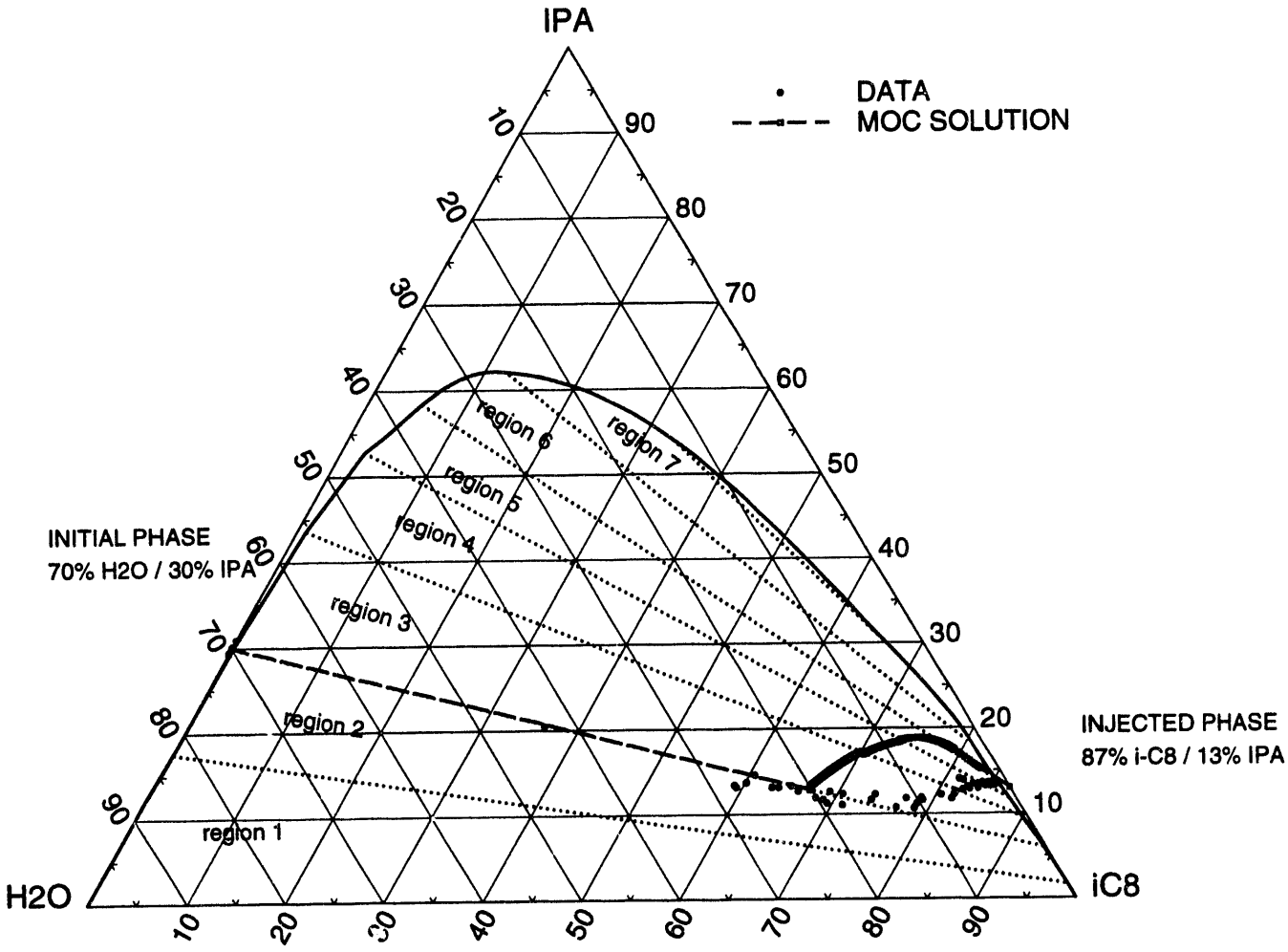

Figure 4.6: Run 7D, Flowing phase composition path.

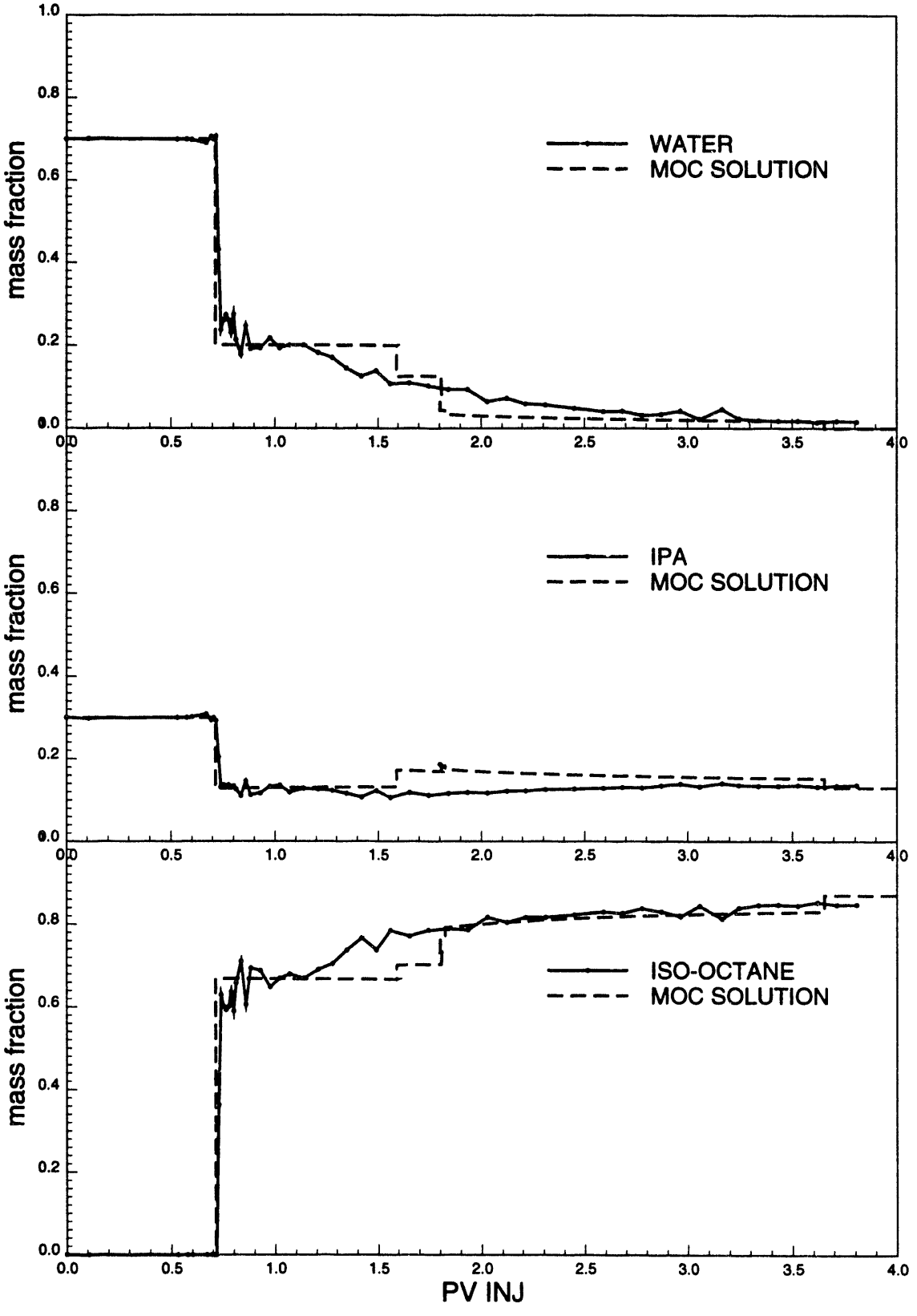

Figure 4.7: Run 7D, Component production profiles.

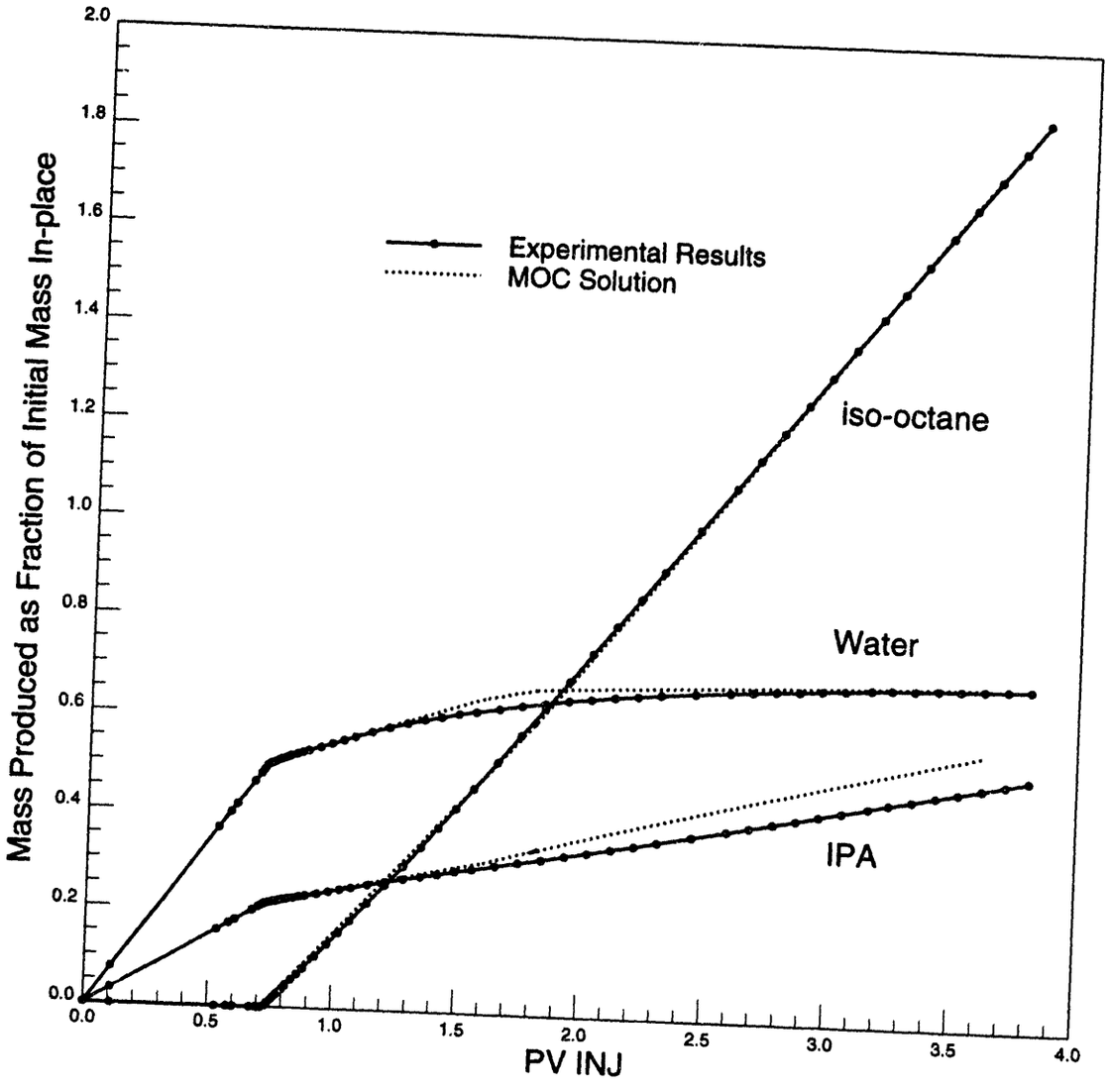

Figure 4.8: Run 7D, Normalized component mass produced, (as % of original total mass in-place).

tie line between two measured tie lines all share the same intersection point. This ensures that tie lines do not cross. The binodal curve in any region is assumed to be made of straight-line segments connecting any two measured tie-line end points. All fractional flow properties on any tie-line within the limiting injection and initial tie lines, were interpolated based on the known fractional flow properties of these limiting tie lines.

Discussion

Comparison of analytical profiles with measured data in Fig.4.7 show that the theory predicts the initial shock on the initial tie line quite well, but after this point, actual production response lacks the analytical detail. However, the match on the cumulative recovery plot (Fig.4.8), is still very good considering these deviations in profile solutions.

Interfacial tensions were high enough that slugging of the two phases occurred immediately following the arrival of the initial shock. Sample volumes were small enough that this effect caused measured compositions to vary significantly. Thus the measured concentration profiles between 0.7 and 0.9 PV injected, oscillate rather than remaining constant as in the MOC solution.

The series of shocks between 1.6 and 1.8 PV injected represent the velocity change as the analytical solution moves from the initial tie line to the injection tie line (nontie-line path). Several uthors have shown that when tie-line intercepts are constant, wave velocities are also constant [34, 39]. For this case the nontie-line path passes through four regions so there are four associated velocities. Thus the nontie-line path shocks are a result of how the phase diagram is modeled.

Modeling the binodal curve as a series of line segments also affects the nontie-line path calculation. The derivative of vapor fraction compositions do not vary smoothly between phase envelope regions, which affects the nontie-line eigenvector direction at region edges. Fig.4.6 shows for example that the nontie-line path shifts where two of the tie lines are crossed, and the solution is no longer on the correct path. Since the intercepts in regions 4 and 5 are almost the same, but the path is incorrect, the velocities in region 4 actually decrease slightly (Fig.4.7). This violates the velocity constraint, but really is caused by the way the phase diagram is modeled, and not problems with the MOC theory. The correct application of MOC theory would actually require a shock jump over the offending increase in velocity.

Although the above discussion explains why the nontie-line path has the appearance calculated, the important observation to note is that Fig.4.6 clearly shows the measured nontie-line path shifted towards the nonwetting phase side of the diagram relative to the solution. This implies that production of the wetting phase is being delayed somewhat. Dispersion can be ruled out since this would shift the data to the left of the MOC solution [68]. The fact that there was slug production after the initial shock and the wetting phase is being held up suggest that capillary forces have not been completely eliminated.

A second run at twice the injection rate (3.4 cm^3/min) resulted in a similar composition path with only a slight shift in data towards the right of the nontie-line path. For this case N_c' was 0.05. Over this velocity range, neither run confirmed or denied that capillary forces affected the wetting phase production. Displacements at still higher rates could be performed to test whether capillary forces were responsible for the shift. However, increased rates would reduce production data resolution, and the flow rate would exceed the maximum stable flow rate on the injection tie line of approximately 5 cm^3/min. Above this rate, the density difference would not be large enough to prevent the less viscous injection phase from fingering through the water-rich phase.

With respect to capillary effects, the concern here is assumptions involved in calculating the minimum velocity based on Eq. 4.3 may not be correct for the bead pack and phase diagram being used. The validity of these assumptions will be examined further before four-component experiments are performed.

4.3 Conclusions

Considering the assumptions made to arrive at the MOC solution, and the simplicity of doing analytical calculations, the agreement with experimental data is very good. Figs.4.4 and 4.6 both exhibit displacements that progress along tie lines extending through initial and injection phases respectively. The leading shock arrival times are properly predicted, and recovery curves are quite close. Material balance results prove the experimental ability to measure two-phase displacements very accurately.

Run 7D clearly shows the necessity of understanding the various forces affecting a displacement. Once the minimization of capillary forces is properly understood, the four-component system can be tested.

A self-sharpening solution for a real system was constructed based on MOC theory (vaporizing displacement), showing good agreement with actual data. The construction of the condensing displacement was more difficult due to a continuous variation along the nontie-line path. The current solution requires a better model for each binodal curve (vapor, liquid) such that the derivatives of compositions are continuous throughout the phase diagram. An improved phase representation will avoid minor errors in determining the nontie-line path.

In four-component runs the condensing/vaporizing displacement will be composed of both a self-sharpening and continuously varying nontie-line path. Construction of the analytical solutions for this real system will require solution of a three-dimensional eigenvalue problem. All of the flow properties determined in the three-component analysis can be extended to four-component systems, since the addition of NPA will not change flow or phase behavior greatly. An accurate test of the C/V displacement theory and the existence of the crossover tie line will be conducted based on these results.

5. Interplay of Capillary, Gravity, and Viscous Forces in Heterogeneous Media

In this chapter, we examine the interplay of forces that drive flow between zones with different permeability. Consider, for example, a near-miscible gas injection process in a fractured reservoir. Because the process is not quite miscible, two-phase flow occurs. Capillary forces created by the interfacial tension (IFT) act to hold the oil in the rock matrix, while the density difference between gas and oil drives oil out of the matrix. The relative magnitudes of the capillary and gravity forces determine the final oil recovery. At the same time, the gas phase moves more rapidly in the fractures, and buoyancy forces move the gas phase flow upwards. The balance of gravity and viscous forces governs the distribution of oil and gas phases in the fractures, consequently, the oil recovery mechanisms. Thus, understanding the scaling of the interplay of the capillary, gravity and viscous forces is of considerable importance to the description of near-miscible gas injection performance.

In Section 5.1, we present simulations of our imbibition experiments with various IFT's. Our simulations show that there is a transition from the capillary-driven, countercurrent flow to the gravity-driven, cocurrent flow as IFT decreases, which agrees with our experimental observations. We also offer a explanation for the high recovery efficiency from the low IFT imbibition experiments. In Section 5.2, we report a theoretical study of scaling of multiphase flow in simple heterogeneous media, such as, layered and fractured reservoirs. We define three scaling parameters, which represent the relative magnitudes of the capillary, gravity and viscous forces in a system. Among the scaling groups, the transverse gravity and capillary numbers are different from the conventional definitions. Based on the values of the scaling parameters, we identify flow regimes in which certain forces dominate the flow. The boundaries between regimes were defined from the existing experimental and simulation results in the literature.

5.1 Simulation Results for Imbibition Experiments

Darryl H. Fenwick

5.1.1 Simulation of Imbibition Experiments

Numerical simulation is an important tool in the understanding of experimental results. Hamon and Vidal [28] were able to simulate a wide variety of laboratory imbibition tests and were able to show that the scaling parameters put forth by du Prey [20] proved reliable if the heterogeneity of the core was taken account in the simulation. This result could only be proved by numerical simulation. Simulation also can aid in the understanding of the physical mechanisms underlying the process. Certain parameters can be easily varied to determine how they affect the process of interest.

The results of Hamon and Vidal were vital to the understanding of the scaling of imbibition experiments. However, they did not investigate how the scaling parameters behaved when the IFT is varied. Scaling behavior with IFT variation is an important issue when enhanced oil recovery is concerned. Schechter *et al.* [60] provided results of core displacement experiments where the IFT was varied in imbibition. The results of the experiments showed recovery behavior which was inconsistent with capillary-dominated scaling rules. (For a discussion of scaling see [60] and Section 5.2). In this section we use a numerical simulator (ECLIPSE) to obtain insight into the results

of Schechter *et al.* The results of the simulations reveal what physical mechanisms are dominant and how scaling of these imbibition experiments behaves. The results also demonstrate certain limitations of the numerical simulator for simulation of imbibition.

Input Data

The proper input into a simulator is critical if the physics of the experiments are to be captured. Hamon and Vidal demonstrated that a tremendous amount of characterization of the heterogeneity on the core is needed for scaling to be done properly. In fact, a complete description of the varying relative permeabilities and capillary pressures along the core is necessary. This point is also emphasized by Bourbiaux and Kalaydjian [8], who found that countercurrent imbibition relative permeabilities were quite different than cocurrent imbibition relative permeabilities. According to the arguments of Bourbiaux and Kalaydjian, the type of flow regime must be understood before appropriate relative permeability functions can be specified. Unfortunately, these functions are not well known for the experiments of Schechter *et al.* [60]. The heterogeneity of the cores is not characterized, and only single values of the permeability are given. However, Berea is a fairly homogeneous sandstone, so the assumption of constant permeability throughout the Berea cores may be acceptible. Hence, the 500 md Berea core results were selected to be investigated. The experiments done at high IFT (38.1 mN/m) on the 500 md Berea core will subsequently be referred to as the high IFT case, and the low IFT (0.1 mN/m) experiments will be referred to as the low IFT case.

Capillary Pressure

Because the imbibition experiments were done without initial water in the core, primary imbibition capillary pressure curves are needed. Unfortunately, they cannot be found in the literature for Berea. Capillary pressure curves were obtained by extrapolating secondary imbibition curves to zero water saturation. This process does not obtain the correct curve, but the emphasis of this work is not to find an exact match to the imbibition recovery curve. It is the understanding of the physical mechanisms behind imbibition as the IFT is varied that is of interest.

Fig. 5.1 shows the positive values of capillary pressure used for three different simulations. The high IFT and low IFT capillary pressure curves are shown, as well as the capillary pressure curve for a low IFT experiment run with 19% initial water saturation (IWS) in the core. This experiment will be introduced in the Discussion. A logarithmic scale is used to demonstrate how the low IFT curve is over two orders of magnitude smaller in value than the high IFT curve. The difference in capillary forces will become important later when the effects of gravity on the imbibition behavior are considered. The Berea core was assumed to be strongly water wet, so the negative portion of the capillary pressure curves was essentially a vertical line.

Relative Permeability

The relative permeabilities for the low IFT and high IFT experiments were determined by history match of the experimental recovery curve. Fig. 5.2 gives three different sets of relative permeability curves which were used to match the high IFT case recovery curve. The oil relative permeability curve was kept the same throughout the different simulation runs. Note that the three water relative permeability curves have extremely low values even up to high water saturations. Those low values will be important for the scaling of these experiments. The values of the k_{rw} III curve defined in Fig. 5.2 were used to produce the oil saturation profiles in Fig. 5.5, which will be discussed later.

Fig. 5.3 shows two different sets of relative permeability curves used for the low IFT case. These values for relative permeability were over two orders of magnitude larger at lower water

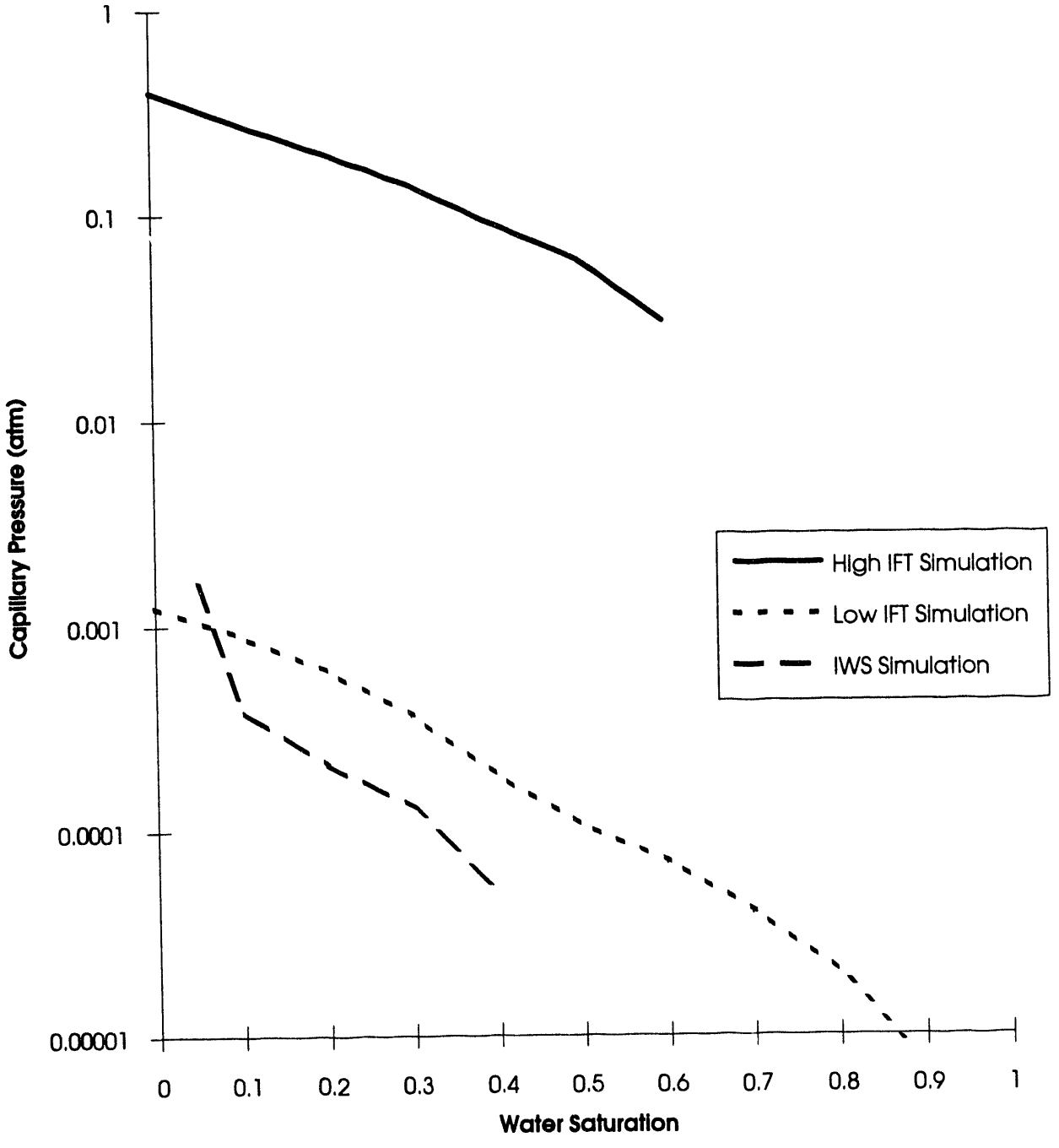

Figure 5.1: Capillary pressure curves for simulations of imbibition experiments.

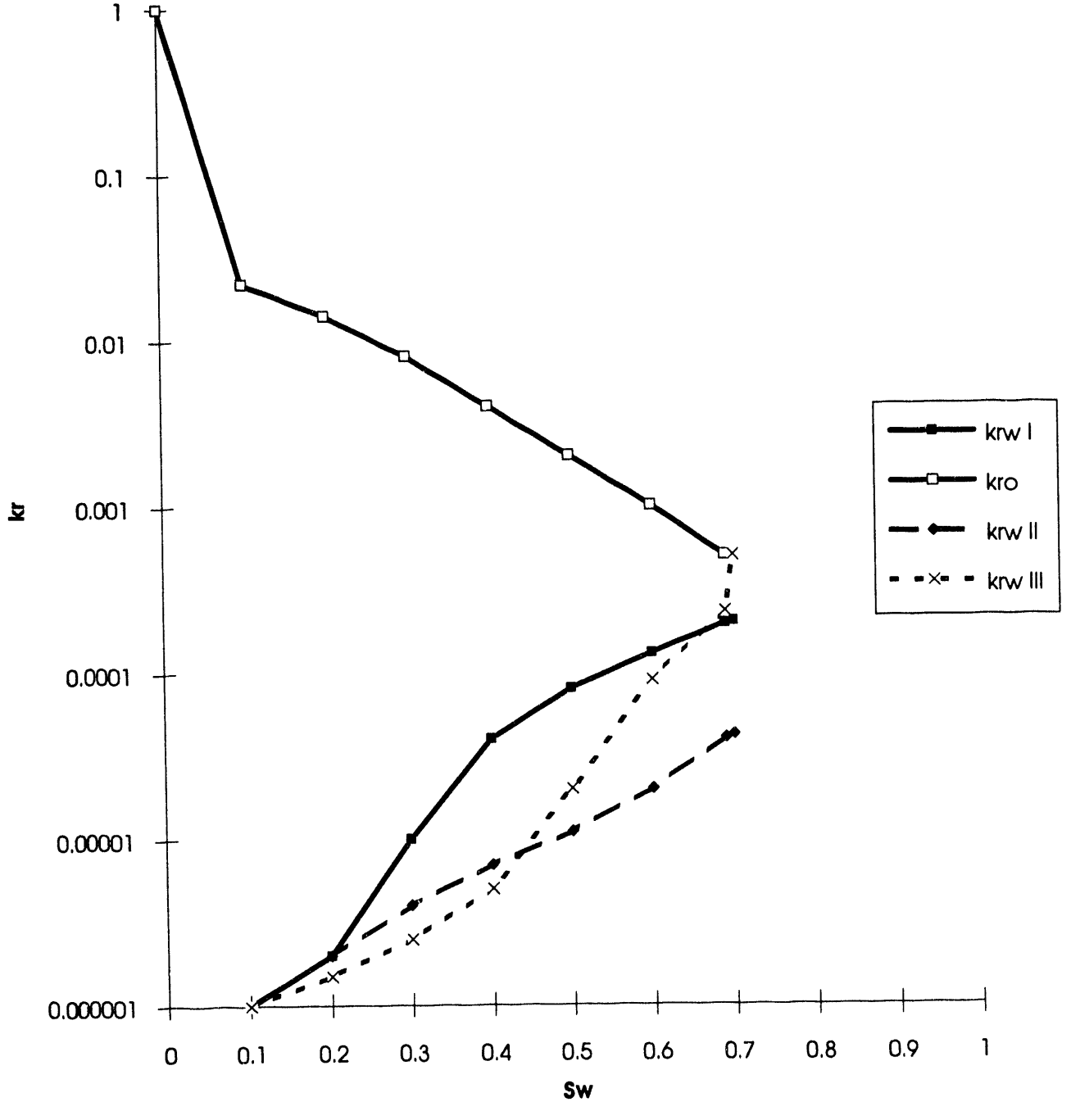

Figure 5.2: Relative permeability functions for high IFT imbibition.

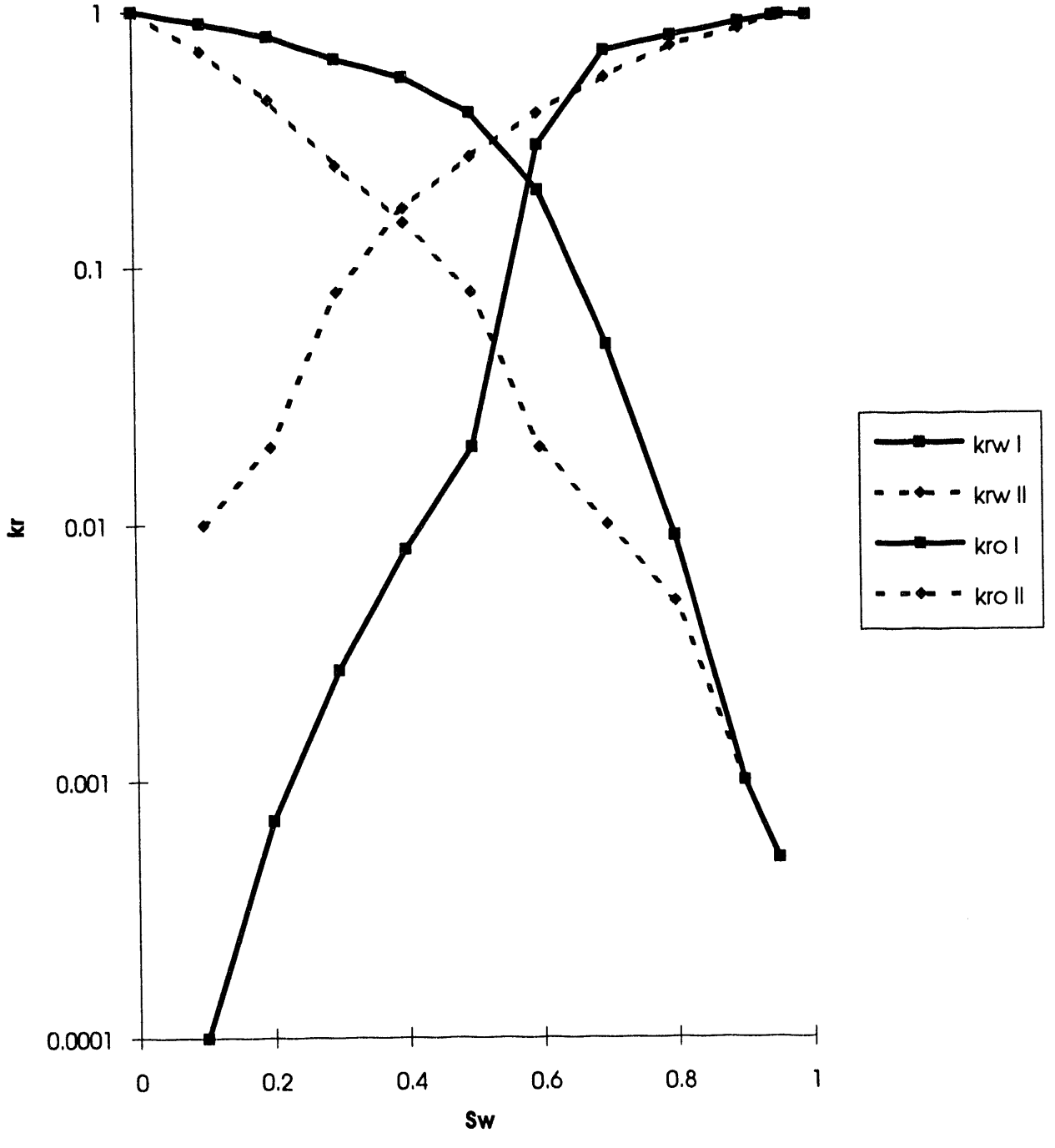

Figure 5.3: Relative permeability functions for low IFT imbibition

saturations than the values for the high IFT case. The values of the k_{rw} I and k_{ro} I curves in Fig. 5.3 were used in generating the oil saturation profiles in Fig. 5.9 to be discussed later.

Gridding Techniques

Sensitivity of computed results to the effects of gridding was investigated. Cylindrical coordinates were used to grid the core and annulus region. For the high IFT case, the core was separated into 59 vertical regions, with the top and bottom region representing the annulus above and below the core. The middle 57 regions were 1 cm in length covering the full length of the core. The core was divided up radially into 27 parts, logarithmically distributed over the core diameter (6.35 cm) such that the finest grid blocks were closest to the annulus. The annulus outside the core was represented by one radial block, so there were a total of 28 radial grid blocks for the high IFT simulations. This configuration was tested against simulations with 8 radial grid blocks and 57 radial grid blocks. The 28 radial grid block results were indistinguishable from the 57 radial grid block results, but were quite different than the 8 radial grid block simulation. It was then considered that 28 radial grid blocks were sufficient to grid the radial flow of the high IFT case accurately .

The low IFT case contained 122 vertical sections to capture more easily the significant vertical component of flow found in the low IFT experiments. Radially the core was set up into 15 sections in a similar manner as for the high IFT case.

Results

High IFT Simulations

The simulations showed a very high sensitivity to relative permeability. Fig. 5.4 shows the results for the three different cases of water relative permeability. Note that none of the curves show a good match to the experimental data. The very low relative permeabilities of the k_{rw} II curve matched the very early recovery time, but the curves of k_{rw} I and k_{rw} III match the recovery better at later times. Attempts to achieve a better match were unsuccessful. There is evidence that simulation of primary imbibition is a very difficult task. Kazemi and Merri [37] had to add a second capillary pressure curve to match the experimental results. The second curve was supposed to account for a "time delay" in the experimental recovery rate. They provided no physical justification for the addition of a second capillary pressure curve. Most important to note is that even for the very low relative permeabilities found in k_{rw} I and k_{rw} III, the simulations had orders of magnitude faster recovery at early times.

Because the k_{rw} III curve matched best the experimental recovery values, the average oil saturation profile along the core was plotted at selected intervals. These values simply averaged the oil saturation for each vertical layer of the core. Fig. 5.5 shows the results. Evidently, the oil saturation decreased in a uniform fashion, with the top and bottom part of the core showing equal additional reductions. The oil saturation decreased faster here than in the rest of the core due to the increased surface area in contact with the water-filled annulus. Note that at 0.1 hour (6 minutes) the average oil saturation was already down to 50% along the core, a very fast recovery rate. The lack of evidence for the segregation of oil and water in the core indicates that the flow was radial and countercurrent in nature.

Low IFT Simulations

Schechter *et al.* [61] proposed that in the scaling of the low IFT experiments, capillary effects can be neglected and the recovery is dominated by vertical gravity-driven flow. To examine this

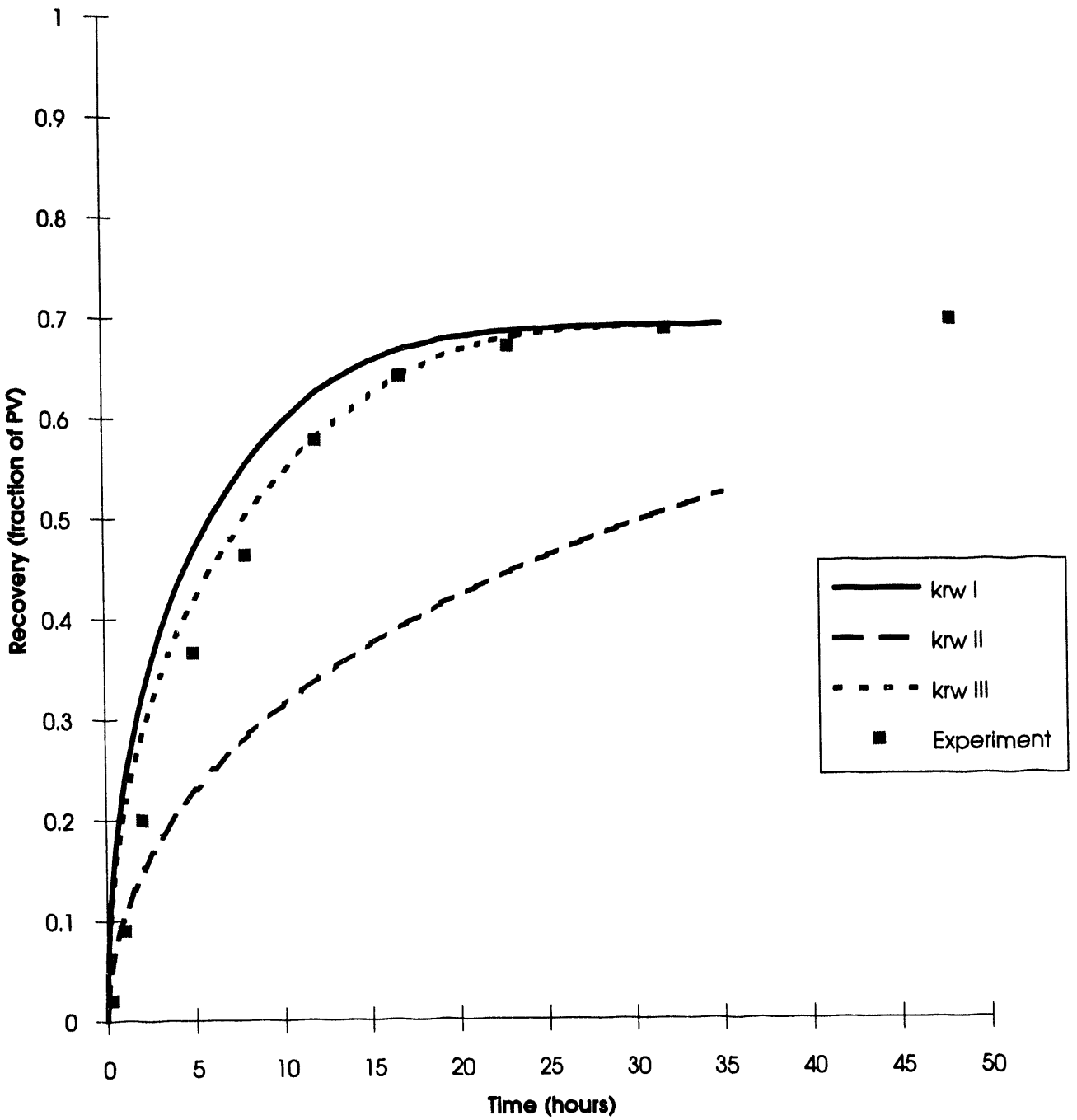

Figure 5.4: Comparison of simulation and experiment for recovery of oil by imbibition at high IFT.

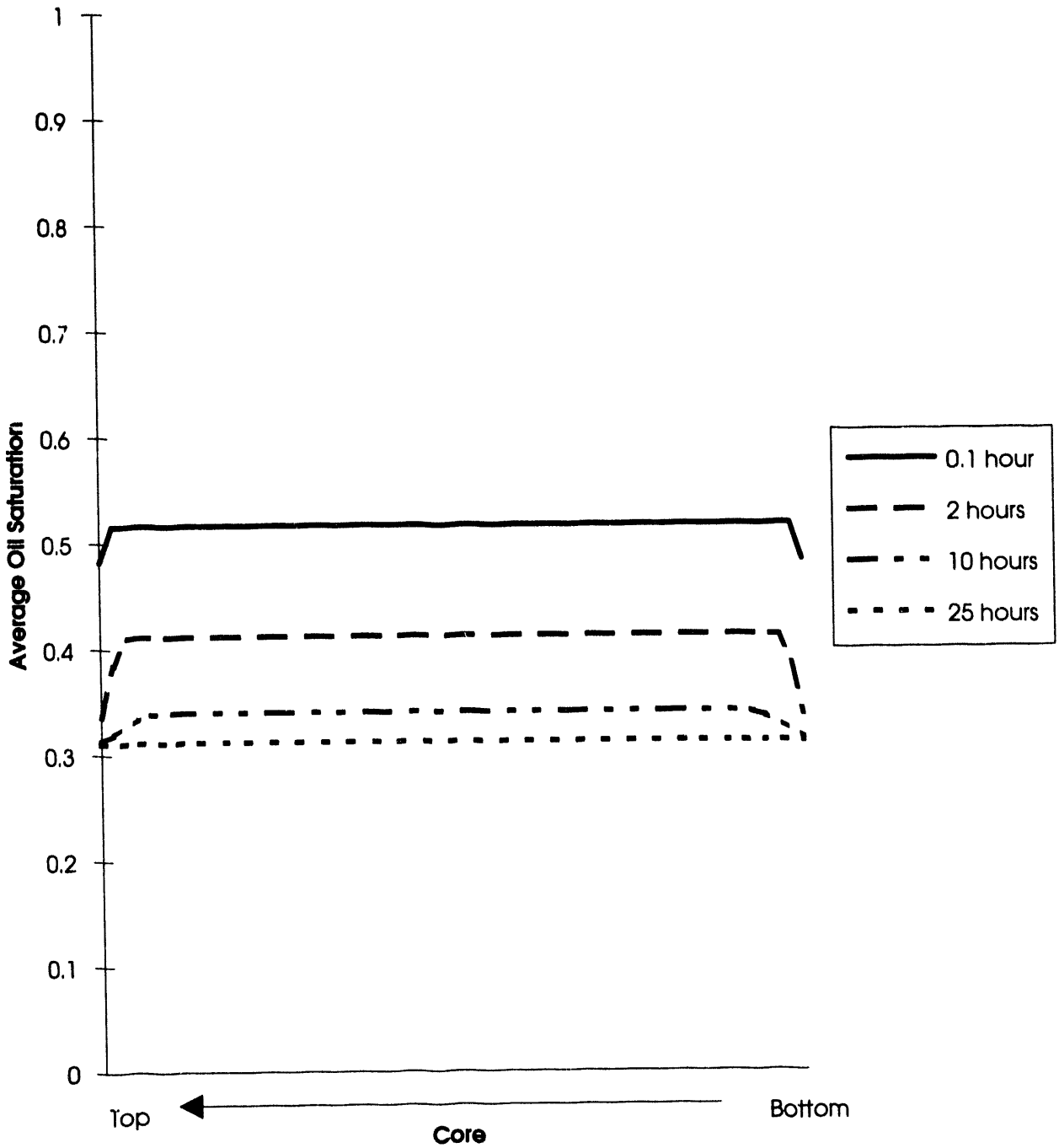

Figure 5.5: Oil saturation profiles during imbibition at high IFT.

assertion, a simulation run was performed where the IFT was set to zero and straight line relative permeability curves were used. The recovery is then due only to the difference in gravity between the oil and water. Fig. 5.6 indicates that the experimental recovery rate was in fact influenced significantly by capillary forces, because the density difference was insufficient to maintain the recovery rate at the level of the experiment. Therefore, capillary pressure must be considered as an important driving force even for these low IFT experiments. The average oil saturation profile for the gravity-driven displacement (Fig. 5.7) shows a very distinct water front advancing from the bottom of the core upward, with original oil saturations ahead of the front. The top of the core shows some oil desaturation due to the top annulus imbibing into the core due to gravity. As expected, the oil saturation profile shows segregation between the oil and water, resulting in largely cocurrent flow.

When the low IFT capillary pressure curve (shown in Fig. 5.1) is incorporated into the simulation, the relative permeability curves in Fig. 5.3 result in the recovery curves in Fig. 5.8. Note that as for the high IFT case, the early time recovery behavior does not match well. Note also that the poor match was obtained even though the water relative permeabilities at low water saturations were quite low, especially for the k_{rw} I curve. In addition, the late time recovery behavior also does not match the experimental results. Attempts to match the experiment better were unsuccessful.

Despite the poor agreement, some important conclusions can be constructed from these simulation runs. Fig. 5.9 shows the average oil saturation profile at different times for the low IFT displacement. Comparison of Fig. 5.9 to Fig. 5.5 indicates that there is an important distinction between the low and high IFT displacements. The low IFT case profile shows aspects of both the high IFT case profile and the gravity-driven flow saturation profile of Fig. 5.7. An advancing water front is evident, as well as a fairly uniform decrease in the oil saturation away from the advancing water front, indicating radial flow. Thus it seems likely that both radial and vertical flow contributed to recovery in the low IFT displacements.

5.1.2 Discussion

In the experiments in Schechter *et al.* [60] imbibition is driven by a combination of capillary and gravity forces. The capillary-to-gravity-force ratio, given by the inverse bond number N_B^{-1}, describes the type of flow that is exhibited in these experiments. Here, N_B^{-1} is given by,

$$N_B^{-1} = C\frac{\sigma\sqrt{\frac{\phi}{k}}}{\Delta\rho g h}$$

where σ is the IFT, $\Delta\rho$ is the difference in density between the phases, ϕ is the porosity, k is the permeability, g is gravity, h is the height of the core, and C is a constant depending on pore geometry. As the permeability and core length increase, and the IFT decreases, a transition from capillary-driven, countercurrent imbibition to more gravity-driven cocurrent segregation is demonstrated. For the cores described in Schechter *et al.* [61, 60] , the transition region has been identified as the N_B^{-1} varies from the capillary dominated region of around five to the gravity-dominated region around 0.2. The simulations described above reinforce these arguments. For the high IFT case, strictly capillary-dominated countercurrent flow was observed, with uniform desaturation of oil throughout the core. When the IFT was lowered, significant vertical cocurrent displacement of oil occurred. However, the assumption of strictly vertical plug flow was not observed in the low IFT case. Capillary forces still played a very important part in the recovery of the oil and cause some countercurrent flow to occur.

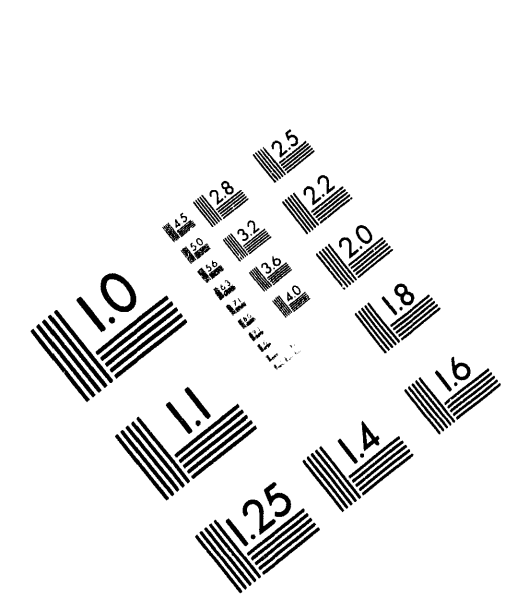

Association for Information and Image Management
1100 Wayne Avenue, Suite 1100
Silver Spring, Maryland 20910
301/587-8202

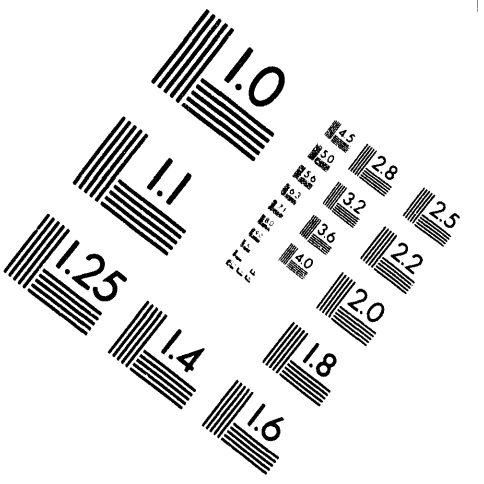

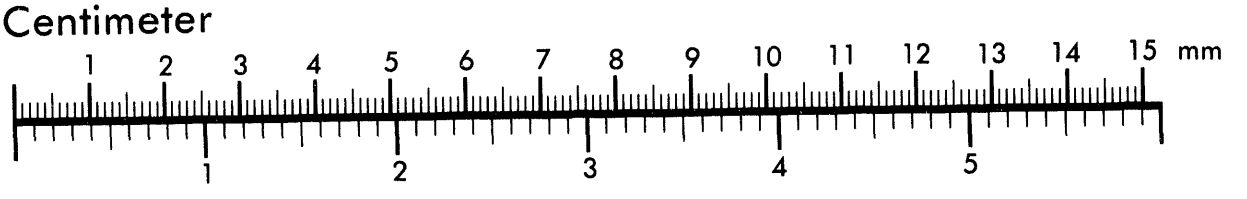

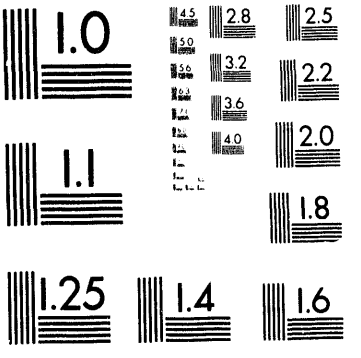

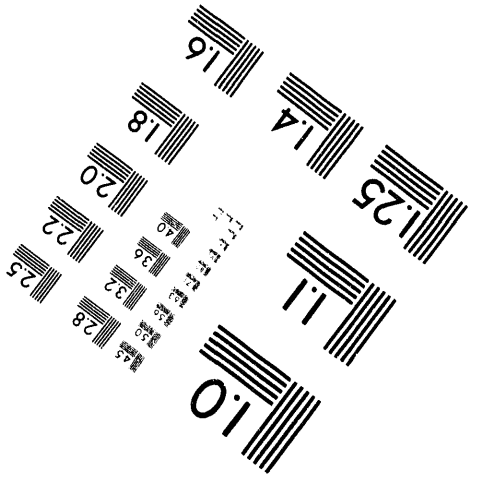

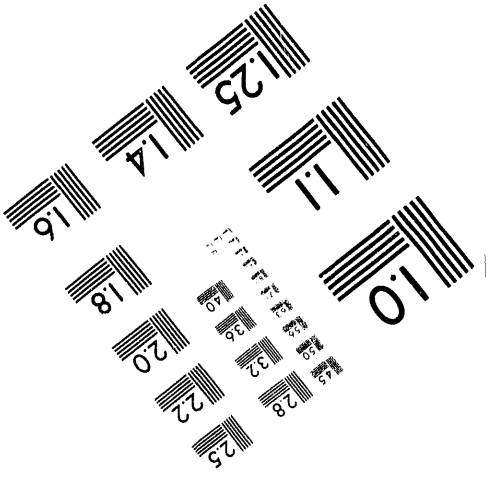

MANUFACTURED TO AIIM STANDARDS
BY APPLIED IMAGE, INC.

2 of 2

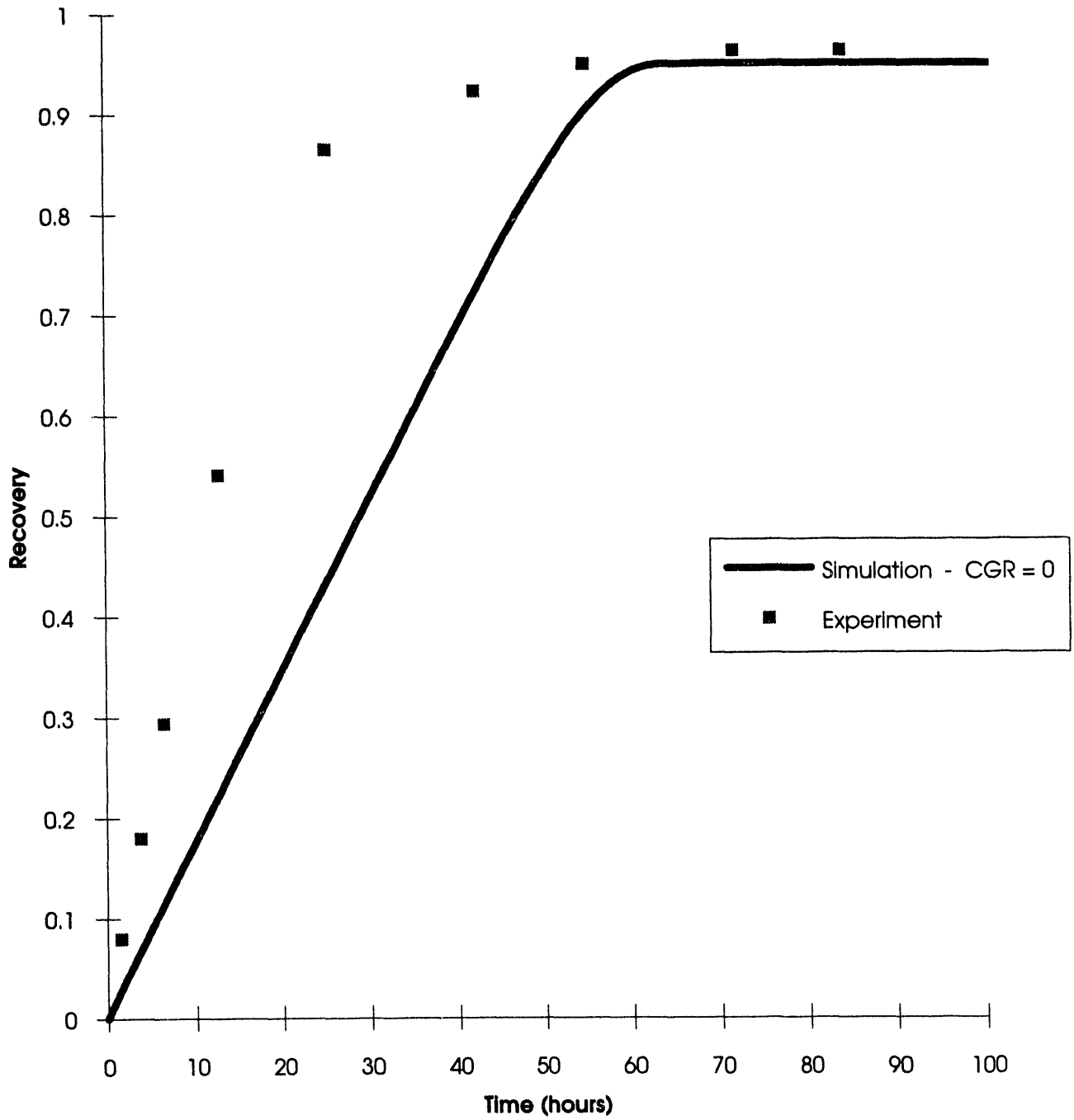

Figure 5.6: Comparison of simulation of gravity-driven vertical flow with expermental observations for low IFT imbibition.

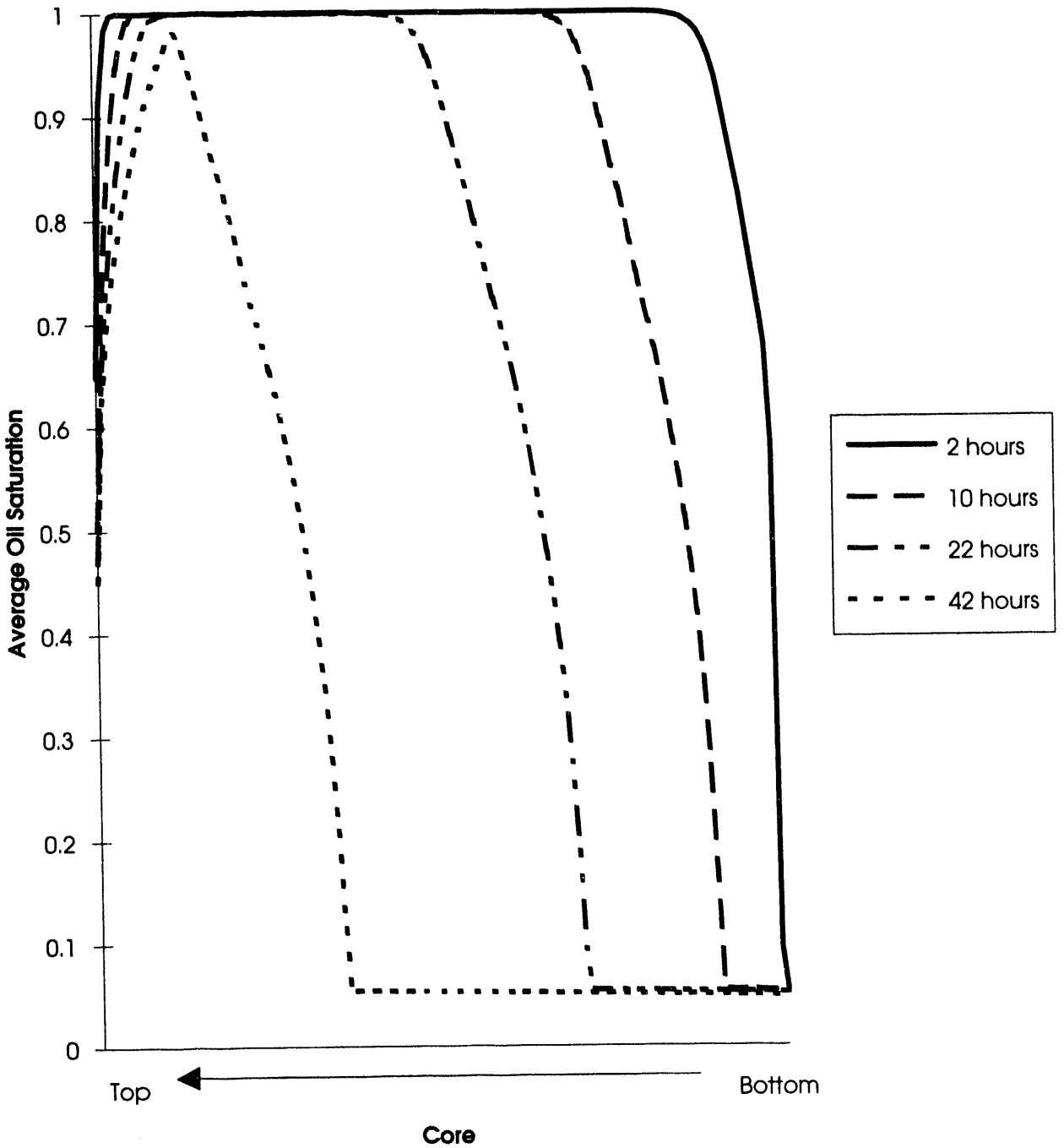

Figure 5.7: Oil saturation profiles during flow driven only by gravity forces.

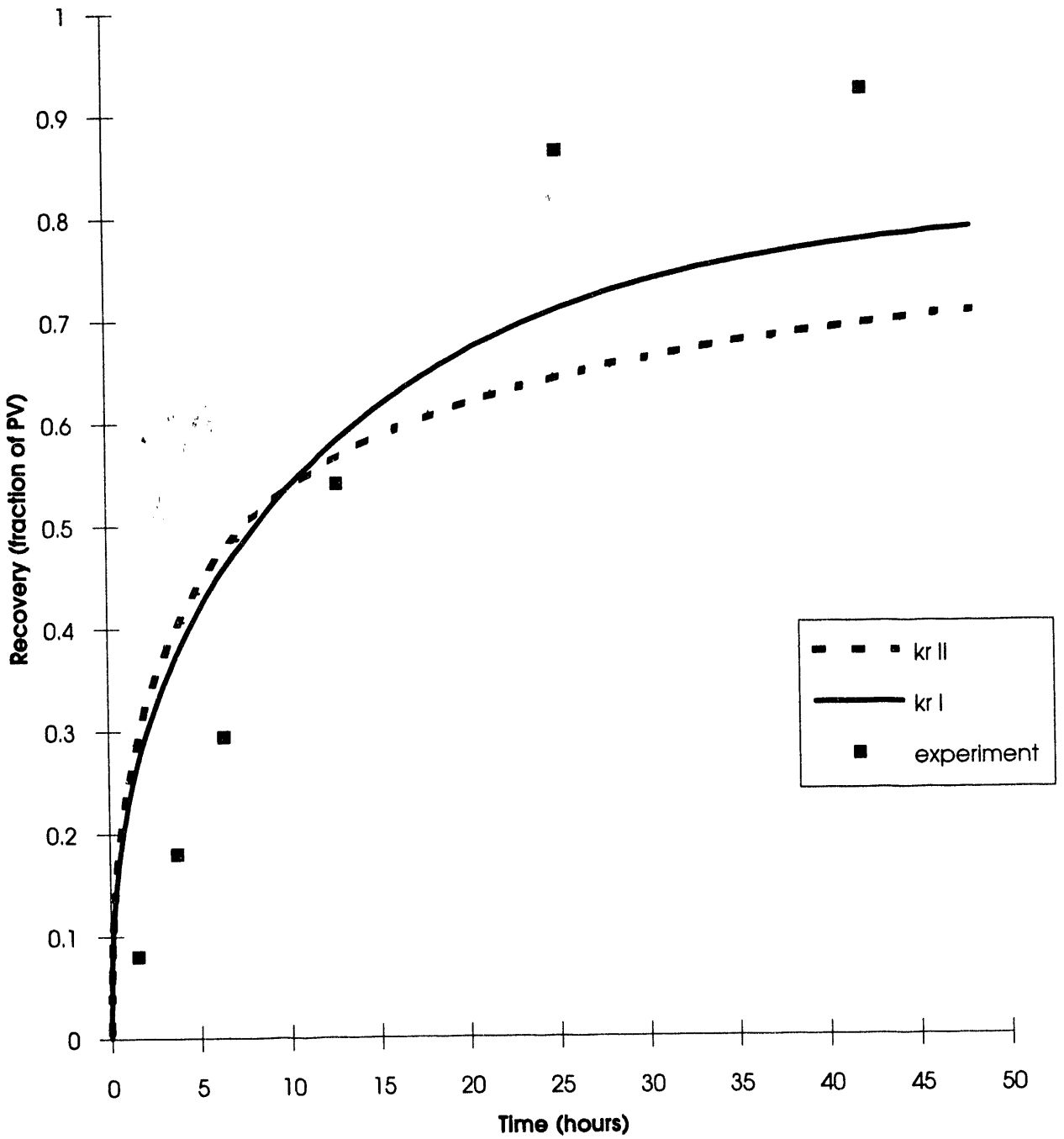

Figure 5.8: Comparison of simulation and experiment for low IFT imbibition.

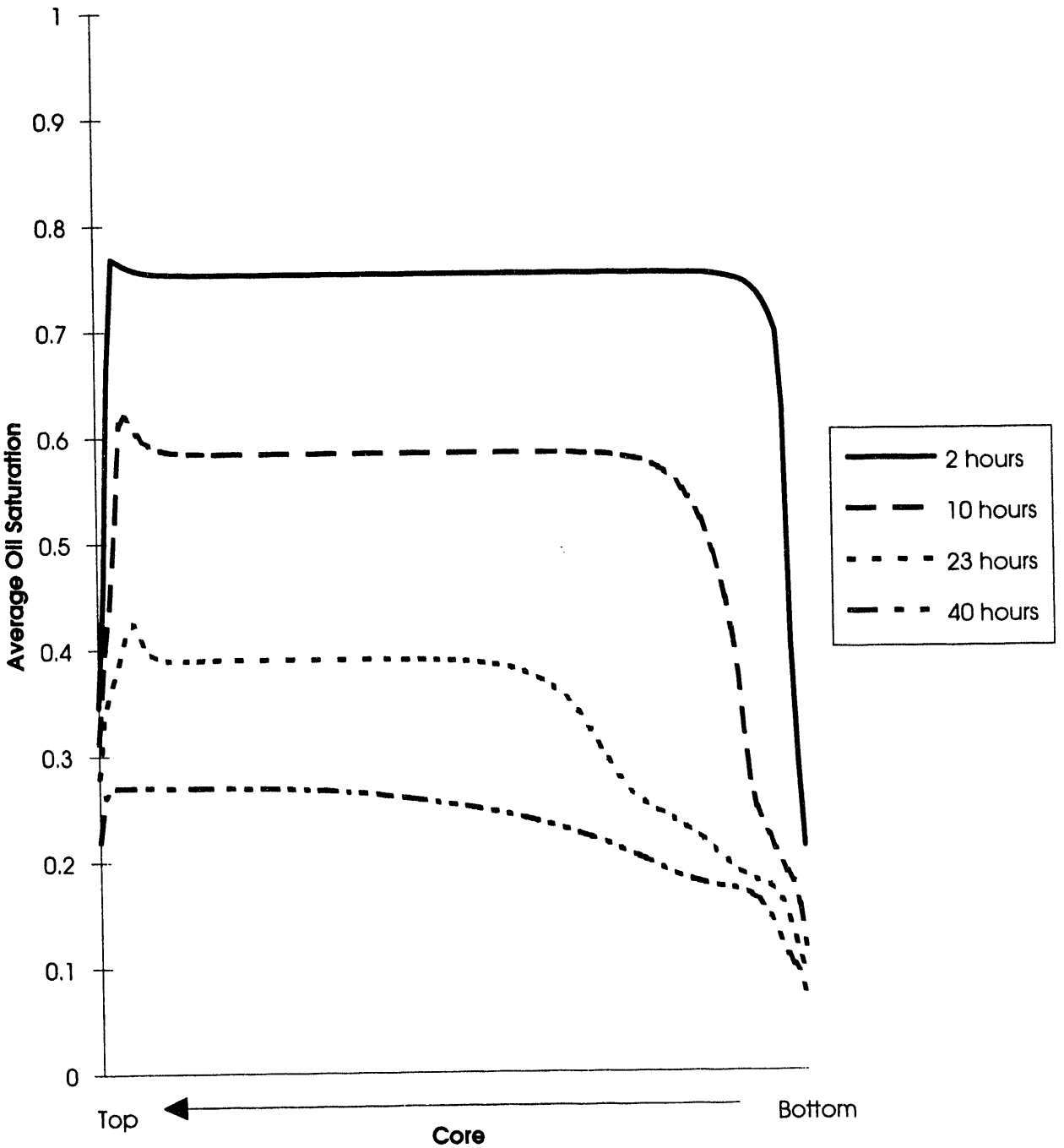

Figure 5.9: Oil saturation profiles during low IFT imbibition.

Imbibition Rates

The results of the imbibition experiments reported by Schechter *et al.* [61] include two important observations that require explanation. The first observation is that the recovery of the nonwetting-phase occurred more rapidly for the lower IFT displacements for all but the lowest permeability core. Faster recovery for the lower IFT's is a counterintuitive result, since the overall driving forces for imbibition decrease as the IFT is reduced. The second observation is that the total recovery exhibits a dramatic increase for all the cores for the low IFT case. Increased recovery efficiency indicates that snap-off of residual oil is suppressed.

The recovery rate is governed by the magnitude of the driving forces and the conductivity of the fluids. When N_B^{-1} is high, imbibition is dominated by capillary forces. Water will imbibe into all faces of the core, inducing countercurrent flow. Countercurrent flow is quite evident in the high IFT simulations. Countercurrent flow exhibits very low relative permeabilities [8], which are again quite evident in the high IFT simulations. Thus the imbibition rate is determined by a competition between very high-driving forces and extremely low fluid permeabilities.

As N_B^{-1} is reduced by lowering the IFT, gravity forces become more important. When the IFT is completely eliminated, cocurrent plug flow occurs. For the low IFT case, gravity exerts a high enough influence to segregate the fluids, resulting in cocurrent flow and higher relative permeabilities. The simulations also indicate a significant capillary driving force, which assists in the rate of recovery. The importance of this radial flow component becomes apparent when time scales for the different recovery processes are considered. Note that water relative permeabilities, although higher than those for the high IFT case, are still quite small at lower water saturations. This factor will be discussed further.

For intermediate value of N_B^{-1} where simulations were not performed, an increased role of capillary imbibition should be expected, and the oil profile would tend to be more uniform. Much like the low IFT case, the gravitational forces cause some segregation of the flow, which keeps the relative permeabilities high, and the capillary forces are strong enough to cause the recovery rate to be greater than the rate for high N_B^{-1}.

A time scale analysis supports the arguments given above. By comparing the ratio of the characteristic time for recovery by gravity-driven cocurrent vertical flow

$$t_g = \frac{H\phi}{\Delta\rho g \lambda^*} \tag{5.1}$$

to that for radial countercurrent capillary imbibition,

$$t_c = \frac{R^2\phi}{C\sigma\lambda^*}\sqrt{\frac{k}{\phi}} \tag{5.2}$$

the key parameters concerning the recovery rate become evident.

$$\frac{t_g}{t_c} = N_A \hat{N}_B^{-1} \frac{k^*_{rc}}{k^*_{rg}}, \qquad \hat{N}_B^{-1} = C\frac{\sigma_h\sqrt{\frac{\phi}{k}}}{\Delta\rho_l g H} \tag{5.3}$$

N_A is the aspect ratio H^2/R^2, where H is the height of the core and R is the radius of the core. $\hat{N}_B^{-1}$ represents a type of pseudo inverse Bond number, with the high IFT value in the numerator and the low IFT value for density difference in the denominator. σ_h and $\Delta\rho_l$ are the high IFT and the density difference at low IFT. The relative permeabilities k^*_{rg} and k^*_{rc} are the characteristic relative permeabilites for the gravity-dominated and capillary-dominated experiments respectively. Comparison of the times for half total recovery for the high IFT and low IFT cases yields an estimate of the ratio of the characteristic relative permeabilities. N_A is around 350, and $\hat{N}_B^{-1}$ equals 14.9.

For the 500 md Berea core the half-time ratio for recovery is approximately one, which results in $k^*_{rc}/k^*_{rg} = 2 \times 10^{-4}$. This number should compare favorably with those found in the simulations for the low IFT and high IFT case. The water relative permeability is the controlling factor in these imbibition experiments, so comparing these values at 30%, a value suitably away from the extremes of the curves, the ratio $k_{rwc}/k_{rwg} \approx 1 \times 10^{-3}$. Thus, the ratios differ by one order of magnitude. The discrepancy should not be too surprising, because the calculation for t_g assumes that the flow is strictly vertical, whereas Fig. 5.9 shows that there is a significant radial contribution to flow.

Imbibition Recovery Efficiency

As previously mentioned, displacements at low IFT showed a much higher recovery efficiency than the high IFT experiments. Significant evidence that supports this result. Morrow and Songkran [46] and Cuiec *et al.* [16] both found better recovery efficiency as IFT was reduced. However, what was not expected was the almost 100% recovery of the oil at the low IFT value. The reason behind this result lies in the fundamental mechanism that creates residual nonwetting-phase saturations. Roof [57] analyzed the quasi-static advance of a gas bubble through a toroidal pore. As the gas passes through a pore constriction and into the diverging part of the pore, the gas/water interfacial curvature changes. Since the gas-phase pressure is assumed to be constant, the pressure in the water must vary to reflect the changing curvature. Eventually, when the gas bubble reaches a certain radius in the diverging part of the core, the interfacial curvature at the front of the bubble becomes small enough such that the water at the front of the bubble has a higher pressure than the water in the pore constriction. This pressure gradient induces water to flow to the constriction, where it accumulates, forms a collar, and snap-off occurs.

However, Roof found that snap-off was extremely slow in experiments done with smooth pores. The presumption was that the rate of accumulation of water at the pore constriction was limited by the rate of transport of water through the thin films lining the pore walls. When a groove was sawed into the pores, collars were found to form more quickly, and snap-off was observed. Mohanty et al. [44] argued that pressure communication in the wetting-phase through roughness in the pore structure is required for collars to form. Lenormand and Zarcone [40] showed that wetting-phase flow through roughness and corners was necessary for snap-off of the nonwetting-phase in imbibition to occur. Thus, there is support for the idea that transport of wetting-phase in the capillary grooves in the rough surfaces is an essential part of the snap-off process that leads to the formation of a residual nonwetting-phase saturation.

For the particular case of the imbibition experiments in Schechter *et al.* [61], the rough surfaces on grains and the capillary grooves between grains are of even greater importance than the consideration of snap-off. Because the experiments were performed without an initial water saturation in the core, roughness and corners in the porous medium also provide the conduit for the introduction of the wetting phase into the rock. There is apparently high resistance associated with the flow of these thin wetting-phase films around the sand grains. The high resistance is evident in the water relative permeabilities required in the simulations at low wetting-phase saturations. Note that despite the very low relative permeabilities the early time recovery rate in the simulations was still significantly faster than the experimental recovery rate. Thus the displacement process becomes a competition between the flow through roughness of thin water films and bulk flow driven by gravity and pore scale interfacial curvature. When the IFT is high, the driving force for flow through roughness overcomes the high resistance to flow. Water can then accumulate at pore constrictions and snap-off can occur. When the IFT is low, flow through roughness is inhibited. Gravitational forces then act to displace the nonwetting-phase before snap-off can occur. Thus, the formation of residual nonwetting-phase saturation is controlled by the time scales for flow by gravity and flow in roughness. The numerical simulator is incapable of accounting for these pore

scale events such as flow through roughness that occur in primary imbibition. This may help to explain the difficulty in simulating primary imbibition shown in this report and in Kazemi and Merrill [37].

This argument is reinforced by an experiment performed on the 500 md Berea core that contained 19% initial water saturation. Fig. 5.10 shows the results of this experiment and a subsequent simulation. The residual oil saturation for this experiment is 55%, much higher than the experiment performed with no water in the core initially. Clearly, when the wetting-phase was present initially in the roughness and corners of the pore structure, the resistance to flow of the wetting-phase through the roughness decreased, allowing the wetting phase to accumulate in the pore constrictions and snap-off the nonwetting-phase. A plot of the average oil saturation versus time in Fig. 5.11 shows a larger degree of radial countercurrent imbibition than the case with no initial water in the core. Thus, the IFT is not low enough for the gravitational forces to become significant when the wetting-phase is initially present in the core. Still lower IFT's are apparently required to suppress snap-off and induce gravity-dominated cocurrent flow when an initial wetting-phase saturation is present.

5.1.3 Conclusions

1. Primary imbibition experiments are particularly difficult to simulate because current models do not account for the effects of flow through roughness.

2. Simulation shows that the high IFT experiments were dominated by radial, countercurrent imbibition.

3. Countercurrent imbibition wetting-phase relative permeabilities are very small for the experiments of Schechter *et al.* [61].

4. The low IFT simulations demonstrated a combination of radial, capillary-driven and vertical, gravity-driven imbibition. This argument was reinforced by examining the ratio of time scales for imbibition.

5. Snap-off was inhibited in the experiments by the lack of initial water saturation in the cores. When the low IFT experiment was repeated with 19% water in the core, snap-off increased dramatically, and the recovery was greatly reduced.

5.2 Scaling Multiphase Flow in Simple Heterogenous Porous Media

D. Zhou, F. J. Fayers, and F. M. Orr, Jr.

5.2.1 Introduction

In this work, we examine the scaling laws and flow regions controlling various types of flow behavior in systems with simple forms of heterogeneity. If we imagine displacement of oil by water in a two-dimensional, vertical cross-section of two layers with differing permeability, the distribution of oil and water at any time during the displacement will be controlled by a combination of physical phenomena. Water will usually flow faster in the high permeability layer. If the water is less viscous than the oil, then viscous fingering may influence the flow pattern. Gravity segregation will induce vertical flow, with very different effects depending on whether the high permeability layer is above or below the low permeability layer. Capillary forces will also cause transverse flow or crossflow, as

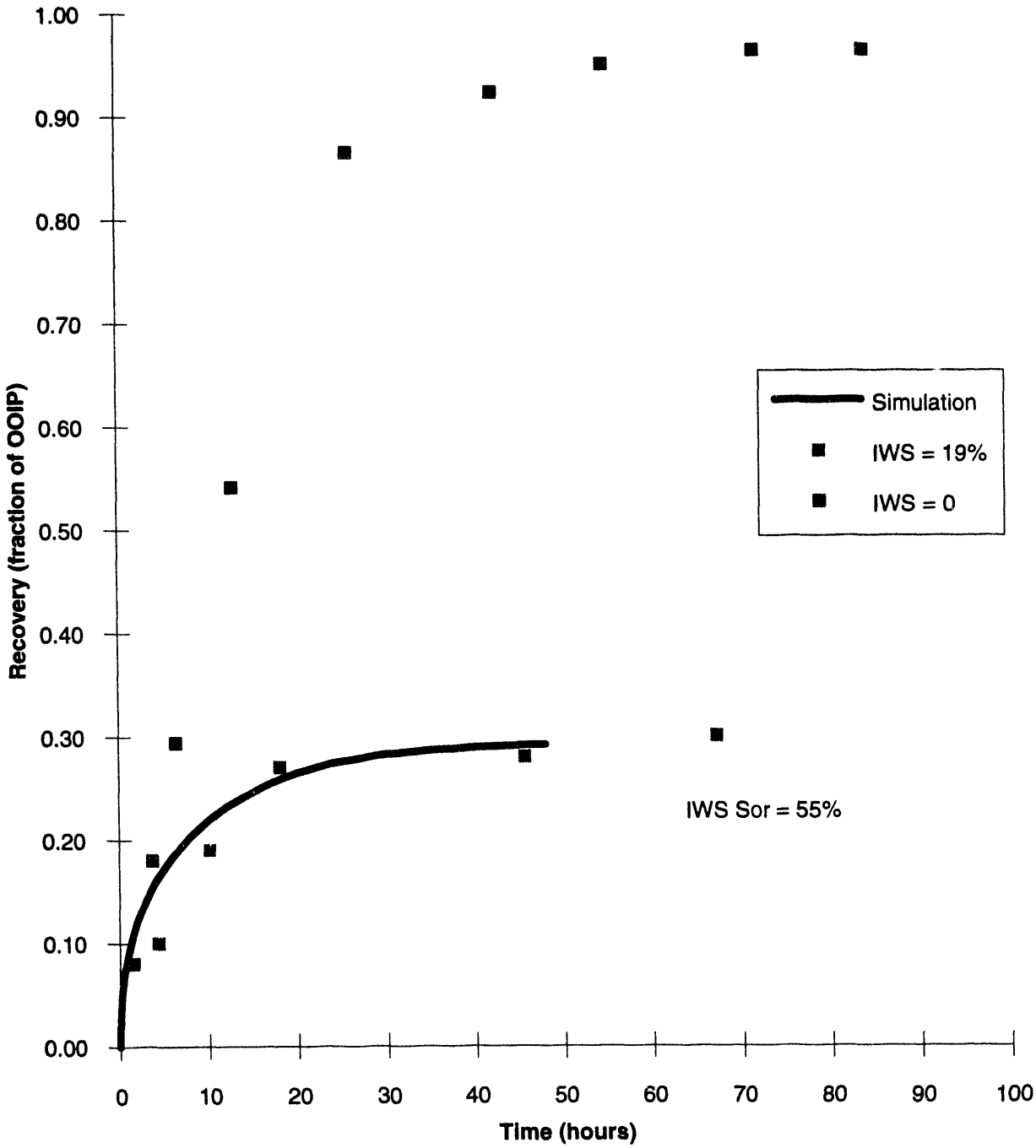

Figure 5.10: Comparison of simulation and experiments performed with and without initial water saturation (IWS) in the core.

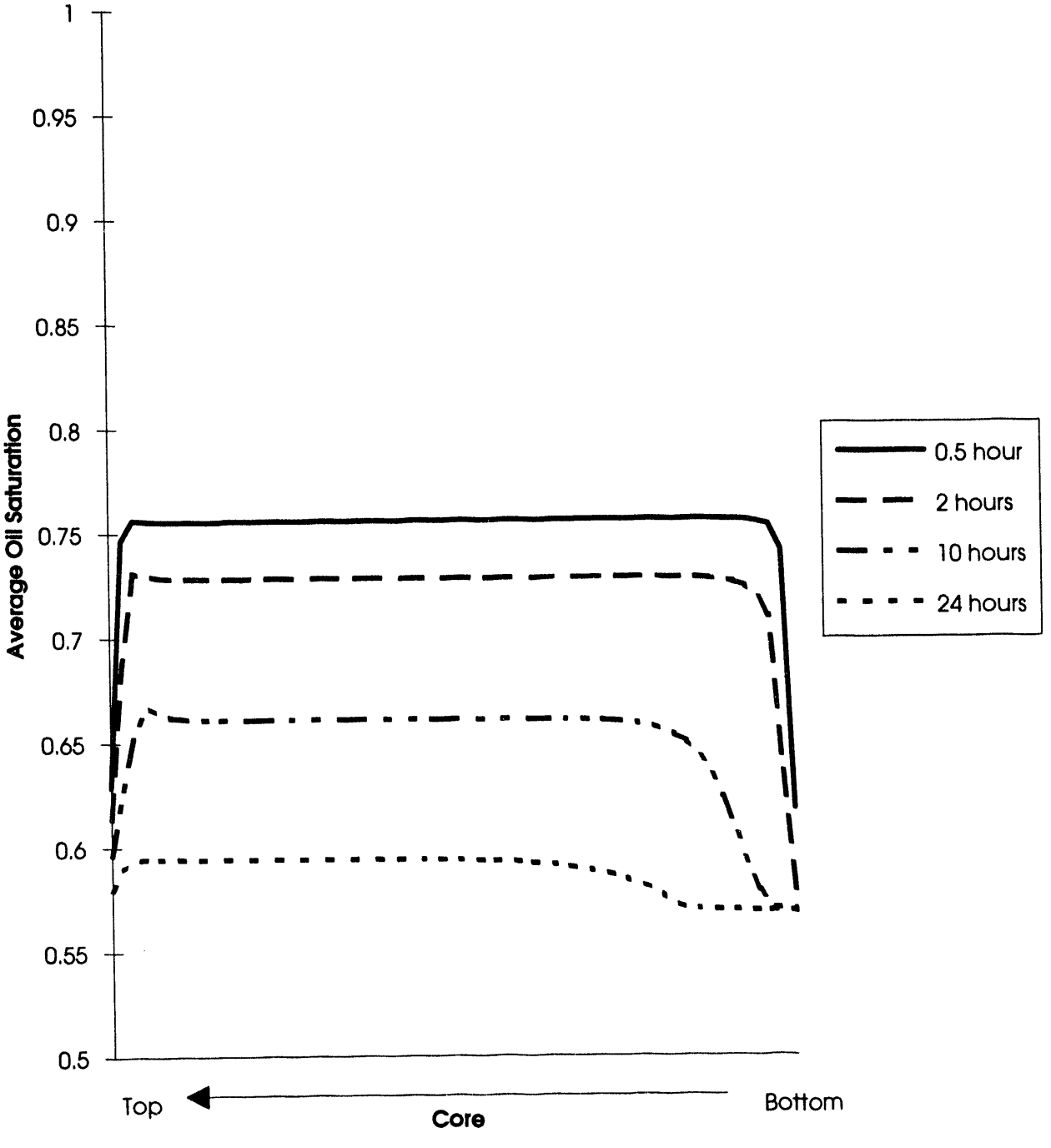

Figure 5.11: Oil saturation profiles during simulations of initial water saturation imbibition experiments.

water imbibes from the high permeability layer into adjacent low permeability zones (in a water-wet porous medium). The relative importance of each flow mechanism depends on the flow rate, the density difference between oil and water, the mobility ratio, permeabilities and capillary pressure curves for the layers, and so on. At low flow rate, for example, capillary and gravity forces will dominate the flow pattern, but at high flow rate, viscous forces will control fluid distributions.

We consider scaling of viscous, gravity, and capillary forces for displacements in homogeneous porous media and in systems that contain some simple heterogeneity such as layers and fractures. We do so by making the material balance equation dimensionless, thereby deriving a set of dimensionless groups that describe the relative magnitudes of the various forces. While many investigators [62, 72, 21, 55, 25] have used the same approach for subsets of the flow problems examined here, there has not previously been a comprehensive analysis which attempts to include a wide range of experimental data covering the combined effects of viscous, gravity, and capillary forces with the effects of permeability variation. We have analyzed many sources of experimental and simulation data to identify limiting flow regimes and to establish the range of values of the dimensionless groups over which transitions from one region to another occur. We find that the experimental information confirms consistent boundaries for the flow domains, and thus our results give a comprehensive mapping of the overall flow behavior.

The analysis and delineation of dimensionless transition regions given here will find a variety of applications. It will establish when concepts such as "vertical equilibrium" can be used to calculate average transport functions (pseudofunctions), and it will help to determine how much resolution is required in description of permeability heterogeneity in a reservoir. For example, if capillary pressure dominates local flow, then capillary crossflow will eliminate the effects of local permeability heterogeneity variations as capillary forces move water from high permeability to low-permeability zones. In such cases, the details of the local variations need not to be resolved in simulation representations of the flow. Thus, this analysis given here will permit more effective use of approximate simulation techniques that are an inevitable part of current simulation approaches for field-scale flows.

5.2.2 Analysis

For two-phase flow in a heterogeneous two-dimensional cross-section, we commence by expressing the equations of motion in a dimensionless form similar to that adopted by Yortsos [72] and Ekrann [21]. This form of analysis is referred to as Inspectional Analysis by Shook *et al.* [62]. While the approach we use is similar, the dimensionless groups we will define differ from those obtained by Shook *et al.* [62]. Material balance equations for incompressible flow are

$$\phi\frac{\partial S_w}{\partial T} + \frac{\partial U_w}{\partial X} + \frac{\partial V_w}{\partial Y} = 0, \tag{5.4}$$

$$\frac{\partial}{\partial X}(U_w + U_o) + \frac{\partial}{\partial Y}(V_w + V_o) = 0, \tag{5.5}$$

and the Darcy flow velocities for both phases are given by

$$U_j = -k_h(X,Y)\frac{k_{rj}}{\mu_j}\frac{\partial \Psi_j}{\partial X}, \tag{5.6}$$

$$V_j = -k_v(X,Y)\frac{k_{rj}}{\mu_j}\frac{\partial \Psi_j}{\partial Y}, \tag{5.7}$$

where Ψ_j is the flow potential in phase j, U_j and V_j are the flow velocities of phase j in the horizontal and vertical directions, and k_v and k_h are the permeability distribution functions in the vertical

and horizontal directions. By defining $x = X/L$, $y = Y/H$, $t = Tq/L$, $u_j = U_j/q$, $v_j = (LV_j)/(qH)$, $k_v = k_{av}K_V(x,y)$, $k_h = k_{ah}K_H(x,y)$, $\Phi_j = (\Psi_j k_{ah})/(Lq\mu_o)$, and $\lambda_j = (k_{rj}\mu_o)/\mu_j$, we obtain the following dimensionless equations

$$\phi\frac{\partial S_w}{\partial t} + \frac{\partial u_w}{\partial x} + \frac{\partial v_w}{\partial y} = 0, \tag{5.8}$$

$$\frac{\partial}{\partial x}(u_w + u_o) + \frac{\partial}{\partial y}(v_w + v_o) = 0, \tag{5.9}$$

$$u_j = -K_H(x,y)\lambda_j\frac{\partial \Phi_j}{\partial x}, \tag{5.10}$$

$$\left(\frac{H}{L}\right)^2\frac{k_{ah}}{k_{av}}v_j = -K_V(x,y)\lambda_j\frac{\partial \Phi_j}{\partial y}, \tag{5.11}$$

where H and L are the width and length of the medium, k_{av} and k_{ah} are the average permeabilities of the medium in vertical and horizontal directions, and q is the total flow velocity in the horizontal direction. Note that the flow potentials Φ_o are dimensionless and expressed relative to the oil viscosity, and that the dimensionless mobilities also contain oil viscosity as a factor.

In the four dimensionless equations, $(L/H)^2(k_{av}/k_{ah}) = {R_l}^2$ appears in Eq. 5.11 as the only scaling group, which can be rearranged as

$$\left(\frac{L}{H}\right)^2\frac{k_{av}}{k_{ah}} = \frac{L}{H}\frac{\frac{k_{av}\Delta\Phi}{H\mu}}{\frac{k_{ah}\Delta\Phi}{L\mu}} = \frac{L}{H}\frac{q_v}{q_h} = \frac{T_h}{T_v}, \tag{5.12}$$

which is the time ratio for a fluid to flow a distance (L) in the horizontal direction to the distance (H) in the vertical direction with the same potential difference across the distance. R_l is also called the effective shape factor, which is the shape factor L/H weighted by the permeability anisotropy. The shape factor (${R_l}^2$) represents the relative flow capacities of the medium in vertical and horizontal directions.

In this work, our objective is to identify flow regions where certain forces dominate fluid movement in the transverse direction. Thus, we will focus our attention on the flow velocity in the transverse direction. Combining the Darcy equations for each phase gives

$$\frac{1}{(R_l)^2}(v_w + v_o) = -K_V(x,y)\left(\lambda_o\frac{\partial \Phi_o}{\partial y} + \lambda_w\frac{\partial \Phi_w}{\partial y}\right). \tag{5.13}$$

In order to define the relation between Φ_o and Φ_w, we use the definition of capillary pressure to obtain

$$\Phi_w = \Phi_o + \frac{\Delta\rho g H k_{ah}}{Lq\mu_o}y - \frac{{p_c}^* k_{ah}}{Lq\mu_o}J(S_w), \tag{5.14}$$

where transverse capillary pressure is defined as $p_c = {p_c}^* J(S_w)$, and ${p_c}^*$ is a characteristic transverse capillary pressure of the medium, ${p_c}^* = \int_{S_{wc}}^{1-S_{or}} p_c(S_w)dS/(1 - S_{or} - S_{wc})$. Substituting Eq. 5.14 into Eq. 5.13 yields

$${R_l}^2\frac{\partial \Phi_o}{\partial y} = \frac{-(v_o + v_w)}{\lambda_o K_V(x,y)(1+M)} - \frac{M}{1+M}\left(N_{gv} - N_{cv}\frac{\partial J}{\partial y}\right), \tag{5.15}$$

where

$$N_{gv} = \frac{\Delta\rho g L k_{av}}{Hq\mu_o}, \tag{5.16}$$

$$N_{cv} = \frac{L{p_c}^* k_{av}}{H^2 q\mu_o}, \tag{5.17}$$

and

$$M = \frac{\lambda_w}{\lambda_o}. \tag{5.18}$$

N_{gv} and N_{cv} are the characteristic time ratios for fluid to flow in the transverse direction due to gravity or capillary forces to that in horizontal direction due to viscous forces as shown by Eqs. 5.19 and 5.20.

$$N_{gv} = \frac{\Delta\rho g L k_{av}}{H q \mu_o} = \frac{L}{q}\frac{\frac{\Delta\rho g k_{av}}{\mu_o}}{H} = \frac{T_h}{T_{gv}}, \tag{5.19}$$

and

$$N_{cv} = \frac{L p_c^* k_{av}}{H^2 q \mu_o} = \frac{L}{q}\frac{\frac{p_c^* k_{av}}{H \mu_o}}{H} = \frac{T_h}{T_{cv}}. \tag{5.20}$$

Note the differences of the gravity and capillary numbers defined here from the conventional gravity (N_g) and capillary (N_c) numbers in the past studies [62, 72, 3], except Fayers and Muggeridge [27] used N_{gv}, and Yokoyama and Lake [71] used N_{cv} in their studies. The conventional capillary (N_c) and gravity (N_g) numbers are defined and related to the new numbers as

$$N_g = \frac{\Delta\rho g H k_{ah}}{L q \mu_o} = \frac{N_{gv}}{{R_l}^2}, \tag{5.21}$$

and

$$N_c = \frac{p_c^* k_{ah}}{L q \mu_o} = \frac{N_{cv}}{{R_l}^2}. \tag{5.22}$$

The advantage of using N_{gv} and N_{cv} is that they represent the relative magnitudes of the gravity and capillary forces to the viscous forces in the transverse direction including the fact of aspect ratio as reflected by the shape factor (${R_l}^2$).

We will treat $M/(1+M)$ as a constant in the system, although in principle, the mobility ratio M is a function of saturation. For a number of the applications to be considered, we will be concerned with crossflow mechanisms in vertical sections for which the boundary conditions are $v_o = v_w = 0$ at top and bottom. We therefore expect that v_o and v_w will be relatively small at intermediate locations.

Eq. 5.15 shows that the potential gradient in the vertical direction of a cross-section consists of three parts: viscous, gravity and capillary forces. The relative magnitudes of these forces are defined by two dimensionless numbers: a modified gravity number $(N_{gv}M)/(1+M)$, and a modified capillary number $(N_{cv}M)/(1+M)$. Thus, the mobility ratio has been included in the capillary and gravity numbers, because the definitions of capillary and gravity numbers are based only on oil viscosity. The shape factor (${R_l}^2$) defines the magnitude of the potential gradient of the system in the transverse direction. In addition to the three scaling numbers, the scaled permeability distribution function $K_V(x,y)$ and scaled capillary pressure function $J(S_w)$ represent the effects of heterogeneity of the medium. $\partial S_w/\partial y$ shows the influence of the phase distribution in the medium.

The scaling properties of a heterogeneous medium can be categorized as the average scaling parameters, such as the shape factor ${R_l}^2$, capillary number $(MN_{cv})/(1+M)$, gravity number $(MN_{gv})/(1+M)$, and the mobility ratio M, and the detailed scaling properties as the scaled permeability distribution function $K_V(x,y)$, capillary pressure function $J(S_w)$, and phase distribution $\partial S_w/\partial y$. This work will examine the average scaling parameters to identify flow regions where certain forces dominate. We will consider media having simple heterogeneity, but will assume that the effects of ordering of layers is secondary to the principal mechanisms controlling the flows. In the following, we will define conditions for four flow regions: gravity-dominated, capillary-dominated, capillary-gravity equilibrium, and viscous-dominated flow regions. In each case, the vertical potential gradient given in Eq. 5.15 is used to obtain limiting conditions for the crossflow behavior. The limiting forms of expression for vertical potential gradients to be derived in the next section are summarized in Table 5.1.

Table 5.1: Summary of the limiting cases

Flow region	Simplified expression	Conditions
Capillary-dominated	$R_l{}^2\frac{\partial\Phi_o}{\partial y} = \frac{MN_{gv}}{1+M}\frac{\partial J}{\partial y}$	$N_{cv} >> N_{gv}$ and $\frac{MN_{cv}}{1+M} >> 1.0$
Gravity-dominated	$R_l{}^2\frac{\partial\Phi_o}{\partial y} = -\frac{MN_{gv}}{1+M}$	$N_{gv} >> N_{cv}$ and $\frac{MN_{gv}}{1+M} >> 1.0$
Capillary-gravity equil.	$\frac{\partial J}{\partial S}\frac{\partial S}{\partial y} = -\frac{\Delta\rho g H}{p_c{}^*}$	$N_{gv} \approx N_{cv}$ and $\frac{MN_{gv}}{1+M} >> 1.0$
Viscous-dominated	$R_l{}^2\frac{\partial\Phi_o}{\partial y} = \frac{1}{(1+M)}\frac{v_o+v_w}{\lambda_o K_V(x,y)}$	$\frac{(N_{gv}+N_{cv})M}{1+M} << 1.0$
Vertical crossflow equil.	$\frac{\partial\Phi_o}{\partial y} \approx 0$	$\frac{(N_{gv}+N_{cv})M}{1+M} << 1.0$ and $R_l{}^2 >> 1.0$
No-communication	$\frac{\partial\Phi_o}{\partial y} \approx \infty$	$\frac{(N_{gv}+N_{cv})M}{1+M} << 1.0$ and $R_l{}^2 << 1.0$

Gravity-Dominated Crossflow

Gravity-dominated flow occurs if $N_{gv} >> N_{cv}$, so that Eq. 5.15 can be reduced to

$$R_l{}^2\frac{\partial\Phi_o}{\partial y} = \frac{-(v_o+v_w)}{\lambda_o K_V(x,y)(1+M)} - \frac{MN_{gv}}{1+M}. \tag{5.23}$$

Furthermore, if $(N_{gv}M)/(1+M) >> F_{vis}$, Eq. 5.23 can then be reduced to

$$R_l{}^2\frac{\partial\Phi_o}{\partial y} = -\frac{MN_{gv}}{1+M}. \tag{5.24}$$

where $F_{vis} = -(v_w+v_o)/(\lambda_o(1+M)K_V(x,y))$. F_{vis} should be small and in the magnitude of unity for this case. Thus, the conditions for Eq. 5.24 to be valid are that $N_{gv} >> N_{cv}$ and $MN_{gv}/(1+M) >> 1.0$. Eq. 5.24 has been derived such that the system is dominated by gravity segregation.

Capillary-Dominated Crossflow

If capillary effects dominate, then Eq. 5.15 reduces, when $N_{cv} >> N_{gv}$ to

$$R_l{}^2\frac{\partial\Phi_o}{\partial y} = \frac{-(v_o+v_w)}{\lambda_o K_V(x,y)(1+M)} + \frac{M}{1+M}N_{cv}\frac{\partial J}{\partial y}. \tag{5.25}$$

When $(N_{cv}M)/(1+M) >> 1.0$, Eq. 5.25 simplifies to

$$R_l{}^2\frac{\partial\Phi_o}{\partial y} = \frac{MN_{cv}}{1+M}\frac{\partial J}{\partial y}, \tag{5.26}$$

Thus, the driving force for fluid to flow in the transverse direction is the capillary force. The conditions for such a case are that $(N_{cv}M)/(1+M) >> 1.0$ and $N_{cv} >> N_{gv}$.

Capillary-Gravity Equilibrium

If $(N_{gv}M)/(1+M) >> 1.0$, Eq. 5.15 can be reduced to

$$R_l{}^2\frac{\partial\Phi_o}{\partial y} = \frac{MN_{gv}}{1+M}\left(1 - \frac{N_{cv}}{N_{gv}}\frac{\partial J}{\partial y}\right). \tag{5.27}$$

If $(MN_{gv})/(1+M) >> 1.0$, and $N_B = N_{gv}/N_{cv}$ is intermediate, the value of $(1-(N_{cv}/N_{gr})(\partial J/\partial y))$ should be small, which means that

$$\frac{\partial J}{\partial S}\frac{\partial S}{\partial y} \approx \frac{N_{gv}}{N_{cv}} = \frac{\Delta \rho g}{p_c^*}. \tag{5.28}$$

Eq. 5.28 indicates that the system is in capillary-gravity equilibrium. Thus, if $(N_{gv}M)/(1+M) >> 1.0$ and N_{gv}/N_{cv} is moderate, the system can be considered to be in capillary-gravity equilibrium.

Viscous-Dominated Crossflow

In Eq. 5.15, the net effects of capillary and gravity forces are controlled by the sign of $\partial S_w/\partial y$. Since $\partial J/\partial S_w$ is negative, if $\partial S_w/\partial y$ is negative, the gravity and capillary forces tend to offset each other's effects. However, they will enhance each other's effects if $\partial S_w/\partial y$ is positive. In order to reach a viscous-dominated flow region, the viscous force should be much greater than the maximum effects of capillary and gravity forces, that is

$$(1 + \frac{N_{cv}}{N_{gv}})\frac{N_{gv}M}{1+M} << 1.0. \tag{5.29}$$

Eq. 5.15 can then simplify to

$$R_l{}^2\frac{\partial \Phi_w}{\partial y} = R_l{}^2\frac{\partial \Phi_o}{\partial y} = \frac{-(v_w + v_o)}{\lambda_w K_V(x,y)}. \tag{5.30}$$

If $R_l{}^2 >> 1.0$, the value of $\partial \Phi_o/\partial y$ should be very small, because $F_{vis} = -(v_o + v_w)/(\lambda_o(1 + M)K_V(x,y))$ has a finite value. Thus,

$$\frac{\partial \Phi_o}{\partial y} \approx 0 \approx \frac{\partial \Phi_w}{\partial y}. \tag{5.31}$$

Crossflow under such condition is referred as viscous crossflow equilibrium (VCE). It is obvious that VCE is valid only if $(N_{gv}G + N_{cv})M/(1 + M) << 1.0$, and also $R_l{}^2 >> 1.0$.

Eq. 5.30 indicates that if the viscous forces dominate flow, both phases should crossflow in the same direction at any point of the medium. Furthermore, if $R_l{}^2 << 1.0$, $\partial \Phi_o/\partial y$ should be very large, that is,

$$\frac{\partial \Phi_o}{\partial y} = \frac{\partial \Phi_w}{\partial y} \rightarrow \infty. \tag{5.32}$$

Eq. 5.32 indicates that for finite crossflow velocites $(v_o + v_w)$ and $R_l{}^2 << 1.0$, there would need to be an infinitely large potential gradient. Since this is not plausible, there should be little crossflow in the transverse direction.

In summary, if $(N_{cv} + N_{gv})M/(1 + M) << 1.0$, the system is dominated by the viscous forces. At the same time, if $R_l{}^2 << 1.0$, viscous crossflow can be neglected, and if $R_l{}^2 >> 1.0$, the system is in VCE.

5.2.3 Discussion and Comparison with Existing Experimental and Simulation Results

Three independent dimensionless groups have been derived for the average scaling properties of a flow system:
$(N_{gv}M)/(1 + M)$, $(N_{cv}M)/(1 + M)$ and $R_l{}^2$. We then defined the conditions for certain forces

to dominate fluid flow in a medium. However, the conditions defined in the above section are mathematically infinitely small or large. In practice, we would ask, how large (or small) is large (or small) enough for these conditions to hold. To answer this question, we examined existing experimental and numerical simulation results to identify flow regions. In the following, we define a flow with a single gravity tongue as gravity-dominated flow, a flow which is faster in the low-permeable region than in high-permeable region as capillary-dominated, and a flow where recovery varies little with increase in flow rates as viscous-dominated.

Previous studies of scaling behavior in multiphase flow in porous media have usually concentrated on one of the following three situations: miscible displacements, immiscible displacements with minimal gravity effects, and flow in fractured reservoirs. Although the existing experimental and numerical simulation results for each case do not cover all parameters derived above, combining these three different situations gives us a reasonably clear picture of the flow regions in general. A summary of the principal sources of data and their estimated ranges of scaling parameters is given in Table 5.2.

Miscible Displacements($N_{cv} \approx 0$)

The term miscible displacement here refers to displacements with negligible capillary effects ($N_{cv} \approx 0$), which can also include two-phase flow. Much research effort has been applied to flow in such systems [3, 25, 9, 33]. When the capillary force is neglected, only gravity and viscous forces contribute to flow. Dispersion and diffusion can influence to some degree the performance of miscible and near-miscible displacements [23], since they affect mixing and the contrasts in viscosity and density differences. However, dispersion can usually only be a significant contributor in displacements where capillary and gravity forces are small and injection rates are also relatively small. Dispersion effects will not be included in this work, and we retain the unmixed viscosities and densities to analyze miscible scaling behavior.

Studies of crossflow in heterogeneous media have commonly been carried out on stratified media [50, 74, 75, 33]. The complexity of the problem has progressed from studying viscous crossflow alone [75, 74] to including gravity effects [21, 33]. Zapata and Lake's fine-grid simulation results on stratified reservoirs concluded that for systems without gravity and capillary effects, when $R_l{}^2$ was larger than 100, the viscous-crossflow equilibrium assumption was valid [75]. Continuation of their work by Thiele [66] showed that for practical purposes, if $R_l{}^2$ was larger than 10, the VCE assumption held, and if $R_l{}^2$ was smaller than 0.01, the system could be assumed to have no communication (vertical crossflow can be neglected).

Both experimental and numerical simulation results have been reported for gravity effects on displacement performance in vertical cross-sections [3, 25, 33]. Fayers and Muggeridge [25] performed very fine-grid simulations for homogeneous vertical cross-sections and found that the transition of viscous-dominated flow to gravity tonguing occurs in the range of $0.2 < (N_{gv}M)/(1 + M) < 2$. Pozzi's [55] experimental results for uniform bead-packs showed that a single-gravity tongue would form if $(N_{gv}M)/(1 + M) > 2.5$, which agrees well with Fayers and Muggeridge's simulation results. Araktingi and Orr's simulation results from a particle-tracking simulator for both homogeneous and stratified vertical cross-sections indicates that flow was viscous-dominated if $N_{gv}M/(1 + M) < 0.25$ [3], which also agrees very well with the above results.

Experimental results were reported by Insoy and Skjaeveland [33] to examine the theory by Ekrann for development of a gravity tongue in a stratified porous medium. Ekrann's theory assumed that vertical equilibrium and pressure continuity along the displacement front are the criteria for development of a single gravity tongue. The predicted critical value of a system for a single gravity tonguing is $(MN_{gv})/(1 + M) > 5.0$. Their experimental data showed that when $(MN_{gv})/(1 + M) = 11.5$, there was a gravity-stable tongue.

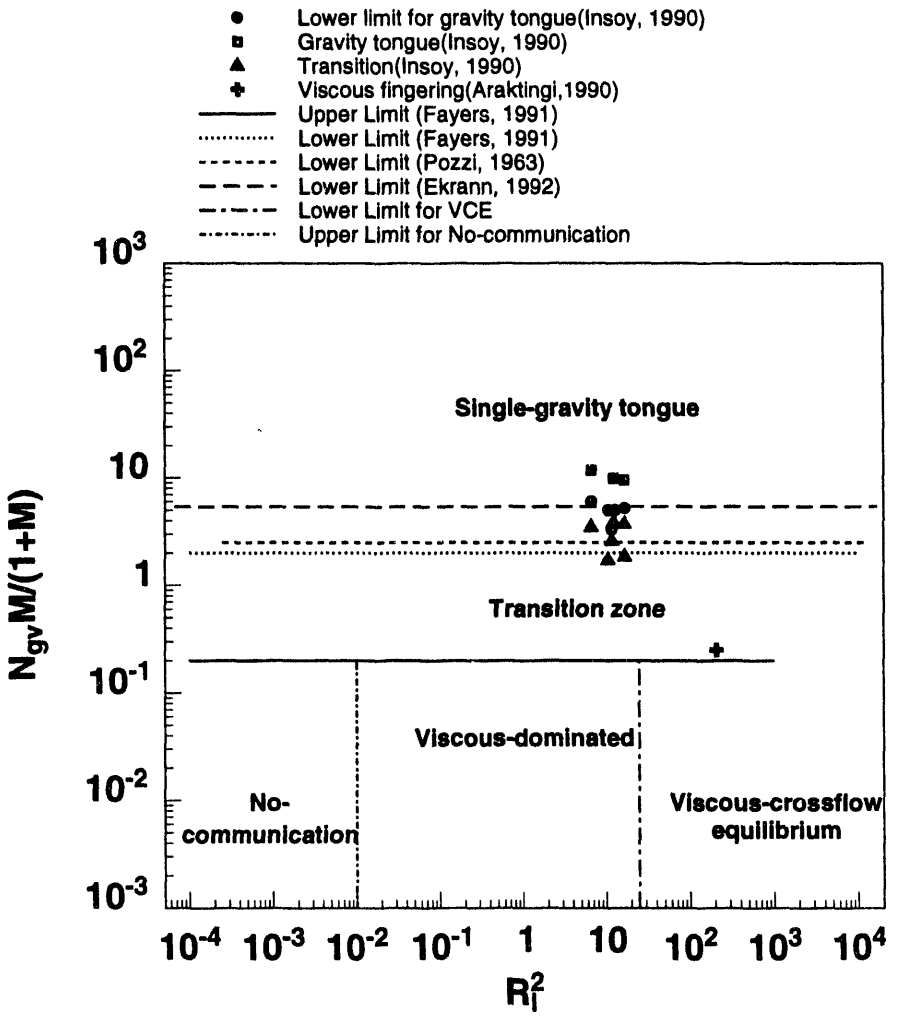

Figure 5.12: Flow regions in miscible displacements

Fig. 5.12 shows the flow regions in miscible displacements in layered and homogeneous media. The lines are the boundaries between flow regions reviewed in this section. Although the results are from both layered and homogeneous media, the transition from the gravity-dominated to the viscous-dominated region agrees well between investigators. The transition is in the range of $0.2 < (N_{gv}M)/(1+M) < 5.0$. In the viscous-dominated region, the boundaries of transition from no communication to VCE regions are based on Thiele's results. The transition in this case in the range of $0.01 < R_l{}^2 < 10$.

Immiscible Displacements without Gravity Effects ($N_{gv} \approx 0$)

Capillary-dominated crossflow has been demonstrated as an important oil recovery mechanism, and therefore it receives considerable attention in oil recovery research. Several studies were carried out to investigate capillary crossflow in the absence of gravity effects [22, 71, 18]. Yokoyama and Lake [71] simulated the effects of capillary pressure on displacements in stratified porous media. Their results show that with increased injection rate, less oil was recovered at the same pore volume injected [71]. They varied the transverse capillary number (N_{cv}) from 0 to 57.4. From their simulated fractional flow curves, we can see that at $N_{cv} = 0$, there was no crossflow between layers, while with increase of N_{cv}, more crossflow occurred from the high-permeable layer to the low-permeable layer. When $MN_{cv}/(1+M) = 4.1$, the displacement front in the stratified system was close to uniform. When $(MN_{cv})/(1+M) = 57.4$, the displacement front was completely

uniform, which indicated capillary-dominated flow.

An experimental study of capillary crossflow on a bead-pack by Ahmed *et al.* [1] showed that crossflow changed significantly with changes in injection rates, although the production curves did not vary so much. At their high injection rate ($MN_{cv}/(1+M) = 0.35$), a viscous flow regime existed in the most permeable layer, with breakthrough occurring in that layer. At low injection rate ($MN_{cv}/(1+M) = 8.5$), flow advanced faster in the low-permeability layer, which indicates a capillary-dominated flow. At intermediate flow rates ($(MN_{cv})/(1+M) = 0.57$), displacements occurred in both the high-permeability layer and the low-permeability layer.

In the waterfloods by Dawe *et al.* [18] in layered bead-pack systems at low rates, the water front in the low-permeability layer advanced faster than that in the high-permeability layer [18]. Thus, the displacements were capillary-dominated. The corresponding value for $(MN_{cv})/(1+M)$ varied from 13.1 to 105.

The studies discussed above were for imbibition processes. Pavone's study [53] of viscous fingering in carbonate porous media was for drainage processes, however. The physical parameters of the system were not well defined, although the author listed the permeabilities and porosities of the samples. In order to use Pavone's experimental results, the measured maximum pressures were used to estimate the capillary entry pressures and the viscous pressure drops for similar media. For each viscous ratio, media with reported permeability differences of no more than 0.1 Darcy were considered as similar media. The corresponding values of $(MN_{cv})/(1+M)$ can then be estimated for all displacements. From the moldings of the displacement fronts in the porous media, it can be seen that the displacement in RUN 9 is capillary-dominated, since it had a stable front with unfavorable mobility ratio. For RUN 9, $(MN_{cv})/(1+M) = 10$.

Combining the experimental and simulation data, we can approximately determine the transition region from capillary- to viscous-dominated flow as shown in Fig. 5.13. The lower limit for the capillary-dominated flow is the intermediate rate displacement of Yokoyama and Lake's simulations $MN_{cv}/(1+M) = 4.1$. The dashed line in Fig. 5.13 is the estimated lower limit for the capillary-dominated region. The upper limit (solid line) for the viscous-dominated region is drawn through the highest rate of Ahmed *et al.*'s experiments. In summary, the transition between capillary-dominated and viscous-dominated flow occurs in the range of $0.35 < N_{cv}\frac{M}{1+M} < 4.1$. Within the viscous-dominated flow regions (i.e. capillary and gravity forces are negligible), the no-communication and viscous crossflow equilibrium flow regimes should be the same as in the miscible displacement cases.

Flow in Fractured Reservoirs

In studies of flow in fractured reservoirs, imbibition or drainage cells are commonly used to simulate the behavior of oil recovery from reservoirs with vertical fractures [61, 16, 20]. In such cases, the flow in the horizontal direction is relatively small and the values for N_{cv} and N_{gv} become very large. Therefore, the ratio of the gravity to capillary forces ($N_B = N_{gv}/N_{cv}$) is an important parameter in scaling flow in fractured media. Thus, flow in vertically fractured reservoirs is a special case in using the scaling equation. The calculation of the Bond number (N_B) requires the value of capillary pressure. However, in some of the studies, capillary pressure curves are not available. In the following discussion, $p_c{}^*$ is taken to be the average threshold capillary pressure of the medium and is estimated by the following equation for cases without capillary pressure data:

$$p_c{}^* = 4\sigma\cos\theta\left(\frac{c\phi}{k}\right)^{1/2} \tag{5.33}$$

where c is a constant depending on the medium, $c = 0.02$ is used for glass bead-packs, θ is the contact angle depending on the wettability of the system. The glass bead-packs can be considered as strongly water-wet ($\cos\theta = 1$) .

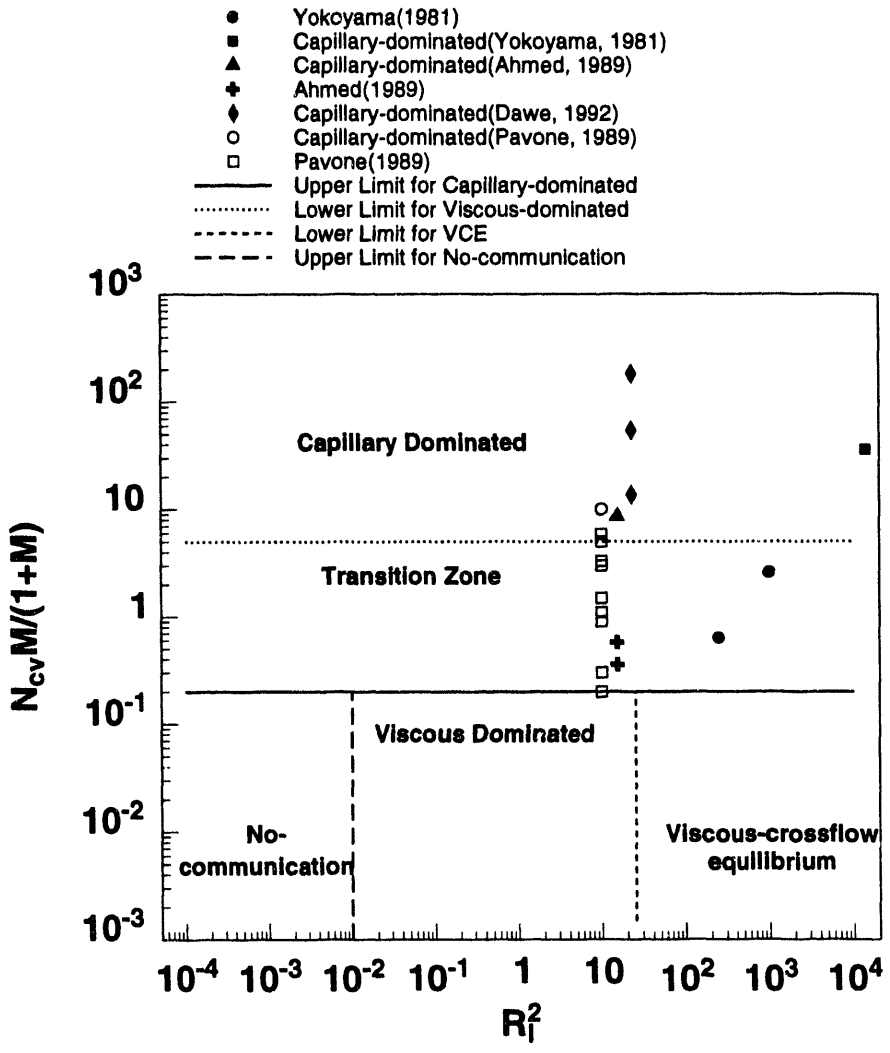

Figure 5.13: Flow regions in immiscible displacements

Early studies of imbibition were carried out on small reservoir samples and at high interfacial tension (IFT). Cuiec's results [16] for low-permeability chalks indicates that production curves could be scaled according to imbibition theory (i.e. capillary force is the driving force). The Bond numbers were small and varied from 10^{-4} to 10^{-2} in Cuiec's study. On the other hand, du Prey's centrifuge imbibition tests [20] for sandstone samples showed that production curves could not be successfully scaled with an imbibition model when the Bond number changed from 10^{-2} to 10. Careful examination of the production curves shows that they can be scaled well by imbibition theory if $N_B < 0.2$. Production curves with Bond numbers between 0.2 to 10 cannot be scaled by either capillary-dominated or gravity-dominated theory.

Schechter *et al.* [61] reported low IFT imbibition and drainage results, which showed that imbibition processes changed from capillary-dominated to gravity-dominated when IFT was changed from 38.1 mN/m to 0.1 mN/m. Their characteristic time scaling shows that if $N_B < 0.2$ the flow could be considered to be capillary-dominated, and if $N_B > 5$ the flow was gravity-dominated.

Imbibition studies by Iffly *et al.* [32] concluded that gravity influenced imbibition in the tests with the cylindrical sides sealed when the Bond number changed from 0.05 to 10^{-3}. This seems a contradiction to the results reviewed above. However, the characteristic length used in their scaling was based on countercurrent flow. The flows in the test could have been cocurrent flow. Thus, an explanation is that water imbibed in from the bottom of the media and oil flowed out from the top of the samples. Scaling of their results improves significantly with the characteristic length for

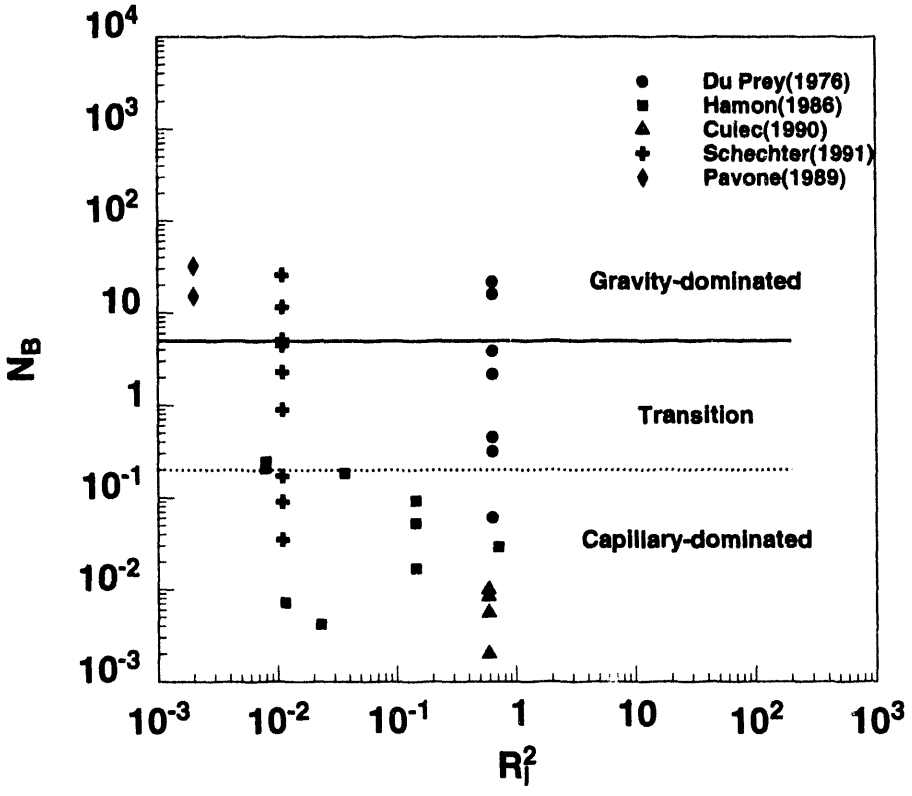

Figure 5.14: Flow regions in fractured reservoirs

cocurrent flow. The improvement suggests that the imbibition processes were capillary-dominated, but the flow was cocurrent.

Fig. 5.14 summarizes the experimental results reviewed in this section. Most of studies were focused on the capillary-dominated region with only the work by du Prey [20] and Schechter *et al.* [61] covering the transition region. The transition boundaries from the capillary-dominated to gravity-dominated regions are determined from Schechter *et al.*'s results, which are in the range of $(0.2 < N_B < 5)$.

Discussion

In previous sections, we have reviewed data from three types of situations: miscible displacements, immiscible displacements, and flow in fractured reservoirs. Although the data are limited, approximate bounds can be set up between flow regions for the media reviewed here. From miscible displacements, we find the transition between viscous-dominated to gravity-dominated is in the range of $0.2 < (MN_{gv})/(1+M) < 5.0$. Immiscible displacement results indicates the transition between viscous-dominated to capillary-dominated is in the range of $0.35 < (MN_{cv})/(1+M) < 4.1$, and the transition from capillary- to gravity-dominated flow in vertically fractured reservoirs is in the range of $0.2 < N_B < 5.0$. It is interesting to note that the transitions from capillary to gravity, from viscous to capillary, and from viscous to gravity flow regions occur in a similar range for the different scaling numbers. We can generalize the conditions for the transitions as: $0.2 < Sc < 5.0$, where Sc can be either $MN_{cv}/(1+M)$, or $MN_{gv}/(1+M)$, or N_B.

Fig. 5.15 shows the combined results of the flow regions for all three scaling numbers. The boundaries are determined based on the general results discussed above. In determining the viscous-dominated region with both gravity and capillary effects, we assume that $0.2 < (M(N_{cv} + N_{gv})/(1+M) < 5.0$. In the viscous-dominated region, the bounds of the transition from viscous

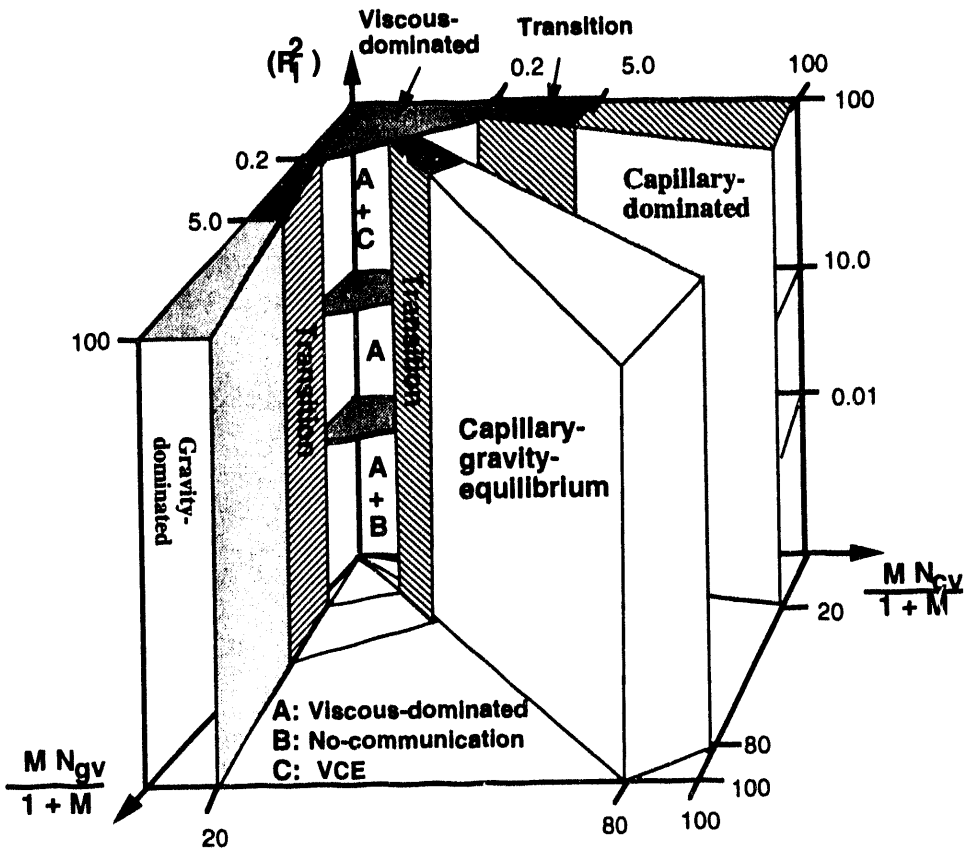

Figure 5.15: Schematic of flow regions in simple heterogeneous porous media

crossflow equilibrium to no-communication regions are based on Thiele's simulation results.

For slightly immiscible systems approaching a critical condition, the ratio $\Delta\rho/\sigma$ determined from critical scaling theory increases rapidly near the critical point, and thus the Bond number of the system can increase dramatically. Therefore, in systems approaching miscibility as injection pressure or solvent enrichment increases, gravity effects will dominate as the capillary forces are reduced. In such situations, simulation models of near-miscible processes must handle the phase behavior and the density difference with care if the interplay of capillary and gravity forces is to be modeled accurately.

Since there are difficulties in determining the capillary pressure and mobility ratio, the bounds set from this work for immiscible displacements may have relatively large uncertainty regarding to the Bond number and capillary numbers. Capillary pressure curves should be measured to obtain reliable scaling for reservoirs, using either the imbibition or drainage mode appropriate to the type of displacement. Further investigation is needed to be sure that the end-point mobility ratio used here is valid for immiscible displacements with unfavorable mobility ratio.

5.2.4 Conclusions

In this study, we have defined three important dimensionless numbers that govern fluid flow in porous media with simple heterogeneities, and we have established approximate bounds for the transitions between regions. The dimensionless numbers can be easily extended to specific flow systems as shown in the discussion section. A diagram of flow regions (Fig. 5.15) was drawn from the above discussion. This diagram can be very useful in identifying a flow situation in a given reservoir. From this work, the following conclusions can be drawn:

1. Transverse gravity (N_{gv}) and capillary (N_{cv}) numbers have been defined from this analysis for identifying flow regions in heterogeneous porous media. These numbers are the characteristic

time ratios for fluid to flow in the transverse direction due to gravity or capillary forces to that in horizontal direction.

2. Mobility ratio should be considered in the scaling process. With decreasing mobility ratio for a given medium, the viscous crossflow increases.

3. Miscible displacements can be very different in behavior depending on the system properties. Even for a system with an aspect ratio less than 0.1, the flow region can vary from viscous-dominated, to gravity-dominated regions depending on the gravity number.

4. Viscous-dominated flow in layered porous media can be in the vertical crossflow equilibrium region or the no-communication region depending upon the shape factor of the media and the gravity or capillary number of the system.

5. In near-miscible displacements, increases in injection pressure or enrichment will cause the gravity effects to increase.

6. In fractured systems, the capillary to gravity force ratio defines the recovery mechanisms of oil from the matrix. Hence, identifying the flow regions is important in the simulation of fractured reservoirs.

Table 5.2: Summary of data used to identify flow regions

Date source	Flow type (medium)	Scaling numbers N_B	$\frac{MN_{cv}}{1+M}$	$\frac{MN_{gv}}{1+M}$	${R_l}^2$	Flow regions
Du Prey [20]	imbibition (sandstone)	$0.05 - 10$			0.59	transition $0.2 < N_B < 5.0$
Hamon [28]	Imbibition (sandstone)	$10^{-3} - 10^{-1}$			$10^{-2} - 0.5$	capillary-dominated $N_B < 0.05$
Cuiec [16]	Imbibition (chalks)	$10^{-3} - 10^{-2}$			0.56	capillary-dominated $N_B < 10^{-2}$
Schechter [61]	imbibition drainage (sandstone)	$10^{-2} - 20$			0.01	transition $0.2 < N_B < 5.0$
Fayers [25]	miscible (simulation)		0	$10^{-4} - 10^{2}$	$10^{2} - 10^{3}$	transition $0.2 < \frac{MN_{gv}}{1+M} < 2.0$
Araktingi [3]	miscible (simulation)		0	$10^{-4} - 1.0$	$10^{2} - 10^{3}$	viscous-dominated $0.25 < \frac{MN_{gv}}{1+M}$
Ingsoy [33]	miscible (bead-packs)		0	$8.0 - 14.0$	20	gravity-dominated $\frac{MN_{gv}}{1+M} > 5.0$
Pozzi [55]	miscible (bead-packs)		0	$10^{-5} - 10^{-1}$	$10 - 10^{5}$	gravity-dominated $\frac{MN_{gv}}{1+M} > 5.0$
Zapata [75]	viscous flow (simulation)		0	0	0.1–?	VCE ${R_l}^2 > 10^2$
Thiele [66]	viscous flow (simulation)		0	0	$10^{-2} - 10^{3}$	transition $0.1 < \frac{1}{{R_l}^2} < 10^2$
Yokoyama [71]	imbibition (simulation)		$0 - 57.4$	0	$0 - 10^{4}$	capillary-dominated $\frac{N_{cv}M}{1+M} > 4.1$
Dawe [18]	imbibition (bead-packs)		$13.1 - 250$	0	25	capillary-dominated $\frac{N_{cv}M}{1+M} > 13.1$
Ahmed [1]	imbibition (bead-packs)		$0.29 - 14.3$	0	14.3	transition $0.2 < \frac{N_{cv}M}{1+M} < 6.1$
Pavone [53]	drainage (carbonate)		$0.2 - 20$	0	11.1	transition $0.2 < \frac{N_{cv}M}{1+M} < 10$

6. Summary

The simulation results of Chapter 2 reveal several important features of gas injection processes. They show, for example, that multicomponent flow can be adequately represented with a small number of components and that the presence of two-phase flow, which will occur in all real gas injection processes, can reduce significantly the mobility ratios that govern flow instabilities. Thus, the two-phase flow that results from dispersive mixing and crossflow actually reduces the tendency for viscous fingering. Comparison of compositional and first-contact miscible (Todd-Longstaff) simulations shows that effects of gravity segregation are significantly underestimated in Todd-Longstaff models.

Differences between flows in 2D and 3D porous media are explored in particle-tracking simulations also described in Chapter 2. The computations show surprisingly large differences between 2D and 3D flow when both gravity and viscous forces are important. Simulation results in both parts of Chapter 2 show that heterogeneities reduce the impact of gravity on vertical flow. Those results suggest that adequate reservoir description is an essential part of any assessment of the relative importance of viscous and gravity forces.

A new technique for simulation of flow in heterogeneous reservoirs was demonstrated in Chapter 3. The method combines analytical solutions for one-dimensional flow with computations for flow in streamtubes. Example results show that reasonable approximations can be obtained at much lower cost with the new method than can be obtained by conventional simulation. Work continues to develop the technique to represent compositional effects in multicomponent displacements.

Another aspect of multicomponent flow is considered in Chapter 4, which reports results of a test of the analytical theory of two-phase, three-component flow. The experimental results show reasonable agreement with the theory, though there are some differences that remain to be explained. The agreement is good enough that experiments for four-component systems are being planned. Those experiments will test the key ideas that call for the existence of crossover tie lines [34] that can control development of miscibility.

The interplay of capillary and gravity forces in corefloods is examined in some detail in the first part of Chapter 5, which describes attempts to simulate the performance of low IFT imbibition experiments performed previously at Stanford. Conventional simulations do not agree well with experimental observations for those displacements. The reasons appear to be related to the way the effects of capillary-driving forces are represented in conventional simulators. The use of an equilibrium capillary pressure curve apparently does not adequately represent the complexity of the differing time scales of flows driven by gravity, by capillary forces in pore bodies, and by capillary forces in grooves and surface roughness. Development of better simulation models will require improved understanding of rates of motion associated with those mechanisms. The use of pore network simulations to study those mechanisms is being considered.

The final portion of Chapter 5 examines scaling behavior of the combined effects of gravity, viscous, and capillary forces. An analysis of the dimensionless forms of the appropriate differential equations reveals a set of dimensionless groups that delineates regimes where some subset of the forces dominates the flow. Experimental and simulation results were then reviewed to set approximate limits on the regions where transitions occur. The specified flow regimes and transitions are the first available that consider all three principal forces.

The results discussed in this report are but part of a broad-ranging examination of the scaling of the physical that control displacement performance in gas injection processes. The work in progress includes experiments to delineate physical mechanisms and test models, and

simulations to explore combinations of physical mechanisms that are difficult or impossible to study experimentally. Predictions of process performance at field scale will inevitably make use of simulation. It is the goal of this project to make those simulation predictions based on analysis of the physics of the flow rather than on empirical models that may not represent scaling behavior accurately. Therefore, a significant part of the research effort is aimed at fundamental description of the capillary, gravity and viscous-driving forces that move multicomponent fluids and phases in heterogeneous reservoirs. It will be improvements in understanding of the scales on which those mechanisms operate that give us the tools we need to design more effective recovery processes for very heterogeneous reservoirs.

References

[1] Ahmed, G., Castanier, L.M. and Brigham, W.E.: "An Experimental Study of Waterflooding from a Two-Dimensional Layered Sand Model," *SPE Reservoir Engineering* (February 1988) 219–227.

[2] Araktingi, U.G. and Orr, F.M., Jr.: "Viscous Fingering in Heterogeneous Porous Media," paper SPE 18095 presented at the 1988 SPE Annual Technical Conference and Exhibition, Houston, TX, October 2–5.

[3] Araktingi, U.G. and Orr, F.M., Jr.: "Viscous Fingering, Gravity Segregation and Reservoir Heterogeneity in Miscible Displacements in Vertical Cross Section," paper SPE 20176 presented at the 1990 SPE/DOE Seventh Symposium on Enhanced Oil Recovery, Tulsa, OK.

[4] Araktingi, U.G. and Orr, F.M., Jr.: "Viscous Fingering in Heterogeneous Porous Media," *SPE Advanced Technology Series* (1993) **1**, No. 1, 71–80.

[5] Barker, J.W. and Fayers, F.J.: "Transport Coefficients for Compositional Simulation with Coarse Grids in Heterogeneous Media," paper SPE 22591 presented at the 1991 SPE Annual Technical Conference and Exhibition, Dallas, TX, October 6–9.

[6] Bear, J.: *Dynamics of Fluids in Porous Media*, American Elsevier, New York (1972).

[7] Blunt, M. and Rubin, B.: "Implicit Flux Limiting Schemes for Petroleum Reservoir Simulation," (September 1990) Second European Conference on the Mathematics of Oil Recovery, France.

[8] Bourbiaux, B.J. and Kalaydjian, F.J.: "Experimental Study of Cocurrent and Countercurrent Flows in Natural Porous Media," paper SPE 18283 presented at the 1988 SPE Annual Technical Conference and Exhibition, Houston, TX, October 2–5.

[9] Brock, D.C.: *An Experimental Investigation of Viscous Fingering in Heterogeneous Porous Media*, PhD dissertation, Stanford University, Stanford, CA (1990).

[10] Brock, D.C. and Orr, F.M., Jr.: "Flow Visualizations of Viscous Fingering in Heterogeneous Porous Media," paper SPE 22614 presented at the 1991 SPE Technical Conference and Exhibition, Dallas, TX, October 6–9.

[11] Buckley, S.E. and Leverett, M.C.: "Mechanism of Fluid Displacement in Sands," *Trans., AIME* (1941) **249**, 107–116.

[12] Chang, Yih-Bor, Lim, M.T., Pope, G.A. and Sepehrnoori, K.: "Carbon Dioxide Flow Patterns Under Multiphase Flow, Heterogeneous Field Scale Conditions," paper SPE 22654 presented at the 1991 SPE Annual Technical Conference and Exhibition, Dallas, TX, October 6–9.

[13] Christie, M.A. and Bond, D.J.: "Multidimensional Flux Corrected Transport for Reservoir Simulation," paper SPE 13505 presented at the 1985 Symposium on Reservoir Simulation, Dallas, TX, February.

[14] Christie, M.A. and Bond, D.J.: "Detailed Simulation of Unstable Processes in Miscible Flooding," *Soc. Pet. Eng. Res. Eng.* (November 1987) **2**, No. 4, 514–522.

[15] Christie, M.A., Muggeridge, A.H. and Barley, J.J.: "3D Simulation of Viscous Fingering and WAG Schemes," *Soc. Pet. Eng. Res. Eng.* (February 1993) 19–26.

[16] Cuiec, L.E., Bourbiaux, B. and Kalaydjian, F.: "Imbibition in Low-Permeability Porous Media: Understanding and Improvement of Oil Recovery," paper SPE 20259 presented at the 1990 7th Annual Symposium on Enhanced Oil Recovery, Tulsa, OK, April.

[17] Dake, L.P.: *Fundamentals of Reservoir Engineering*, Elsevier Scientific Publishing Company (1978).

[18] Dawe, R.A., Wheat, M.R. and Bidner, M.S.: "Experimental Investigation of Capillary Pressure Effects on Immiscible Displacement in Lensed and Layered Porous Media," *Transport in Porous Media* (1992) **7**, 83–101.

[19] Dindoruk, B.: *Analytical Theory of Multiphase, Multicomponent Displacement in Porous Media*, PhD dissertation, Stanford University, Stanford, CA (1992).

[20] du Prey, L.E.: "Gravity and Capillary Effects on Imbibition in Porous Media," *Soc. Pet. Eng. J.* (June 1978) 195–206.

[21] Ekrann, S.: "An Analysis of Gravity-Segregated Piston-like Displacements in Stratified Reservoirs," *SPE Reservoir Engineering* (February 1992) 143–148.

[22] El-Khatib, N.: "The Effects of Crossflow on Water-flooding of Stratified Reservoirs," *Soc. Pet. Eng. J.* (April 1985) 291–302.

[23] Fayers, F.J. and Lee, S.T.: "Crossflow Mechanisms by Gas Drive in Heterogeneous Reservoirs," paper SPE 24934 presented at the 1992 SPE Technical Conference and Exhibition, Washington, D.C.

[24] Fayers, F.J. and Newley, T.M.J.: "Detailed Validation of an Empirical Model for Viscous Fingering with Gravity Effects," *SPE Reservoir Engineering* (1988) **3**, 542–550.

[25] Fayers, F.J., Blunt, M.J. and Christie, M.A.: "Accurate Calibration of Empirical Viscous Fingering Models," *Revue de L'Institut Francais du Pétrole* (September 1990).

[26] Fayers, F.J., Blunt, M.J. and Christie, M.A.: "Comparisons of Empirical Viscous Fingering Models and Their Calibration for Heterogeneous Systems," *SPE Reservoir Engineering* (May 1992) 195–203.

[27] Fayers, F.J., Muggeridge, A.H.: "Extensions to Dietz Theory and Behavior of Gravity Tongues in Slightly Tilted Reservoirs," *SPE Reservoir Engineering* (November 1990) 487–494.

[28] Hamon, G. and Vidal, J.: "Scaling the Capillary Pressure from Laboratory Experiments on Homogeneous and Heterogeneous Samples," paper SPE 15852 presented at the 1986 SPE European Petroleum Conference, London, England, October 20–22.

[29] Hewett, T. and Behrens, R.: "Scaling Laws in Reservoir Simulation and Their Use in a Hybrid Finite Difference/Streamtube Approach to Simulation the Effects of Permeability Heterogeneity," *Reservoir Characterization, II*, L. Lake and J. Carroll, H.B. (eds.), Academic Press, Inc., London (1991).

[30] Higgins, R.V. and Leighton, A.J.: "A Computer Method to Calclate Two-Phase Flow in Any Irregularly Bounded Prous Medium," *Journal of Petroleum Technology* (June 1962) 679–683.

[31] Higgins, R.V., Boley, D.W. and Leighton, A.J.: "Aids to Forecasting the Performance of Water Floods," *Journal of Petroleum Technology* (September 1964) 1076–1082.

[32] Iffly, R., Rousselet, D.C. and Vermeulen, J.L.: "Fundamental study of imbibition in fissured oil fields," paper SPE 4102 presented at the 1972 SPE Annual Meeting, San Antonio, TX, October 8–11.

[33] Ingsoy, P. and Skjaeveland, S.M.: "Experimental Validation of New Method for Optimizing Miscible Flooding of Stratified Reservoirs," paper SPE 20176 presented at the 1990 SPE/DOE Seventh Symposium on Enhanced Oil Recovery, Tulsa, OK, April 22–25.

[34] Johns, R.T.: *Analytical Theory of Multicomponent Gas Drives With Two-Phase Mass Transfer*, PhD dissertation, Stanford University, Stanford, CA (1992).

[35] Johns, R.T., B. Dindoruk, and Orr, F.M. Jr.: "Analytical Theory of Combined Condensing/Vaporizing Gas Drives," *SPE Advanced Technology Series* (1993) **1**, No. 2, 7–16.

[36] Johns, R.T., Fayers, F.J. and Orr, F.M., Jr.: "Effect of Gas Enrichment and Dispersion on Nearly Miscible Displacements in Condensing/Vaporizing Drives," paper SPE 24938 presented at the 1992 SPE Technical Conference and Exhibition, Washington, D.C.

[37] Kazemi, H. and Merril, L.S.: "Numerical Simulation of Water Imbibition in Fractured Cores," *Soc. Pet. Eng. J* (June 1979) **19**, 175–182.

[38] King, M.J., Blunt, M.J., Mansfield, M. and Christie, M.A.: "Rapid Evaluation of the Impact of Heterogeneity on Miscible Gas Injection," paper SPE 26079 presented at the 1993 Western Regional Meeting, Anchorage, AK, May 26–28.

[39] Lake, W.L.: *Enhanced Oil Recovery*, first edition, Prentice Hall, Engelwood Cliffs, NJ 07632 (1989).

[40] Lenormand, R. and Zarcone, C.: "Role of Roughness and Edges During Imbibition in Square Capillaries," paper SPE 13264 presented at the 1984 SPE Annual Technical Conference and Exhibition, Houston, TX, September.

[41] Leverett, M.C.: "Flow of Oil-Water Mixtures Through Unconsolidated Sands," *Trans., AIME* (1939) **132**, 149–169.

[42] Martin, J.C. and Wegner, R.E.: "Numerical Solution of Multiphase, Two-Dimensional Incompressible Flow Using Streamtube Relationships," *Soc. Pet. Eng. J.* (October 1979) 313–323.

[43] Mohanty, K.K. and Johnson, S.W.: "Interpretation of Laboratory Gasfloods with Multidimensional Compositional Modeling," paper SPE 21204 presented at the 1991 Symposium on Reservoir Simulation, Anaheim, CA, February 17–20.

[44] Mohanty, K.K., Davis, H.T. and Scriven, L.E.: "Physics of Oil Entrapment in Water-Wet Rock," *SPE Reservoir Engineering* (February 1987) 113–128.

[45] Monroe, W.W., Silva, M.K., Larsen, L.L. and Orr, F.M. Jr.: "Composition Paths in Four-Component Systems: Effect of Dissolved Methane on 1D CO_2 Flood Performance," *Soc. Pet. Eng. Res. Eng.* (August 1990) 423–432.

[46] Morrow, N.R. and Songkran, B.: "Effect of Viscous and Buoyancy Forces on Nonwetting Phase Trapping in Porous Media," *Surface Phenomena in Enhanced Oil Recovery*, D. Shah (ed.), Plenum Press, New York City, NY (1982) 387–411.

[47] Morrow, N.R., Chatzis, I. and Taber, J.J.: "Entrapment and Mobilization of Residual Oil in Bead Packs," *Soc. Pet. Eng. Res. Eng.* (1988) **3**, 927–935.

[48] Orr, F.M., Jr., Johns, R.T. and Dindoruk, B.: "Miscibility in Four-Component Vaporizing Gas Drives," paper SPE 22637 presented at the 1991 SPE Annual Technical Conference and Exhibition, Dallas, TX, October 6–9.

[49] Pande, K.K.: *Interaction of Phase Behaviour with Nonuniform Flow*, PhD dissertation, Stanford University, Stanford, CA (December 1988).

[50] Pande, K.K. and Orr, F.M., Jr.: "Interaction of Phase Behavior, Reservoir Heterogeneity and and Crossflow in CO_2 Floods," paper SPE 19668 presented at the 1989 SPE Annual Technical Conference and Exhibition, San Antonio, TX, October 8–11.

[51] Pande, K.K. and Orr, F.M., Jr.: "Analytical Computation of Breakthrough Recovery for CO_2 Floods in Layered Reservoirs," paper SPE 20177 presented at the 1990 SPE Annual Technical Conference and Exhibition, Tulsa, TX, April 22–25.

[52] Pande, K.K. and Orr, F.M., Jr.: "Effects of Permeability Heterogeneity on Miscibility Development in Condensing Gas-Drive Processes," paper SPE 22635 presented at the 1991 SPE Annual Technical Conference and Exhibition, Dallas, TX, October 6–9.

[53] Pavone, D., Bruzzi, P. and Verre, R.: "Gravity Drainage at Low IFT," (October 1989) 5th European Symposium on Enhanced Oil Recovery, Budapest.

[54] Pongpitak, S.: "Interaction of Phase Behavior with Multiphase Flow in Porous Media," Master's thesis, New Mexico Institute of Mining and Technology, Socorro, New Mexico (February 1980).

[55] Pozzi, A.L. and Blackwell, R.J.: "Design of Laboratory Models for Study of Miscible Displacement," *Soc. Pet. Eng. J.* (March 1963) **3**, 28–40.

[56] Richardson, Joseph G.: *Handbook of Fluid Dynamics*, first edition, McGraw-Hill Book Company, Inc., Englewood Cliffs, NJ (1959) Ch. 16, 16–72 to 16–74.

[57] Roof, J.G.: "Snap-Off of Oil Droplets in Water-Wet Pores," *Soc. Pet. Eng. J.* (March 1970) 85–90.

[58] Rubin, B., Barker, J.W., Blunt, M.J., Christie, M.A., Culverwell, I.D. and Mansfield, M.: "Compositional Reservoir Simulation with a Predictive Model for Viscous Fingering," paper SPE 25234 presented at the 1993 Symposium on Reservoir Simulation, New Orleans, LA, February.

[59] Sarma, H. and Bentsen, R.G.: "A New Method for Estimating Relative Permeabilities from Unstabilized Displacement Data," *J. Pet. Tech.* (July–August 1989) **28**, No. 4, 118–128.

[60] Schechter, D. and Zhou, D.: "Capillary Imbibition and Gravity Segregation: Interactions with Phase Equilibrium in Oil/Brine/Alcohol System," Annual Report No. U.S. DOE Grant No. DE-FG21-89MC26253, U.S. Department of Energy, Bartlesville, OK (1991) Chap. 3.4 in "Scale-Up of Miscible Flood Processes".

[61] Schechter, D.S., Zhou, D. and Orr, F.M., Jr.: "Capillary Imbibition and Gravity Segregation in Low IFT Systems," paper SPE 22594 presented at the 1991 SPE Annual Technical Conference and Exhibition, Dallas, TX, October 6–9.

[62] Shook, M., Li, D. and Lake, L.E.: "Scaling Immiscible Flow Through Permeable Media by Inspectional Analysis," *In Situ* (1992) **16**, No. 4, 311–349.

[63] Stalkup, F.I.: "Miscible Displacement," Monograph 8, Soc. Pet. Eng. of AIME, New York (1983).

[64] Tchelepi, H.A. and Orr, F.M., Jr.: "The Interaction of Viscous Fingering, Permeability Heterogeneity and Gravity Segregation in 3D," paper SPE 25235 presented at the 1993 Symposium on Reservoir Simulation, New Orleans, LA, February 28–March 3.

[65] Tchelepi, H.A., Orr, F.M., Jr., Rakotomalala, N., Salin, D., and Woumeni, R.: "Dispersion, Permeability Heterogeneity and Viscous Fingering: Acoustic Experimental Observations and Particle-Tracking Simulations," *Phys. Fluids A* (July 1993) **5**, No. 7, 1558–1574.

[66] Thiele, M.R.: "A Pseudofunction Approach to the Description of Viscous Crossflow in Multilayered Permeable Media," Master's thesis, University of Texas, Austin, TX (1988).

[67] Todd, M.R. and Longstaff, W.J.: "The Development, Testing and Application of a Numerical Simulator for Predicting Miscible Flood Performance," *Trans., AIME, 253* (1972) 874–882.

[68] Walsh, B.W. and Orr, F.M. Jr.: "Prediction of Miscible Flood Performance: The Effect of Dispersion on Composition Paths in Ternary Systems.," *IN SITU* (1990) **14**, No. 1, 19–47.

[69] Wattenbarger, Robert C.: *Simulation of Tracer Flow Through Heterogeneous Porous Media*, PhD dissertation, Stanford University, Stanford, CA (December 1992).

[70] Withjack, E.M. and Akervoll, L.: "Computed Tomography Studies of 3-D Miscible Displacement Behavior in a Laboratory Five-Spot Model," paper SPE 18096 presented at the 1988 SPE Annual Technical Conference and Exhibition, Houston, TX, October.

[71] Yokoyama, Y. and Lake, L.: "The Effects of Capillary Pressure on Displacements in Stratified Porous Media," paper SPE 10109 presented at the 1981 SPE Annual Technical Conference and Exhibition, San Antonio, TX.

[72] Yortsos, Y.C.: "A Theoretical Analysis of Vertical Flow Equilibrium," paper SPE 22612 presented at the 1991 SPE Annual Technical Conference and Exhibition, Dallas, TX, October 6–9.

[73] Young, L.C.: "Equation of State Compositional Modeling on Vector Processors," paper SPE 16023 presented at the 1987 Ninth Symposium Reservoir Simulation, San Antonio, TX, February 1–4.

[74] Zapata, V.J.: "The Effects of Viscous Crossflow on Sharp Front Displacements in Two-layered Porous Media," Master's thesis, University of Texas, Austin, TX (1979).

[75] Zapata, V.J. and Lake, L.W.: "A Theoretical Analysis of Viscous Crossflow," paper SPE 10111 presented at the 1981 SPE Annual Technical Conference and Exhibition, San Antonio, TX, October 5–7.

[76] Zimmerman, W.B. and Homsy, G.M.: "Nonlinear Viscous Fingering in Miscible Displacements with Anisotropic Dispersion," *Phys. Fluids A* (1991) **3**, No. 8, 1859–1872.

DATE
FILMED
7/18/94

END